In silico study on *in vitro* experiments to determine the electric membrane properties of a realistic cochlear model for electric field simulations on cochlear implants

A thesis submitted for the degree of

Doctor of Engineering

of the Faculty of Computer Science and Electrical Engineering
of the University of Rostock

by Mirjana Holst
born on 06.01.1983 in Skopje, Macedonia

Rostock 2018

Tag der Einreichung: 26.06.2018
Tag der Verteidigung: 30.11.2018

Acknoledgments

I am truly grateful to my supervisors who were constant there for me to support and encourage me to pursue with my ideas no matter how difficult and challenging they were. This work would not be possible without Prof. U. van Rienens invaluable guidance and advice. Thank you for giving me this opportunity, your constant and professional guidance and supervision, the encouragement to face all obstacles and challenges and for the many ideas and invaluable discussions, without which I would not be able to accomplish this work.

I would like to thank Prof. H.-W. Pau for his valuable support throughout the years, immense knowledge in so many different areas and providing a lot of novel ideas. Thank you for your critical reading and useful suggestions to my dissertation.

I would like to thank Prof. R. Köhling for introducing me to the fascinating world of electrophysiology - glass microelectrodes, electrolytes and membranes. Thank you for enabling me to visit your Institute at any time and giving me the freedom and support to carry out the experiments on my own. I greatly benefited by your valuable advice and constructive suggestions. I am indebted to Dr. M. Rohde with whom I have worked at the Institute of Physiology. Thank you for your time and patience. My knowledge in electrophysiology has flourished under your guidance. Thanks to A. Prestel and all the staff members working or have been working at the Institute of Physiology, with whom I had contact or communication. Furthermore, it is a pleasure to thank H. R. Polder for his help with the electronic devices involved in this thesis, recommendations and useful hints considering the experiments.

I am grateful to Dr. A. Körtge, J. Schmidt and C. Mohic who helped me with the pipette geometry measurements. I would also like to thank Prof. Behrend and O. Specht for the support at the early stages of my work. Many thanks to Prof. Gimsa for his suggestions and cooperation. Richard Kosub thank you for supporting part of the experiments.

I would like to thank Kathrin Krebs for her support in all project issues. I wish to express my gratitude to Petra for being part of my workaday life, for the constant support, presence and advice throughout the years. Dr. B. Himmel thank you for the help with technical and software issues. I would also like to show my gratitude to my old and current colleagues at the Chair of Theoretical Electrical Engineering for the pleasant work and atmosphere.

I would like to thank my dearest friend Kathy and her lovely family for close interaction, support and encouragement over the years, especially for the valuable discussions and useful critiques during the important phase of writing this dissertation.

To my valuable family in Macedonia. I would like to thank you for giving me support in all aspects of life, helping me and being around me whenever I need you. Thank you for your generosity, patience and endless trust in me.

My deepest and immeasurable gratitude is reserved for my husband and three adorable children who fill my life with joy and happiness. Thank you for your understanding and compassion on daily basis.

Content

List of Figures

List of Tables

List of Symbols

A	cross-section, area [m²]
Ag/AgCl	silver/silver chloride
B	magnetic flux density [T=Vs/m²]
B	susceptance [S]
C	capacitance [F]
c	electrolytic concentration [mol/l]
CH_3COOK	potassium accetat
Cl^-	negative charged chloride ion
D	electric displacement [C/m²]
d	distance between bath electrode and tip opening [m]
d_l	thickness of the uniform glass layer [m]
d_s	dimension of the studied system [m]
d_t	tip diameter [m]
E	electric field [V/m]
ε	permittivity, $\varepsilon_r\varepsilon_0$
ε_0	permittivity of free space [As/Vm]
ε_r	relative permittivity
F{}	Fourier transform
f	frequency [Hz]
f_c	cutoff frequency, critical frequency
f_{end}	final instant frequency
f_{start}	initial instant frequency
G	conductance [S]
h	height of a truncated cone [m]
H	magnetic field [A/m]
$i(t)$	alternating current signal
I_0, i_m	current amplitude [A]
I_{pp}	peak to peak current amplitude
Im (**Z**)	imaginary part of the impedance
j	imaginary unit
J	current density [A/m²]
J_c	conduction current density [A/m²]
J_e	impressed current density [A/m²]
k	wave number
K^+	positive charged potassium ion
KCl	potassium chloride
l	immersion depth [m]
M	modulus function, $1/\varepsilon$
M	mol, number of particles, relative mass
n	number of layers
Na^+	positive charged sodium ion
NaCl	sodium chloride
p	millimetre distance starting from the tip opening

R	resistance [Ω]
R_e	electrode resistance [Ω]
Re ($\mathbf{Z}$)	real part of the impedance
R_i	internal electrode resistance
R_o	external electrode resistance
R_0	resistance at very low frequencies
R_∞	resistance at very high frequencies
r_1	inner glass tube diameter [m]
r_2	outer glass tube diameter [m]
r_a	apex radius [m]
r_b	base radius [m]
r_0	tip opening radius
t	time [s]
T	duration of the chirp pulse [s]
U	voltage [V]
V	electric potential [V]
$v(t)$	alternating voltage response [V]
v_m	voltage amplitude [V]
X	reactance [Ω]
Y	admittance [S]
$\mathbf{Z}$	impedance [Ω]
$|\mathbf{Z}|$	absolute value, magnitude of the impedance [Ω]
α	tip (conical) angle [rad]
θ	phase angle [degree]
λ	molar conductivity [Sm^2/mol]
μ	permeability, $\mu_r \, \mu_0$
μ_0	permeability of free space [Vs /Am]
μ_r	relative permeability
ρ	charge density [C/m³]
ρ_i	resistivity of the filling fluid [Ωm]
ρ_0	resistivity of the surrounding fluid [Ωm]
σ	conductivity [S/m]
τ	relaxation time, time constant [s]
τ_e	charge relaxation time [s]
τ_{em}	electromagnetic transit time [s]
τ_m	current density diffusion time [s]
ω	angular frequency, $2\pi f$ [1/s]
ω_{max}	characteristic (cutoff) angular frequency [1/s]
Ø	diameter
∇	grad (gradient operator)
$\nabla \cdot$	div (divergence operator)
$\nabla \times$	curl (curl operator)
$\approx$	approximately equal to
$\sim$	proportional to

List of Acronyms

AC	Alternating Current
ACSF	Artificial Cerebrospinal Fluid
BEM	Boundary Element Methods
BiCGStab	Biconjugate Gradient Stabilized Method
BNC	Bayonet Nut Connector
CB	Chair of Biophysics
CI	Cochlear Implants
CNLS	Complex Nonlinear Least Square
CPE	Constant Phase Element
CTEE	Chair of Theoretical Electrical Engineering
dB	decibel
DC	Direct Current
DEO	Department of Experimental Ophtalmology
DFG	Deutsche Forschungsgemeinschaft
DOHN	Department of Otorhinolaryngology, Head and Neck Surgery
EQS	Electro-Quasistatic
FD	Finite Difference Method
FEM	Finite Element Method
FFT	Fourier transform
FIT	Finite Integration Technique
IBMT	Institute of Biomedical Technik
IEAC	Institute of Electronic Appliances and Circuits
IHCs	inner hair cells
IP	Institute of Physiology
IS	Impedance Spectroscopy
MQS	Magneto-Quasistatic
NLLS	Nonlinear Least Square Method
OHCs	Outer Hair Cells
PMMA	polymethylmethacrylat (plexiglass)
RC circuit	resistor-capacitor ciruit
SEC	Single Electrode Clamp
TMC	Technical Manifacturing Corporation
ZAP	Impedance Amplitude Profile

Abstract

To further develop and optimise the design and effectiveness of cochlear implants, an advanced numerical model with precise material properties and authentic geometry is required. Since simulation results strongly depend on the accuracy of the adopted estimates of the electrical properties of cochlear membranes, it is of vital importance to have a reliable and accurate *in vivo* method for measuring electrical impedance changes in the cochlear compartments. To prove the functionality, characterize the accuracy and study the limits of such an *in vivo* method, simulations and measurements on an *in vitro* model devised for this purpose, have been performed. Such a work permits a great level of simplification of the system under study and can predict its *in vivo* performance. Indeed, this work is a preliminary attempt to consider, model, simulate and analyse the behaviour of a novel *in vitro* experimental system for conducting plausible *in vivo* measurements on mammalian cochlea membranes.

The project goal is centred around an *in silico* study of an *in vitro* measurement setup for determination of the electric impedance of the cochlear membranes.

Here, the principle and a detailed description of an *in vitro* modeling of cochlea are introduced. Essential information about the chosen measurement method and configuration is provided, too. Extensive description of the basic instrumentation, electrode types and their fabrication and characterization, the composition of electrolyte solutions as well as tissue samples used in the experiments is presented. Furthermore, the inevitable alternations, modifications and upgrades of the experimental setup are presented and discussed. A newly designed Ussing-chamber is introduced, as well.

The *in vitro* experimental setup is modeled and simulated in COMSOL Multiphysics® as well as in MATLAB®/Simulink®. The models mimicry the *in vitro* environment and allow exceptionally good evaluation and comparison of simulated and measured impedance values. The lumped parameter models in MATLAB®/Simulink® are also very useful in the process of calibration, verification and validation of the devices.

To determine and analyse impedance profiles at different frequencies i.e. impedance profile of biological membranes, the impedance spectroscopy is used. A numerical procedure has been developed in order to automatically convert time domain data into frequency domain. Subsequently, the obtained impedance data is fitted to an appropriate model and important parameter (resistance and capacitance) values are estimated and extracted.

Moreover, the computer application is validated and a comparison with experimental measurement data is carried out giving the opportunity to explain the discrepancies between the results.

Zusammenfasssung

Zur Weiterentwicklung und Optimierung des Designs und der Wirksamkeit von Cochlea-Implantaten ist ein detailliertes numerisches Modell der Cochlea mit exakt ermittelten Materialeigenschaften und realitätsnaher Geometrie erforderlich. Da die Ergebnisse der Simulation stark von der Genauigkeit der angenommenen Schätzungen der elektrischen Eigenschaften der Cochlea-Membranen abhängen, ist es von entscheidender Bedeutung, ein zuverlässiges und präzises In-vivo-Verfahren zur Messung des elektrischen Impedanzverlaufs der Cochlea-Sektoren zu haben. Um die Funktionalität zu prüfen, die Genauigkeit zu charakterisieren und die Grenzen einer solchen In-vivo-Methode zu untersuchen, wurden Simulationen und Messungen an einem für diesen Zweck entwickelten In-vitro-Modell durchgeführt. Der Hauptvorteil dieser Methode besteht darin, dass sie einen hohen Vereinfachungsgrad des untersuchten Systems erlaubt und die In-vivo-Charakteristik realitätsnah vorhersagen kann. Unter diesem Aspekt ist diese Arbeit eine vorbereitende Studie, das Verhalten eines neuartigen In-vitro- Versuchssystems zur Durchführung plausibler In-vivo-Messungen an Cochlea-Membranen von Säugetieren, zu modellieren, zu simulieren und zu analysieren.

Das Projektziel konzentriert sich hauptsächlich auf eine In-silico-Studie eines In-vitro-Messaufbaus zur Bestimmung der elektrischen Impedanz von Cochlea-Membranen.

Hier wird das Prinzip der In-vitro-Modellierung der Cochlea einschließlich einer detaillierten Beschreibung ihrer Teile vorgestellt. Weiterhin werden wesentliche Informationen über die gewählte Messmethode und die gewählte Konfiguration bereitgestellt. Im Anschluss werden die grundlegenden Instrumente und Messkonfigurationen, die bei der Durchführung der Experimente verwendet werden, vorgestellt. Dies betrifft die Elektrodenarten einschließlich ihrer Herstellung und Charakterisierungen, die Zusammensetzung von Elektrolytlösungen sowie die Gewebeproben. Außerdem werden erforderliche Veränderungen, Modifikationen und Verbesserungen des Versuchsaufbaus erläutert und diskutiert. Eine neu gestaltete Ussing-Kammer wird ergänzend vorgestellt.

Der In-vitro-Versuchsaufbau wird sowohl in COMSOL Multiphysics® als auch in MATLAB®/Simulink® modelliert und simuliert. Die Modelle bilden die In-vitro-Umgebung nach und erlauben eine sehr gute Bewertung und einen Vergleich von simulierten und gemessenen Impedanzwerten. Die Lumped-Parameter-Modelle in MATLAB®/Simulink® sind ebenfalls sehr nützlich bei der Kalibrierung, Verifizierung und Validierung der Geräte.

Um den Impedanz-Frequenzgang biologischer Membranen zu ermitteln und zu analysieren, wird die Impedanzspektroskopie verwendet. Dafür wurde ein numerisches Verfahren entwickelt, um Daten aus dem Zeitbereich automatisch in den Frequenzbereich zu konvertieren. Anschließend werden die erhaltenen Impedanzdaten an ein geeignetes Ersatzmodell angepasst und wichtige Ersatzgrößen (Widerstand und Kapazität) abgeschätzt und extrahiert. Darüber hinaus wird die rechnertechnische Analyse validiert und ein Vergleich mit experimentellen Messdaten durchgeführt, um die Unterschiede zwischen den Ergebnissen zu erklären.

1 Introduction

Hearing rehabilitation has advanced significantly since introduction of cochlear implants (CIs). At the beginning, a CI was developed as an electronic device to facilitate deaf people to get a sound impression of the surrounding environment. Over the years, however its specifications were broadened to include people with severe to profound hearing loss as well as children. This expansion was possible as a result of continuous development of these systems. The success of CI may be attributed to the dedicated work and combined efforts of scientists from various disciplines - bioengineering, physiology, otolaryngology, speech science and signal processing. Each of these disciplines contributed to various aspects of the CIs design [1]. A significant progress has been especially made in the combined acoustic and electrical stimulation (bi-modal stimulation). In this context, new electrodes were created, with the aim of decreasing the insertion trauma and preserving residual hearing. Among other concepts, the idea of a new flat electrode was developed, which could be endosteally inserted into the cochlea [2], [3]. This is a prerequisite for a successful bi-modal stimulation. To further develop and optimize the design and effectiveness of such and any other cochlear implant electrode carriers, a numerical model with precise material properties and authentic geometry is required. Since simulation results strongly depend on the accuracy of the estimated electrical properties of cochlear membranes, it is essential to have highly accurate material properties of all constituents, for which data is still lacking. Specifically, the impedances of cochlear compartments are either unfamiliar or very often based on appraised values deducted from lumped parameter circuit models [5]. For many cochlea structures, the impedance values have never even been measured. Thus, the establishment of a novel *in vivo* method is highly desirable.

1.1 Aim of work

To further develop, optimise and improve the design and effectiveness of cochlear implants, a physical cochlear model with realistic material properties and geometry is required. To date, a number of studies have been performed and several techniques have been employed to investigate the properties of the implanted cochlea. Yet implementation of different cochlear models based on various methods (Analytical Model [4], Lumped Parameter Model [5], Finite Element Model [6] and Boundary Element Model [7]) has shown that the simulation results are strongly influenced by the chosen approach and the adopted estimates of the electrical properties for the cochlear components.

The available literature data contains an enormous spectrum of values due to diverse methodology (*in vivo*, *ex vivo*, *in vitro*), measurement electrode configuration (different electrode types and geometry, inclusion of various number of electrodes) and conditions (body and environment temperature, used drugs, applied signal and frequency) used for their measurement and derivation. Thus, there is no straight–forward procedure to select which values to use in the simulations. Hence, a new *in vivo* method needs to be established. In order to obtain accurate values of the membrane properties *in vivo*, it is

convenient to first experiment on an *in vitro* model devised for this purpose. The primary advantage of such a work is that it permits a great level of simplification of the system under study and can predict its *in vivo* performance. This approach also provides precise evaluation and optimization of the parameters of the measurement configuration. This work is a preliminary attempt to consider, model, simulate and analyse the behaviour of a novel *in vitro* experimental system for conducting plausible *in vivo* measurements on mammalian cochlea membranes.

In summary, the project is basically focused on an *in silico* study of an *in vitro* measurement setup for determination of the electric impedance of the cochlear membranes. From the impedance values, the membrane electrical properties, electrical conductivity and electrical permittivity, can be deducted. Moreover, the computer application is validated and a comparison with experimental measurement data is carried out giving the opportunity to explain the discrepancies between the results.

As a result, the gained membrane electrical properties are intended for further studies on modeling and simulation of the human cochlea (3D-CAD-model) [8] and on electric stimulation of auditory nerve by cochlear implant electrodes [9] (Figure 1.1).
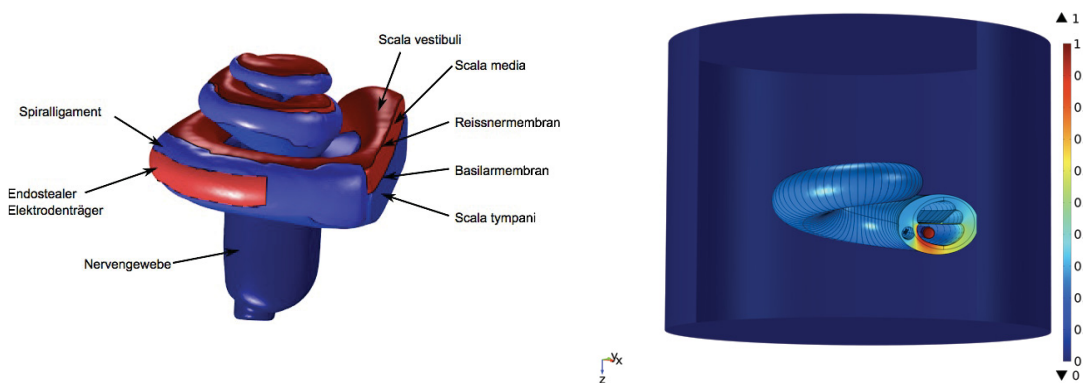
Figure 1.1: A 3D CAD model of the cochlea (left) [8]; field distribution in the cochlea for bipolar stimulation (right) [9].

The project, part of the DFG Research Training Group 1505 *welisa,* has embraced a very interdisciplinary approach. Overall, the main research work, the numerical simulations and data analysis were completed at the Chair of Theoretical Electrical Engineering (CTEE) (Faculty of Computer Science and Electrical Engineering) whereas the measurements took place at the Institute of Physiology (IP) (Rostock University Medical Center) where the experimental setup is situated. In order to achieve the project aims, an interdisciplinary network with diverse other institutes of University of Rostock was built and very successfully maintained, among which are the Department of Otorhinolaryngology, Head and Neck Surgery (DOHN) (Rostock University Medical Center), Institute of Biomedical Technik (IBMT) (Faculty of Mechanical Engineering and Marine Technology), Chair of Biophysics (CB) (Faculty of Mathematics and Natural Sciences), Institute of Electronic Appliances and Circuits (IEAC) (Faculty of Computer Science and Electrical Engineering) and Department of Experimental Ophtalmology (DEO) (Rostock University Medical Center).

1.2 Outline

The actual content of the thesis is organized in several chapters. Chapter 2 provides some important background information regarding the auditory system and the hearing process as well as the cochlear implants. Further, in the same chapter a brief introduction of the electrical bioimpedance basis is given. Chapter 3 is dedicated to the application of bioimpedance measurements in cochlear partition. In the second section of Chapter 3 a novel *in vitro* method is proposed, followed by a detailed description of the experimental set up and its components. In Chapter 4, the emphasis is on the fundamentals of the finite element method and the FEM model of the *in vitro* experimental setup. A lumped parameter model is furthermore introduced. Important numerical simulation results and measured data are presented, compared and validated in Chapter 5. Finally, suggestions and conclusions for possible future work are given in Chapter 6.

2 Background

2.1 Auditory system and hearing

The human auditory system consists of two basic parts, peripheral and central. The main role of the peripheral system is to transform an enormous range of mechanical signals into a complex series of electrical signals in the central system. The peripheral auditory system includes the outer, middle and inner ears (Figure 2.1). Each of them has an important dedicated function in the process of sound transduction. The outer ear composed of the visible part - pinna, the ear hole - external auditory meatus and the ear canal - external auditory canal, collects the sounds from the environment. The middle ear beginning with the eardrum (tympanic membrane) is an air-filled space cavity which houses the three smallest bones (malleus, incus, and stapes) in the body responsible for conducting sound to the inner ear. The inner ear contains the sensory cells for hearing (the cochlea) and balance (the vestibular system) and it is the ear structure where mechanical movement changes into electrical impulse. Finally the auditory nerve carries the sound information, in the form of nerve impulses from the inner ear to the brain.
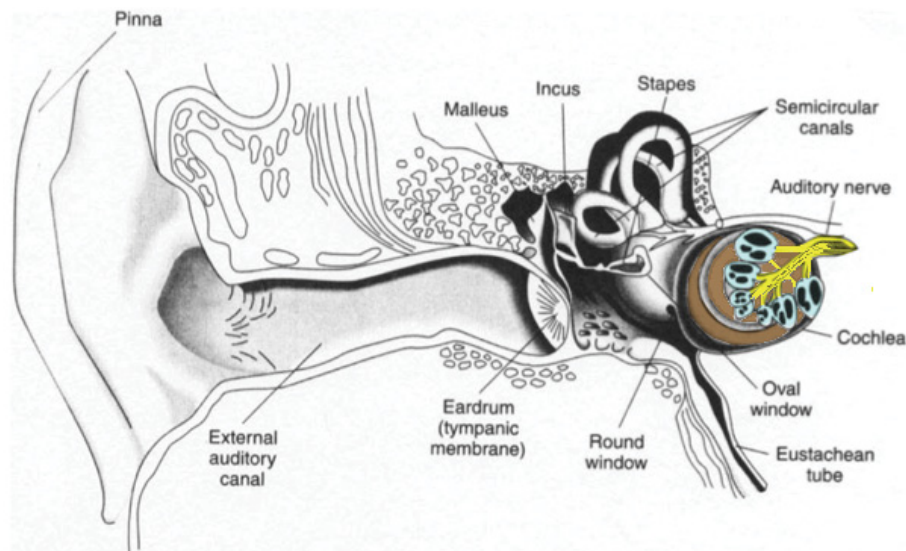
Figure 2.1: The human ear (adapted from [10]).

The process of hearing starts with the outer ear. The adequate stimulus is the sound. Ambient sounds in form of series of pressure changes in the air, funnel the ear canal via the pinna and a mechanical sound wave travels down the ear canal directly to the eardrum. The sound pressure on the eardrum sets it in vibrations. These vibrations are transmitted through the tiny middle ear bones to the fluid-filled cochlea, containing several thousands of sensory hair cells. Since fluid is not compressible, the back-forth motion of the fluid in the cochlea, sets the sensory cells into motion. As the hair cells move and change shape, they stimulate the auditory nerve. The electrical impulses generated by the hair cells are carried to the brain's hearing centres for further

processing. When the hair cells are damaged or missing, limited amount of sound information can be carried to the auditory nerve. As a result, sensorineural hearing loss appears. To get a better understanding of the conversion process of mechanical vibrations to electrical impulses, a more detailed description of the cochlea is given in the next section.

2.1.1 The Cochlea

The human cochlea is a complex spiral-tube structure that has the most important role in the process of hearing. Namely, here the mechanical vibrations are converted into electrical impulses.

Anatomically, the cochlea is shaped as a snail, approximately between two and a half and two and three-fourth turns [18], [20] wrapped around a conical bony structure called the modiolus. Uncoiled, the cochlea's hollow cavity is around 32 mm to 42 mm long [18], [19], [20] and 2 mm in diameter [21], whereas its actual diameter is only about 9 mm at the base [18]. The distance between base and apex is 5 mm [18]. The two human cochleae are mirror-shaped [20].
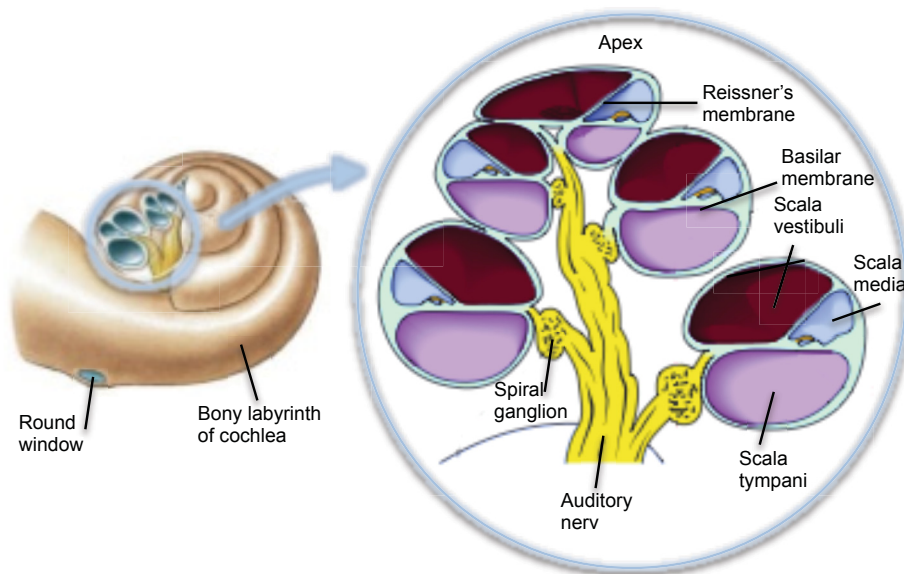
Figure 2.2: Anatomy of the cochlea: longitudinal cross section (adapted and modified from [11], [12]).

The part of the cochlea open toward the air cavity of the middle ear is known as the basal end (base). On the base, the cochlea has two soft spots, the oval and the round window. The other end of the cochlea or the inner tip is the apical end (apex).

The tube of the cochlea consists of three fluid-filled chambers or so-called scalae ('scala' stands for 'stairway' in Latin) - the scala vestibuli, the scala media (cochlea duct) and the scala tympani, separated by two membranes: the Reissner's membrane and the basilar membrane. The scala vestibuli is the uppermost chamber. The Reissner's membrane separates it from the scala media, which on the other side is separated from the scala tympani by the basilar membrane. Laying on the top of the basilar membrane

within the scala media, the organ of Corti is placed (Figure 2.3), over which the tectorial membrane is hanging. At the apical end, the scala vestibuli and scala tympani communicate with each other via an opening called the heliocotrema. At the other end of the spiral, the base of the cochlea, the scala vestibuli ends with the oval window connected to the stapes whereas the basal aperture of the scala tympani is the round window. Both chambers are filled with the same aqueous medium, known as perilymph ($\approx$ 150 mM Na^+ and 4 mM K^+), while the scala media is filled with endolymph ($\approx$ 1 mM Na^+ and 140 mM K^+). The difference of Na^+ and K^+ concentrations results in a constantly maintained endocochlear potential of +85 mV in the scala media [12], [14].

2.1.1.1 The organ of Corti

The organ of Corti is the part of the cochlea where the actual conversion of mechanical motion into a nerve impulse happens. It is attached on the basilar membrane in the scala media. Within the organ of Corti, along the whole length of the cochlea, a population of around 15 000 to 16 000 sensory hair cells are aligned in four rows [16]. Humans have one row of inner hair cells (IHCs) and, roughly in parallel, three rows of outer hair cells (OHCs), anatomically and functionally different. Each of these single cells has about 50 to 70 stereocilia, (tiny little hairs on the top of them) at the basal end and 100 in the apex of the cochlear partition [20]. Over them, a jelly-like mass, the tectorial membrane is laying, which touches only the stereocilia of the OHCs.
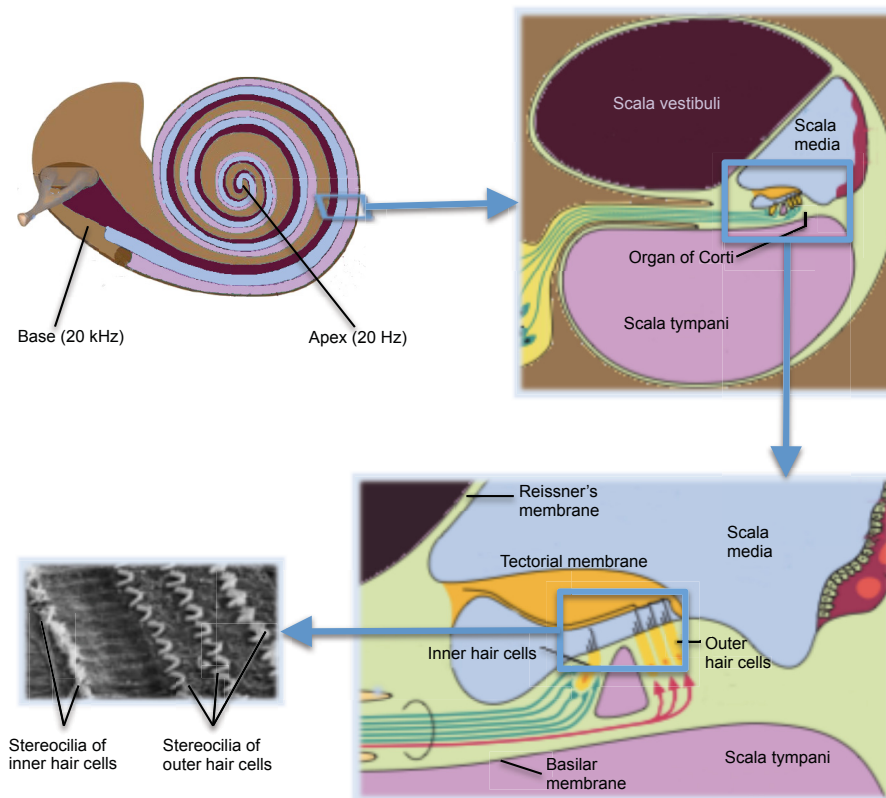
Figure 2.3: Cross section of the cochlea; organ of Corti (down right) and sensory hair cells (down left [14]). Adapted and modified from [11], [13].

The function of the OHCs is to enhance the mechanical pressure that enters the cochlea but not to send a signal to the brain. This role is taken over by the IHCs directly attached to the cochlear nerve fibres.

2.1.2 Coding of mechanical pressure into a neural signal

The crucial moment for transduction of mechanical pressure into a neural signal is the bending and changing of the form of the sensory hair cells as a result of a shear motion between the basilar and tectorial membranes.

This happens as an effect of the incoming mechanical pressure delivered to the cochlea fluid by the stapes footplate at the oval window. Since the perylimph in the scala vestibuli is incompressible, the fluid flows along the cochlea pushes the Reissner's membrane and brings the fluid in the scala media to move. As a consequence, the basilar and tectorial membranes are stretched in different directions. Furthermore, the stereocilia on the hair cells are bent back and forth. Eventually, a bioelectrical process is triggered and an exchange of ions takes place that alters the cell's membrane potential. The hair cells respond by sending an electrical signal to the auditory nerves, which ultimately transfers it to the brain, where it is interpreted as a tone.

The rapidity of signal transduction in the hair cells lies in the range between 20 Hz (hair cells at the apex) and 20 kHz (hair cells at the base) which turns to be the hearing range of the human being [16].

When the hair cells are partly lost or damaged, they cannot properly carry out their function in the mechanism of hearing and smaller amount of sound information is further conveyed to the auditory nerve. As a result, a permanent sensorineural hearing loss appears.

2.2 Hearing loss

In the previous sections, the human auditory system was described and the process of hearing was explained. However, in some cases due to certain factors it may happen that a partial or a total inability to hear appears. The hearing impairment can occur in one (unilateral) or both ears (bilateral), it can be congenital or acquired as well as temporary or permanent. Moreover, the degree of hearing loss can be classified as mild, moderate, moderate-severe, severe or profound. Depending on the causes and localisation, three different types of hearing loss can be distinguished:

- Sensorineural hearing loss appears as a result of damaging (degeneration) of the sensory hair cells in the inner ear. It is a permanent and usually acquired loss due to aging, continuously exposure to noise and chronic infections and diseases, although there also may be genetic factors.
- Conductive hearing loss occurs when the intensity and quality of sound information diminishes on the pathway from the outer ear to the inner ear. The problems appear in the external and middle ear as a result of genetic causes, malformation, metabolic disorders and infections. It is mostly temporary loss and in many cases hearing can be improved by eradication of infection, surgical interventions or with conventional hearing aids.

- Mixed hearing loss is a combination of sensorineural and conductive hearing loss.

As already mentioned there are several options for treating hearing loss. In order to determine the type and degree of hearing loss, a series of examinations and tests on the auditory system are necessary. Therefore, an appropriate non-invasive method is the audiogram. The audiogram (Figure 2.4) is a graph that gives information about the individual's type and degree of hearing lost. The x-axis presents the frequency (Hz) and the y-axis the measured intensity in dB. To determine where the problem of sound conduction within the ear appears, two different tests can be performed: air conducting and bone conducting. For each of the tests different markings on the audiogram are used.

An individual can normally hear at a frequency range of 20 Hz to 20 kHz with an amplitude of 0 dB to 130 dB. The threshold of normal hearing as well as the different degrees of hearing loss are shown in Figure 2.4.
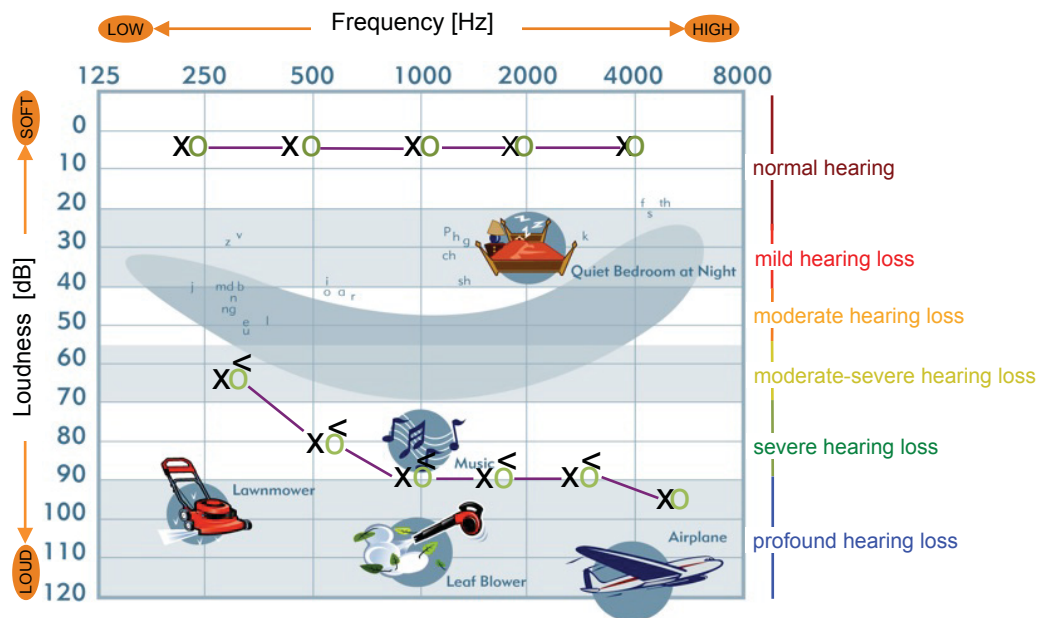
Figure 2.4: An audiogram (adapted and modified from [22]) showing normal hearing (up) and sensoneural hearing loss (down). O is the marking for the left ear, X is the marking for the right ear (air conduction test); the < over the O marks the response from the bone conduction.

The degree of hearing impairment determined from the bunch of tests including the results from the audiogram can point out whether the individual is a candidate for a conventional hearing aid (sound amplifier) or cochlear implant.

In this thesis, a brief introduction to the cochlear implants will be given. The conventional hearing aids will not be discussed in details.

2.3 Cochlear implants

Cochlear implants are electronic devices developed for treating the sensorineural hearing loss, which appears as a result of the reduction of function within the organ of Corti.
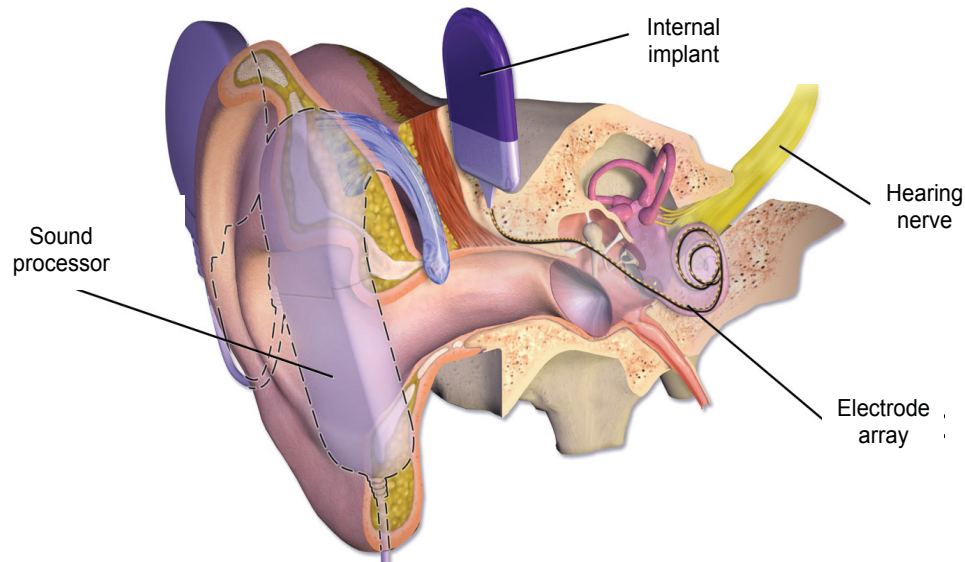
Figure 2.5: A cochlear implant and the position of its parts in the ear [23].

An implant cannot restore normal hearing, but it can facilitate severe-to-profound deaf people to get a sound impression of the surrounding environment.

The main role of the implants is to bypass the damaged parts (hair cells) of the cochlea and directly stimulate the hearing nerve, mimicking the mechano-electrical transduction of a healthy cochlea.

The implant (Figure 2.5, Figure 2.6) consists of two main parts that integrate the visible (external) and the implanted (internal) parts. On the headpiece attached on the skin slightly behind the pinna, a microphone together with a transmitter is placed. The microphone captures the sounds from the patient's surrounding environment and forwards them through a cable to the speech (sound) processor, a tiny electronic device that is usually placed directly on the pinna or worn near to the body. It arranges and converts the sounds picked by the microphone, into detailed digital impulses. This digital information is further transmitted through the magnetic headpiece via radio waves to the internal parts of the implant. Here the digital information is converted into electrical impulses that travel along the electrode carrier, which is implanted in the cochlea. The electrodes on the array, stimulate the auditory nerve, which sends impulses to the brain. Finally, the impulses are interpreted as tones.

Even though the cochlea implants can functionally restore hearing, still improvement of the electrode design is required to achieve hearing resembling the normal one.

Figure 2.6: External and internal parts of the cochlear implant (adapted and modified from [22]).

2.3.1 Conventional and endosteal electrodes

To date various types of cochlear electrode arrays have been developed and used for implantation in the cochlea. Their design differs not only in the geometry and material but also in the electronics, the number of sources and contacts as well as the position and insertion of depth [24]. Some electrode arrays are inserted close to the modiolar wall (perimodiolar electrodes) [25] whereas other lie free in the scala tympani usually near the lateral wall [20] (see Figure 2.7). Both approaches tend to optimise the interaction between the electrode array and the auditory nerve in order to achieve lower thresholds for electrostimulation.
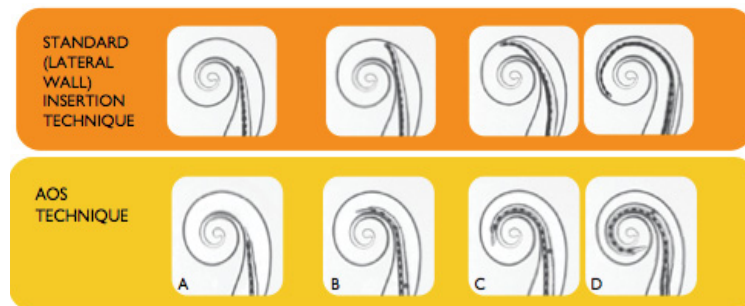
Figure 2.7: Insertion techniques of electrode arrays [26]; lateral (up) and perimodiolar (down).

Unfortunately, despite the enormous benefits offered by cochlear implants, all available design features of electrode arrays and established surgical techniques for insertion and positioning of the electrodes pose a risk for injury of the inner ear structures or cause trauma during the cochlear implant placement. In many cases this leads to permanent post-implantation loss of residual hearing. This is of course a problem for individuals who would like to benefit from the use of cochlear implants to improve hearing in high frequencies but have some residual hearing in low frequencies (bi-modal stimulation). Therefore, in order to overcome the obstacles mentioned above, a new innovative technology for soft cochlear implant insertion is required. Hence, Lehnhardt et al. [2], [3] has introduced an insertion method and cochlear electrode carrier (endosteal electrode) that does not interfere with the normal functioning of inner ear in the process

of implant placement. The idea behind the concept is to insert the electrode array into the cochlea endosteally between the spiral ligament and the endosteum of the cochlea bone [2], [3], [27]. In this way, the opening and breaching of the fluid-filled inner ear structures is averted, the hydrodynamic behaviour of the cochlea is preserved and there is no damaging of the still existing hair cells in the organ of Corti.
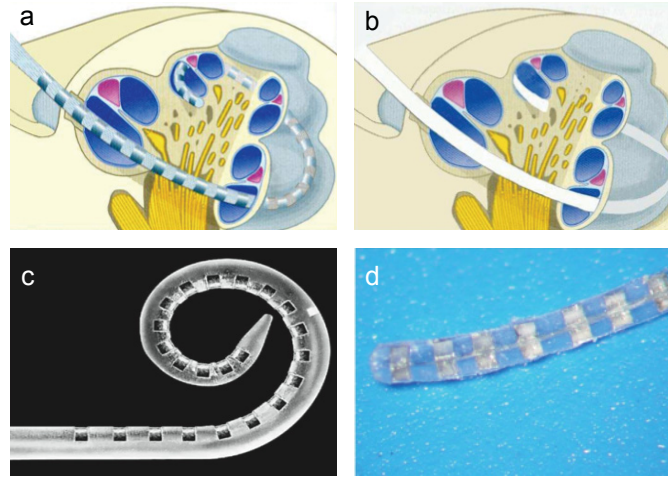
Figure 2.8: Location and design of convential (a, [28] and c, [19]) and endosteal (b, [28] and d, Courtesy of Prof. Pau).

In order to gain new insights and investigate the electrical behaviour of the endosteal electrode inside the cochlea, and before *in vivo* studies are made, numerical simulations on a electrostimulated physical cochlear model [8] should be performed. Therefore, for development of a three-dimensional, physics-based numerical cochlear model, beside the authentic geometry of the cochlear compartments, precise material properties of the cochlear membranes and fluids are highly desirable. To investigate and determine the bioimpedance profile of biological membranes, the impedance spectroscopy is used.

2.4 Electrical bioimpedance – the fundamentals

Electrical properties of biological materials have been a scope of major interest for over a century. In the biomedicine and electrophysiology, electrical bioimpedance measurements have entailed non-invasive techniques for characterizing electrical properties of biological cells and tissues. A detailed knowledge of tissue electrical properties is of great importance for a number of clinical applications which to date have been well established (e.g. lung plethysmography, electrocardiography, dermatology, tumor characterisation and body composition techniques). The biomaterial of interest can be a living or dead tissue from animal or human, as well as any other organic material related to a living organism such as a human, animal, cell, or plant [29].
Bioimpedance relates to the passive electrical properties of biological materials and consideres the capability of the material to oppose (impede) electrical current [30]. The general approach in the bioimpedance measurements is to apply an electrical stimulus,

either a known voltage or current, to a biomaterial and then measure the current flow or register the voltage drop. The excitation signal can be generated in several forms (Figure 2.9) and the choice of a suitable waveform depends on the observed object and the spectral range of interest. Step (rectangular) function or Gaussian pulses are most commonly used for broadband impedance measurements. Less applied, but much more effective (only a small amount of energy remains outside the desired bandwidth) are the sinc, multisine and the chirp signals [31], [32]. The latter ones, also called multi-frequency-one-time signals, are highly appropriate and gain advantage over the one-frequency-one-time signals because of the enormously reduced measurement time and acquired data. Not to forget the fast grasping of the transient physiological changes of a living organism. Additionally, a random (white) noise signal can be applied or some of the above mentioned signals can be combined to generate other types of stimuli [35].
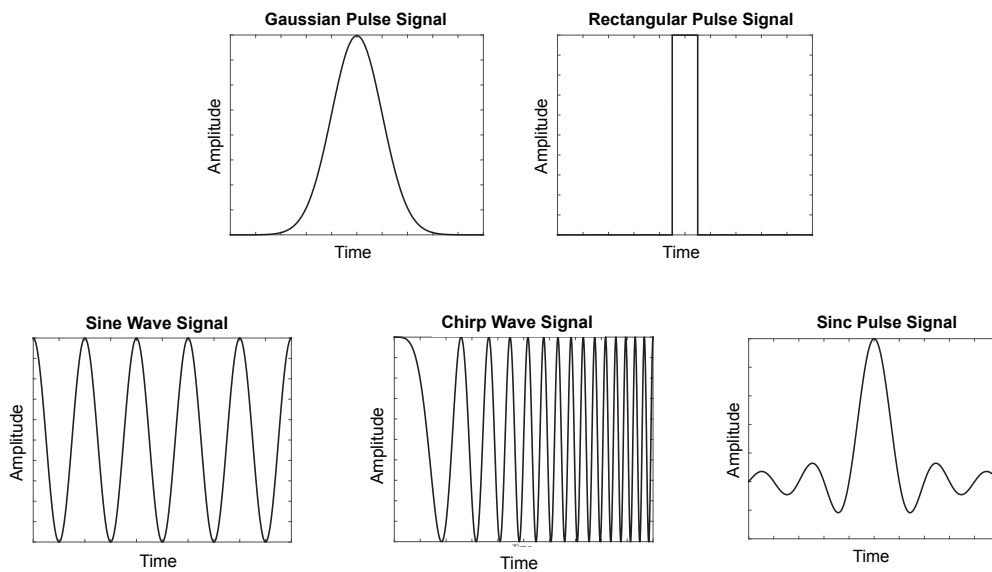
Figure 2.9: Different excitation signals: Gaussian pulse signal, rectangular pulse signal, sine wave signal, chirp wave signal and sinc pulse signal.

To conduct a bioimpedance measurement, an application of two or more electrodes is required to make an electrical contact with the observed biomaterial. The electrodes can be either current carrying, signal pick up or reference electrodes. It is of great importance to choose the proper electrode configuration to avoid the influence of electrode polarization and other side-effects which can reflect in the measurements. Hence, the quality of the bioimpedance data and the repeatability of the measurement strongly depends on the electrode system properties as well as their placement.

2.4.1 Impedance spectroscopy: analysis and interpretation of data

Since biological tissues possess not only resistive but also capacitive properties, with the increasing frequency, a phase shift of the voltage with respect to the current occurs and the amplitude of the impedance declines. Thus, the bioimpedance is frequency

dependent. To experimentally characterise the impedance of biomaterials, measurements in the wide frequency spectrum (starting from 10 µHz up to 10 MHz [36]) are pursued (impedance spectroscopy-IS). Impedance spectroscopy is a relatively new and powerful method capable to analyse some/all impedance-related functions (**Z** (impedance), **Y** (admittance = 1/**Z**) and **ε** (permittivity), **M** (modulus function = 1/**ε**)) at different frequencies, as well as plot them in the complex plane [35]. Subsequently, the obtained data is fitted to an appropriate model and important parameters, that describe the electrical properties of the biomaterials, are extracted.

2.4.1.1 Theory behind the impedance

When a small alternating current $i(t)$ with a known frequency $f = \omega/2\pi$ and amplitude i_m is applied on a biomaterial, the voltage response $v(t) = v_m sin(\omega t + \theta)$ is measured as a function of time. Here, θ is the phase difference between the current and voltage. From the recorded response and the input stimuli, the impedance values over a frequency spectrum are obtained. An impedance **Z** [Ω] is a complex number, defined as the ratio between the complex representation of the sinusoidal voltage and current signal. It is usually represented by a phasor, given the magnitude $|\mathbf{Z}| = v_m/i_m$ and phase θ or by a complex number in cartesian coordinates described with resistance R and reactance X. The representation of the impedance in the complex plane is shown in Figure 2.10 where $j = \sqrt{-1}$. There are two other terms related to impedance: the admittance **Y** [S] (inverse of impedance ($\mathbf{Y} = 1/\mathbf{Z} = G + jB$), admit current flow) and the immittance (term for unifying impedance and admittance).
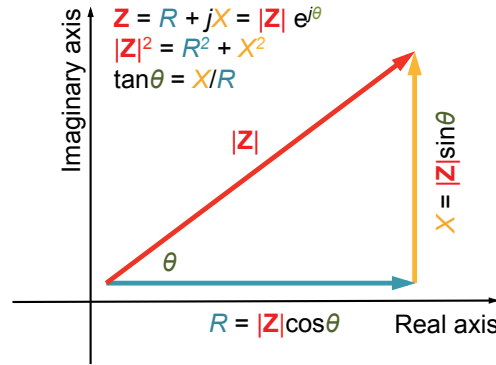
Figure 2.10: Representation of the impedance (complex plane).

Generally, the analysis of a bioimpedance measurement is carried out in frequency domain, hence, the Fourier transform is the link between time and frequency domain. In case of a sine wave excitation, the Fourier transform reduces the complex voltage/current relations (differential equations in time domain) to a form similar to the Ohm's law for DC current: $\mathbf{Z}(\omega) = \mathbf{F}\{v(t)\}/\mathbf{F}\{i(t)\}$, where $\mathbf{F}\{\}$ denotes the Fourier transform operator. Due to this, Ohm's law-like relationship between complex current and voltage, the equivalent impedance of a network with multiple elements is calculated implementing the same rules as with multiple resistors. Both serial and parallel combinations of elements can occur. In this way, the calculations are greatly simplified

[35]. Moreover, the impedance based relations between variables in a system can be used to derive an input/output transfer function of a system.

2.4.1.2 Analysis of impedance spectra: graphic presentation and electrical models

To perform a detailed data analysis, it is useful first to observe the data graphically, for rough interpretation of the AC signal response of the electrode-material system being investigated. The bioimpedance data can be presented in two and three-dimensional graphical form. The choice of presentation should be well conceived and ideally the measured data should be presented in more than one way before any crucial conclusions are deduced [34]. When a capacitive effect dominates over the inductive (common case in IS measurements) it is convenient to plot Im ($\mathbf{Z}$) on the y-axis and Re ($\mathbf{Z}$) on the x-axis. This complex plane impedance diagram is a locus plot also called as Nyquist (or Argand, Wessel, Cole) plot. The frequency scale is along the half circle locus, where each data point corresponds to a different frequency. An example of a response of a simple ideal parallel RC circuit (R and C components are frequency independent and linear) with admittance $\mathbf{Y} = 1/\mathbf{Z} = 1/R + j\omega C$ is shown in Figure 2.11. More expressions and explanations regarding this example are given in the next subsection.
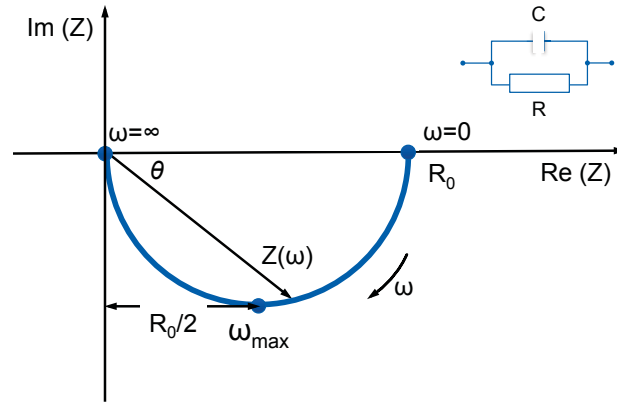
Figure 2.11: Impedance plane plot for a semi-circular arc of an ideal electrical circuit case of resistor in parallel with capacitor that involves a single time constant (relaxation time) $\tau = RC$.

Figure 2.11 shows definitions of quantities used in the analysis, where R_0 is the resistance at zero frequency, $\omega = 2\pi f$ the angular frequency (the arrow shows the direction of increasing frequency) and ω_{max} is the characteristic (cutoff) frequency corresponding to the apex of an arc ($\omega_{max} = 1/\tau$).

An entirely different approach is the Bode diagram (Figure 2.12), which plots the frequency response of a system. The Bode plots are a combination of a Bode magnitude log-log (log ($|\mathbf{Z}|$) against log (f)) and Bode phase semi-logarithmic (phase angle versus log (f)) plot. Moreover, the $|\mathbf{Z}|$, Re ($\mathbf{Z}$) and Im ($\mathbf{Z}$) can be plotted with respect to log (f). In the Bode representation, the frequency is logarithmic-scaled to emphasise the importance of the system behaviour in the lower frequencies. An example is depicted in Figure 2.12. Another important illustration for the analysis of complex dielectric systems ($\varepsilon(\omega) = \varepsilon'(\omega) - i\varepsilon''(\omega)$), is the Cole–Cole plot, where ε' (real part of $\varepsilon(\omega)$) vs

ε'' (imaginary part of $\boldsymbol{\varepsilon}(\omega)$) is plotted in the complex plane. For data illustration, three-dimensional perspective plots may be used which include log (f) axis [36].
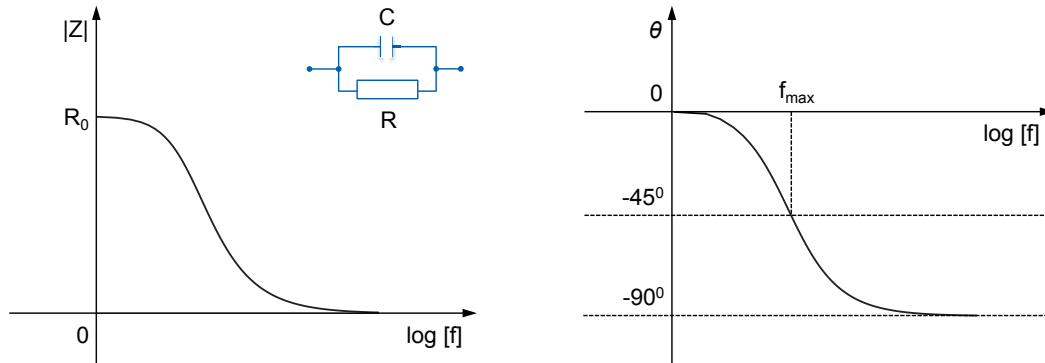
Figure 2.12: Bode plot of an ideal electrical circuit in case of a resistor in parallel with a capacitor that involves a single time constant $\tau = RC$. The left graphic displays the impedance magnitude over the frequency whereas the right graphic shows the phase over frequency.
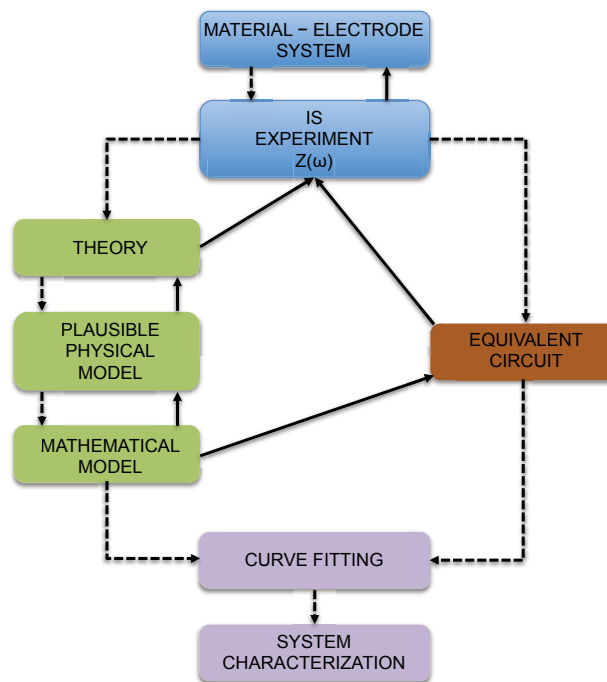
Figure 2.13: Characterization of the electrode-material interface (adapted from [35]).

Even though, from the graphical representation some system parameters can be read out, these values are usually only roughly estimated. Therefore, for precise characterization of the electrode-material interface, a fitting technique has to be implemented. In order to obtain parameter estimates of a model, the widely used

methods are based on the least square curve fitting technique (CNLS-complex nonlinear least square method, NLLS-nonlinear least square method). Hence, the experimental data is fitted to a mathematical model or to an equivalent parameter circuit (Figure 2.13).

In this study, the values of the model parameters are estimated by implementing the Nelder - Mead (simplex) method for finding the minimum of a scalar function of several variables.

For the data presentation, interpretation and analysis, from all above-mentioned and presented graphical plot forms, the complex impedance plot was mostly chosen. In some cases, additionally, different Bode representations were also used.

2.4.2 Properties of biological tissues

A biological tissue is composed of a collection of cells containing an intracellular fluid (cytoplasm) inside a cell membrane surrounded by an extracellular fluid. Electrically, the cytoplasm is a conductive medium due to the presence of large concentrations of ions. Moreover, the extracellular fluid is also conductive. On the other hand, the cell wall (plasma membrane) is a thin layer that is relatively insulating (stores energy) and has the major contribution to the dielectric behaviour of living tissue. Thus, the electrical properties of biological tissue are determined from the behaviour of its constituents in presence of an electric field. The dielectric theory is explained with the concept of the plane parallel-plate capacitor in subsection 2.4.2.1.

A full description of the electrical properties of cells and tissue should ideally include details associated with active ion transport and membrane potentials, but generally only the so-called passive electrical parameters are considered.

As previously explained, biological tissues show both conducting and insulating properties. The conductivity, σ, is namely determined by the ability of movement of free charges (ions) in the material whereas the permittivity, ε, by the ability of a material to be polarized (slight shift of the equilibrium position of the charges) by application of an electric field. For most biological tissues, however, these material properties are not constant, but vary with the frequency of the applied signal. Thus, σ and ε are frequency-dependent. The significant variation in dielectric properties over a frequency range is called a dielectric dispersion. Generally, the dispersion can be characterized by an angular relaxation frequency $\omega_{max} = 2\pi f_{max}$ or by a relaxation time $\tau_{max} = 1/f_{max}$. Due to the fact that polarization does not occur instantaneously, the relaxation times are in the range of picoseconds to few seconds. Although the dielectric properties of the tissues vary greatly from tissue to tissue, their typical behaviour exhibited by the permittivity can be separated into three main regions, known as α-, β-, and γ-dispersions as shown in (Figure 2.14), [30], [34], [37], [40], [41], [42]. Other dispersions such as the δ-dispersion may also be present. The α-dispersion usually occurs in the Hz to kHz range due to counterion (ion) polarization, the β-dispersion arises from interfacial polarization (between intra and extra cellular media) in the frequency region from 10 kHz to tens of MHz, and the γ-dispersion in the microwave frequency region from hundreds of MHz to some GHz mainly caused by polarization of water molecules. With increasing frequency the conductivity increases while the permittivity decreases continuously.

Biological tissues are not only heterogeneous but also highly anisotropic. This implies that the electrical properties are additionally direction dependent. They vary strongly

with the tissues structure and geometry. Furthermore, the properties of tissues depend on the temperature too.
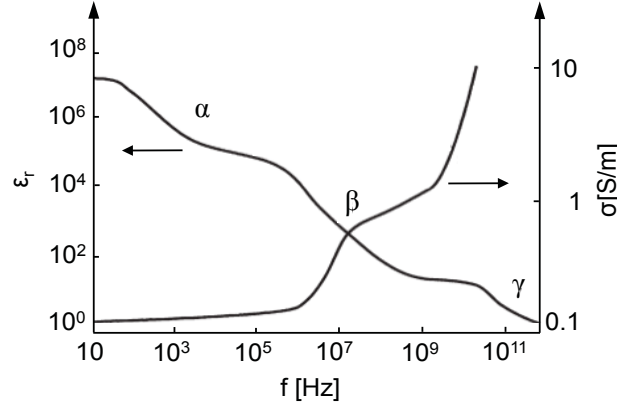
Figure 2.14: The relative permittivity ε_r (decreasing) and the conductivity σ (increasing) of biological tissue within the three main dispersion regions α, β and γ (modified from [37]).

More comprehensive details behind theory, modeling and experimental data about dielectric properties of biological tissues are treated and can be found in the literature ([44]-[50]).
Several more examples of responses of some simple RC circuits are described, presented, illustrated and analysed in the next subsection.

2.4.2.1 Examples of simple equivalent RC circuit for characterizing biological tissues

Numerous equivalent circuits have been proposed for physicochemical analysis and interpretation of an electrode-sample system. Some of them describe the behaviour of biological tissues as a combination of resistance R and reactance X in series, another in parallel, whereas others are much larger and more complex networks including even elements with frequency-independent phase angle (CPE-Constant Phase Element [29], [34]). However, the most simple one ('Debye-type' [36], [37], [39]) expresses an impedance of a biological tissue in terms of a conductance element $G = 1/R$ [S = 1/Ω] in parallel with a capacitance C [F],

$$\mathbf{Z} = \frac{1}{G + j\omega C} \tag{2.1}$$

where the parameters G and C imply that a biological tissue has conductive (resistive) and capacitive properties. These parameters describe the ability of the homogenous material to conduct and store electric charge.

$$R = \frac{1}{\sigma}\frac{d}{A}, \qquad \sigma = \frac{1}{\rho} \left[\frac{S}{m} = \frac{1}{\Omega m} \right]$$

$$C = \varepsilon \frac{A}{d}, \qquad \varepsilon = \varepsilon_0 \varepsilon_r$$
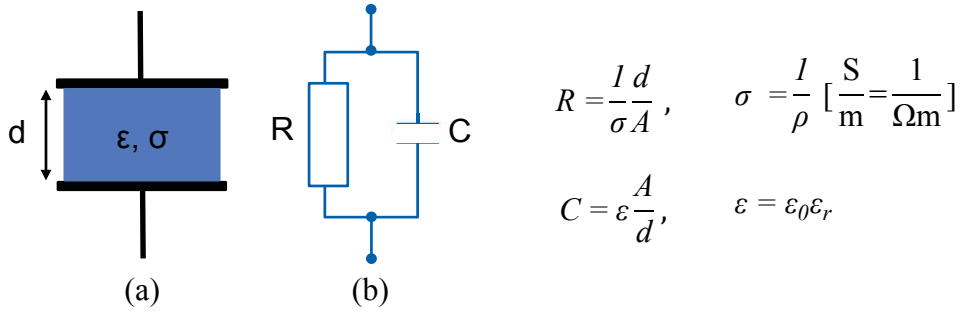
Figure 2.15: (a) An idealised slab of tissue; (b) an equivalent circuit of the slab of tissue represented by conductivity and capacity in parallel; see equation (2.1).

Typically, to define the electric passive properties of a homogeneous sample, a basic model (ideal parallel-plate capacitor model) of a slab [30], [40], [42], [43] that has thickness d and cross-section area A is considered, giving the relation between impedance and geometry (Figure 2.15, (a)). Knowing the geometry, the complex permittivity ε or conductivity σ can be derived.

More often, however, a multilayer model (heterogeneous structure) might be more appropriate to model biomaterials. Thus, the heterogeneous system can be presented by a number of layers with different material properties sandwiched together (Figure 2.16, (a)) [40], [42]. In this case the total impedance is given by

$$\mathbf{Z_N} = \sum_{n=1}^{N} \frac{1}{G_n + j\omega C_n} \tag{2.2}$$

where n denotes the number of distinguished layers. In such cases a presence of multiple time constants (relaxation processes) becomes apparent (Figure 2.16, (c)). It may happen that these single-time relaxations overlap and appear as one dispersion. Hence, other more complex models should be considered.
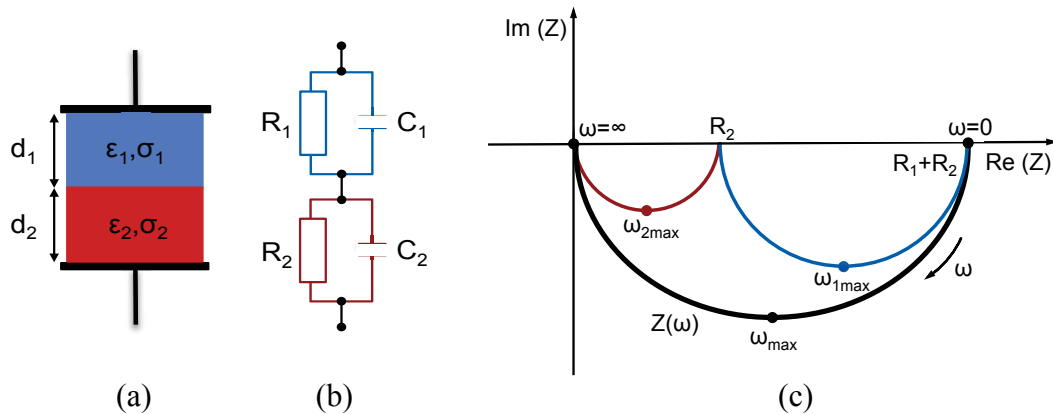
Figure 2.16: (a) A two-layer heterogeneous system; (b) an equivalent circuit model with the parameters: $C_1 = \varepsilon_1 A/d_1$, $R_1 = (1/\sigma_1)d_1/A$; $C_2 = \varepsilon_2 A/d_2$, $R_2 = (1/\sigma_2)d_2/A$; (c) impedance plane plot of two parallel RC circuits in series.

So far very simple models were discussed and presented but they are far too simple to mimic the complexity of dispersions in biological tissues occurring over a wide ranges of frequencies. When an appearance of a spectrum of relaxation processes is identified, then a better agreement with biological systems has been often obtained by incorporation of non-ideal elements that are frequency-dependent. Thus, it is very inconvenient to describe the complexity of the dispersions by using for instance several successive simple Debye-type models. Furthermore, the single dispersion is broader than expected for a simple RC circuit and the impedance plane plot becomes more flattened and has a form of a circular arc with depressed circle centre. Therefore, instead of using a number of simple RC circuits in series, it is more commonly to use the Cole impedance model ([38], [39]) by introducing a "Constant Phase Element" (CPE) with a complex impedance $Z_{CPE} = A(j\omega)^{-\alpha}$, where A is a proportionality factor and α is a factor depending on the nature of the material which may vary between 0 and 1. The CPE impedance is a pure resistance for $\alpha = 0$, capacitive reactance for $\alpha = 1$ and for $\alpha = 0.5$ indicates a diffuse process. Thereupon, the Cole empirical equation gives a nonlinear relationship with the angular frequency.

$$\mathbf{Z} = R_\infty + \frac{R_0 - R_\infty}{1 + (j\omega\tau)^\alpha} \tag{2.3}$$

The response of the Cole-Cole model is a depressed semicircle in the impedance plane (Figure 2.17). The magnitude of this depression is determined by the parameter α, obtaining a complete semicircle when α equals 1. The equation contains three other parameters: R_∞, R_0 and τ, where R_0 is the resistance at very low frequencies, R_∞ is the high frequency resistance and τ is the time constant of the system.
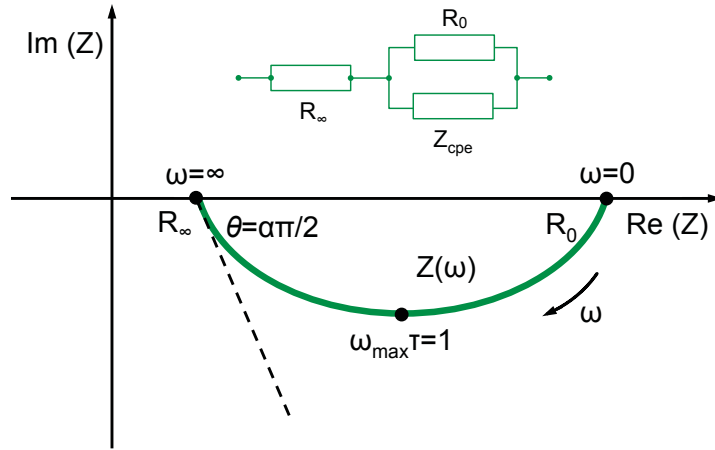
Figure 2.17: An equivalent circuit model (Cole-Cole model) (up) used to mimic the electrical behaviour of tissues characterized by one depressed semicircle impedance arc (down).

2.4.3 Biopotential electrodes

Biopotential electrodes provide the interface between the biomaterial and the electronic measuring circuit. They transduce ionic conduction (electrolyte, body fluid) to electronic conduction (wire, electrode) so that biopotential signals can be viewed, amplified, filtered and recorded. The most common application of the biopotential electrodes is in medical domain used for monitoring heart, brain wave and muscle activity as well as for intra- and extracellular recordings, neurological implantation and bone remodeling. Several major biopotential electrode types are currently used for clinical applications and research purposes each with specific characteristics (form, size and material). Depending on the field of use, the size of bioelectrodes ranges from microscopic intracellular research electrodes (micrometre) to large (3 x 5-inch) defibrillation paddles. The majority of bioelectrodes are made of metal (stainless steel, gold, platinum, titanium), but most microscopic intracellular research electrodes are glass capillary tubes (borosilicate or quartz) filled with a conductive physiological saline solution. A more general overview of the material, geometry, form and application of biopotential electrodes can be found in [51]. Furthermore, the performance of the most commonly used biopotential electrodes in medical domain is compered and evaluated in [52].

Bioelectrical signals are acquired from one of the following four forms of electrodes:

- Body Surface Electrodes (metal plate and disc electrodes, electrodes for Chronic Patient Monitoring (floating and suction electrodes), flexible electrodes)
- Indwelling Electrodes (needle and wire electrodes)
- Electrode Arrays (one dimensional, two dimensional, three dimensional) and
- Microelectrodes (metal, supported metal, fluid filled glass electrodes, microelectrodes based on microelectronic technology)

The fluid filled glass microelectrodes, their geometry as well as their electrical properties are of interest for conducting plausible measurements on biological tissues and performing precise *in silico* studies. Therefore in Chapter 3 a detailed description on the glass capillary formation is presented. In Chapter 4 a model of a glass microelectrode is given and with an *in silico* study the electrical properties of such microelectrode are examined and analysed. The geometry characterization of the micropipettes used for the purpose of the project follows in Chapter 5.

3 Application of bioimpedance in cochlear partition

3.1 Historical perspective

In the early 1950s when von Békésy [53] had presented the first results of measurements of resting potentials inside the cochlear partition, the era of extensive study of electrical properties of the cochlea began. Ever since a great number of experiments have been conducted, electric parameters in various cochlear partitions have been measured and depending on the experimental methods and the animals under observation, immense data of values has been collected.

For instance, Spelman et al. [54], Kumar et al. [55] experimented *ex vivo* whereas Gisselsson [56], Geisler et al. [57], Asakuma et al. [58], Chou and Hellenbrecht [59], Suesserman & Spelman [60] made impedance as well as resting potential measurements *in vivo*. Because the mammalian cochlea is not only very complicated in structure but also not easily accessible for investigation in most species, additionally, *in vitro* techniques have been developed to successfully study its function. As a pioneer in this field of research again the name of von Békésy [61] appears, who performed many important studies using post mortem preparations of the cochlea [62]. Subsequently, this method was accepted, used and continuously refined by others [63], [64].

The most commonly used animal as an experimental model is the guinea pig [37], [54], [56], [57], [58], [60], [65], [66]. It is extensively used for inner ear research due to its simple dissection and similarity in the hearing and vestibular system with human cochlea. However, the dimensions and the structure of the guinea pig cochlea differ from the human one. Furthermore, experiments on macaque monkeys [54], [66] as well on gerbils [55] were conducted.

For *in vivo* experiments, test animals were put asleep with different drugs. Gisselsson [56] used urethane, 6 cm³ of a 25% solution, intraperitoneal, in a combination with Dial in order to keep the middle ear muscular system under control because its contraction during the measurement can lead to false results. Geisler et al. [57] anesthetized the guinea pigs with sodium pentobarbital (Diabutal). A presurgical dose of atropine was used to reduce secretions. Asakuma et al. [58] also used sodium pentobarbital, 35 mg/kg of body weight, administered intraperitoneally and paralyzed with succinylcholine chloride, 15 mg/kg of body weight, intramuscularly. Spelman et al. [54] chose ketamin hydrochloride (100 mg/kg) as anaesthetic for the guinea pigs.

After anesthesia, using topical lidocaine applications, a lateral and ventral surgical approach was used by Geisler [57] to expose the bulla. The bulla was opened and holes were drilled in the wall of the cochlea using either a sharpened hand drill or a fine bit mounted in a dental drill attached to a micromanipulator. After exposing the cochlea, Asakuma [58] made three fenestas in the bony wall of the first turn of the cochlea in order to immerse the two recording electrodes into scala media and the stimulating electrode in scala tympani. The aim was to measure the electrical resistance. For measuring endocochlear potentials *in vivo*, Gisselson [56] drilled a hole in the cochlea so that one can reach the scala vestibuli in the fourth or fifth turn. For his experiments,

von Békésy [53], drilled a small hole in the bony wall just above the Reißner's membrane.

There are several ways for *in vitro* preparation of the cochlea. Ulfendahl [67] introduced isolated guinea pig temporal bone preparation, designed for micromechanical measurements. The acutely excised temporal bone is attached to a holder connecting the auditory duct to a sound system. The entire preparation is immersed in tissue culture medium, and the scala tympani is continuously perfused with oxygenated medium [62]. Gummer et al. [68] used a similar preparation like Ulfendahl [67] with the difference that the middle ear cavity was not immersed and the cochlea was left without perfusion. More recently, another type of *in vitro* preparation has been introduced. The hemi-cochlea preparation allows the observation of the basilar membrane by sectioning of the cochlea along the mid-modiolar plane [62]. Kumar et al. [55] used hemi-cochlea preparation combined with four-electrode reflection-coefficient method for estimating the resistivity of thin cochlear structures which are not easily accessible.

Recording a bioelectrical signal requires the use of two or more electrodes. For measuring DC resting potentials inside the cochlear partition, von Bekesy used glass micropipettes with a tip diameter of about one third of a micron filled with 3M KCl solution (3 molar potassium chloride). Analogously, Gisselson [56], Johnstone and Johnstone [63], Geilsler et al. [57], Asakuma et al. [58], Chou and Hellenbrecht [59], recorded the membrane signals with glass microelectrodes but with different tip dimensions. Spelman et al. [54] used another type of electrodes, namely the nobel metal platinum-iridium which were also used by the experiments of Suesserman et al. [60].

To sum up, for conducting a certain measurement a set of circumstances has to be specified concerning a specific method (*in vivo*, *ex vivo*, *in vitro*), a special measuring electrode configuration (glass microelectrode, nobel metal), the animal under investigation (guinea pig, macaque monkeys, gerbils), the type of membrane preparation and dissection, the location of the measurement (organ of Corti, Reißner's membrane, basilare membrane etc.) and the measured parameter (resting potentials, electrical impedances). Hence, with the years vast collection experimental data has been generated which proves to be difficult to compare because it is experimentally and purpose-oriented.

The above-mentioned facts provided by literature database on measurement of electrical properties of cochlear tissue indicate that this type of measurements conducted in the cochlea are an extremely challenging task and demand a lot of effort theoretically and practically. The basic requirements for accurate measurement data impose a complete understanding of the electrophysiological properties of the tissues and of the measurement configuration as well as the effects that arise from their interaction. Therefore, a new *in vivo* method for measuring electrical impedance changes in the cochlear compartments is highly desirable. To get accurate values of the membrane properties *in vivo*, it is convenient to first experiment on the *in vitro* model devised for this purpose. The primary advantage of such a work is that it permits a great level of simplification of the system under study and can predict its *in vivo* performance.

3.2 Establishment of a novel method

In order to investigate the properties of biological and synthetic membranes a wide range of different methods is available. Among these are optical observation methods, biochemical, molecular biological, biophysical techniques as well as electrical bioimpedance measurements [69]. The latter are explained in detail in this thesis in section 2.4.

To date, one of the most commonly used *in vitro* chamber for measuring electrical impedance changes in tissues is the Ussing chamber [70], initially invented in the 1950s for studying the ion transport through a frog's skin.

However, the Ussing chamber has some certain limitations which restrain optimal conducting of electrophysiological experiments. One substantial problem is the position of the membrane which is vertically stretched in the actual chamber. This makes a simple replacement of the membrane very difficult. Moreover, the positioning of the electrodes on the membrane is challenging. Furthermore, a good optical accessibility to the membrane during the measurements plays a decisive role, which so far does not exist in the Ussing chamber. Hence, the requirements for accurately conducting experiments on biological tissues are not sufficient and satisfying enough.

Therefore, a unique *in vitro* model has been designed and constructed [69] to support the *in vivo* studies on cochlear membranes. The new *in vitro* model consists of a special two plexiglass chamber and a two glass-electrode configuration. The chamber model offers a very simple way of filling, refilling and changing of electrolytes (i.e. representing the endolymph and the perilymph) as well as a possibility to easily apply and remove observed tissues. The two microelectrodes have different tip dimensions, they are made of different types of glass and they are fixed to each other in a certain angle. The principle of modeling is shown in Figure 3.1.
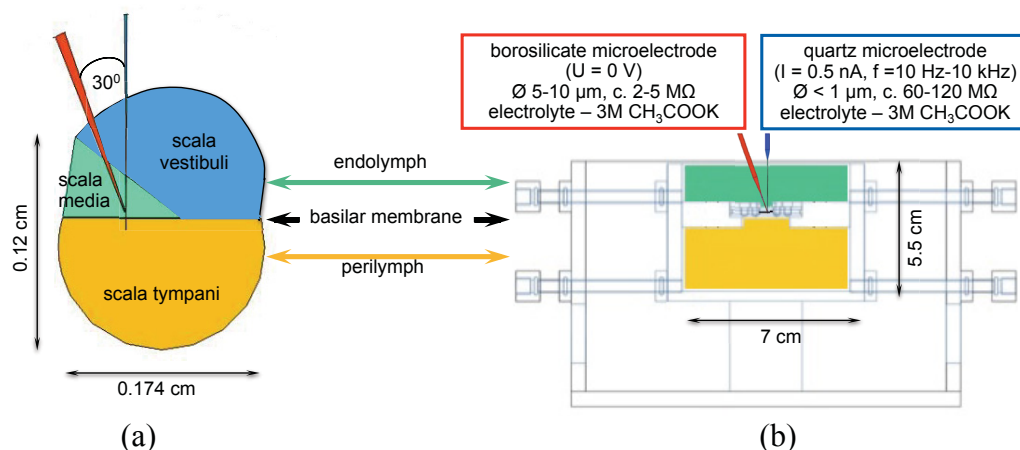
Figure 3.1: The idea behind the principle of *in vitro* modeling of a cochlea and the positioning of the electrode configuration. (a) 2D schematic view of cochlear partition, (b) *in vitro* model of a cochlea [69]: an indifferent electrode is placed just above the membrane (red colour), a second one is pushed through the membrane (blue colour).

3.3 The experimental setup

In this section, the prior mentioned experimental setup depicted in Figure 3.2 is presented. At first, the principle of an *in vitro* modeling of cochlea is introduced including a detailed description of its parts. Moreover essential information about the chosen measurement method and configuration is provided. Secondly, the basic instrumentation, electrode types and their characterizations and fabrications, the composition of electrolyte solutions as well as tissue samples used in conducting the experiments are presented. Eventually, the last subsection is concerned with the inevitable alternations, modifications and upgrades of the experimental setup.
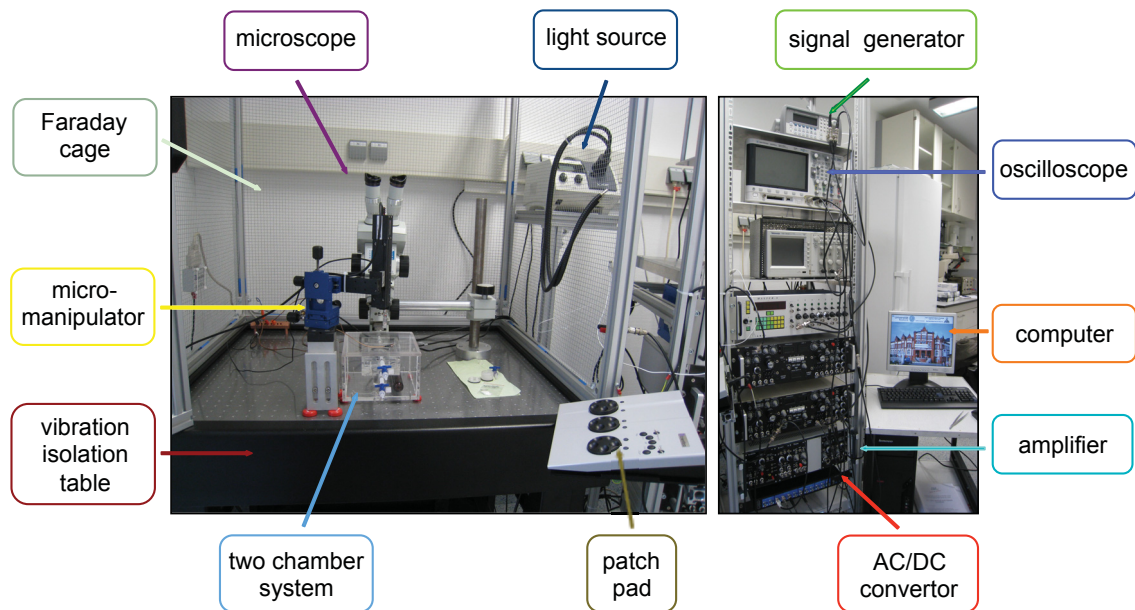
Figure 3.2: The experimental setup at the Institute for Physiology, University of Rostock, Germany (the initial stage). The two panels show the workstation inside the Faraday cage (left panel) and the instrument rack (right panel).

3.3.1 The experimental setup – *in vitro* model of a cochlea and method of choice

The *in vitro* model of a cochlea situated in a Faraday cage is constructed of a plexiglass (polymethylmethacrylat (PMMA)) square shaped chamber system plus a cylindrical membrane holder (Figure 3.3, Figure 3.4), [69]. The system consists of two plexiglass compartments with different dimensions: the smaller one is nested in the bigger one. Additionally, in the outer bigger chamber a temperature slab is integrated that should hold the temperature of the tissue sample to 37 ºC. The smaller chamber is divided into two unequal compartments through a 10 mm PMMA plate that has a cylindrical groove in the middle where the membrane holder is inserted. Both compartments have valves incorporated on one side. Such a chamber design offers a very simple way of separately filling, refilling and changing of the electrolytes that represent the endolymph and the perilymph as well as possibility to easily apply and remove the stretched tissues. Both

chambers are earthed. During the initial measurements (for simplification purposes), in the smaller chamber both compartments are filled with only one type of electrolyte. Its concentration of 4 mM KCl (4 mmol potassium chloride) and 140 mM NaCl (140 mmol sodium chloride) gives the unique ionic composition of the perilymph (later ACSF - artificial cerebrospinal fluid is used). The bigger chamber stays dry and the temperature slab has not been taken in operation.

The membrane holder (Figure 3.4, (b)) is made of two thin discs (material: PMMA, diameter 30 mm) with a hole in the middle (diameter ca. 10 mm) between which a membrane sample can be strained. The lower part is 4 mm thin and on its circumference a sealing ring is mounted which seals the two electrolytes (chamber parts) from each other and ensures the necessary hold in the chamber. The upper part is 2 mm thin and the latter is fixed on the lower with four PMMA screws.

Figure 3.3: A closer look of the measurement chamber with a membrane holder and the respective electrode configuration.

Initially, the measurements are conducted with a two-electrode system (Figure 3.4, (c)). The electrodes have different tip dimensions, they are made of different types of glass and they are fixed to each other at a certain angle. Both electrodes are filled with a composition of 3M CH_3COOK (3 mol potassium acetate) with a pinch of KCl. The shorter thicker electrode, which serves as a bath electrode ($U = 0$ V), is made of a borosilicate glass and should have a tip diameter of 5-10 µm. This microelectrode is brought over the membrane. The longer thinner electrode has approximately 150 µm longer tip than the other electrode and it is made of quartz glass with a tip diameter of < 1 µm. The last one penetrates the membrane, a linear chirp current signal is injected through it and the voltage drop is registered. The injected current and the measured voltage data are the input data for calculation of impedances of biological samples. The obtained results should be afterwards used for computing and deriving the electrical conductivity and electrical permittivity of different membranes.

Originally, synthetic membranes were considered for calibration purposes as well as different types of biological membranes and tissues. In the process of method development, an application on different types of biological membranes and tissues came into question (see 3.3.2.4).

(a)   (b)   (c)
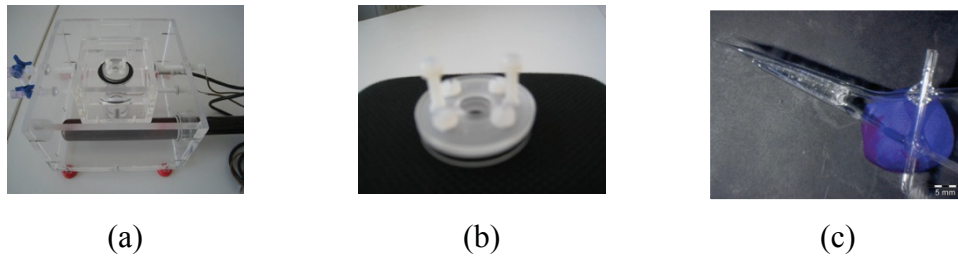
Figure 3.4: (a) A plexiglass chamber membrane holder and the screws, (b) the membrane holder and the screws and (c) measurement configuration (courtesy of O. Specht (IBMT)).

To determine the impedance profile of the membranes impedance spectroscopy is used. A systematic elaboration, verification and validation of the measurements have been carried out and test experiments have been conducted. The ultimate goal includes sophistication of the numerical methods and simulations ensuring good agreement with the experimental data.

3.3.2 The experimental setup – instruments, electrodes and solution

The plausibility of electrophysiological measurements depends on its high reproducibility. Therefore, the choice of methodology, the electronic devices and corresponding software, the properties of the glass micropipettes, the exact electrolyte composition as well as the preparation conditions of the biological tissues are crucial determinants and have a great influence on the measurement results. Thus, the following subsections deal in short with the basic instrumentation, electrodes, electrolyte solution and biological tissues used for conducting the experiments.

3.3.2.1 Electronic instruments and device

The particular experimental setup consists of two parts - the workstation inside the Faraday cage and the instrument rack (Figure 3.2). The newly designed plexiglass chamber together with a microscope (for visualization of the position of the glass electrodes, Carl Zeiss, Technival 2) is placed on a vibration isolation table (TMC-Technical Manifacturing Corporation) within a Faraday cage, where a motorized micromanipulator (Scientifica UI-3200) with an external standard headstage for precise controlling of the movement of the pipette is situated as well. Additionally for driving the micromanipulator, a PatchPad (Scientifica S-PS-800) user interface is integrated that can be computer-controlled (LinLab Software from Scientifica) and allows a smooth movement of an electrode in very small well-defined steps in µm-mm range in the vertical axis. Outside the Faraday cage, very close to the recording stage, the electronic devices are placed in an instrument rack. On the top of the rack, a digital waveform signal generator (Agilent 33220A) is set. For test and observation purposes, the signal generator is connected to an oscilloscope (Agilent DSO-X-2004A) which then again connects directly to the amplifier (npi SEC-10 LX BF [71]) that is operated in bridge mode. At the bottom of the rack, an analog-digital convertor (CED MICRO3 1401) is situated. In order to run it, an application software Signal 4 is installed on a computer (Intel(R) Pentium(R) Dual CPU, E2200@ 2.20 GHz 2.20 GHz, RAM 2 GB) and used

for data sampling, processing and acquisition. Moreover, between the Faraday cage and the instrument rack, a light source (KL 1500 LCD Schott) is placed. All electronic devices are earthed and BNC cables (coaxial cable types that use Bayonet Nut Connector, a quick connect/disconnect radio frequency plug) are used.

The acquisition of accurate measured data depends strongly on the experimental setup and the calibration of the same. Test and tuning procedures are necessary for optimal recordings. Therefore, a passive SEC (Single Electrode Clamp amplifier) cell model [72], [73] is used. The passive cell model is designed for use with single electrode amplifiers to check the function of the instruments. Comparison and optimisation of measured and simulated data is presented in Chapter 5.

3.3.2.2 Glass micro- and bath electrodes

Glass microelectrodes are fabricated from glass capillaries. For this study two different glass types are considered. The longer thinner glass pipette is made of a filament - containing quartz glass (fire polished QF 120-90-10) whereas the shorter thicker glass pipette is drawn from a filament-containing borosilicate glass tube (GB 150-8P) with pre-fire-polished ends.

(a)   (b)
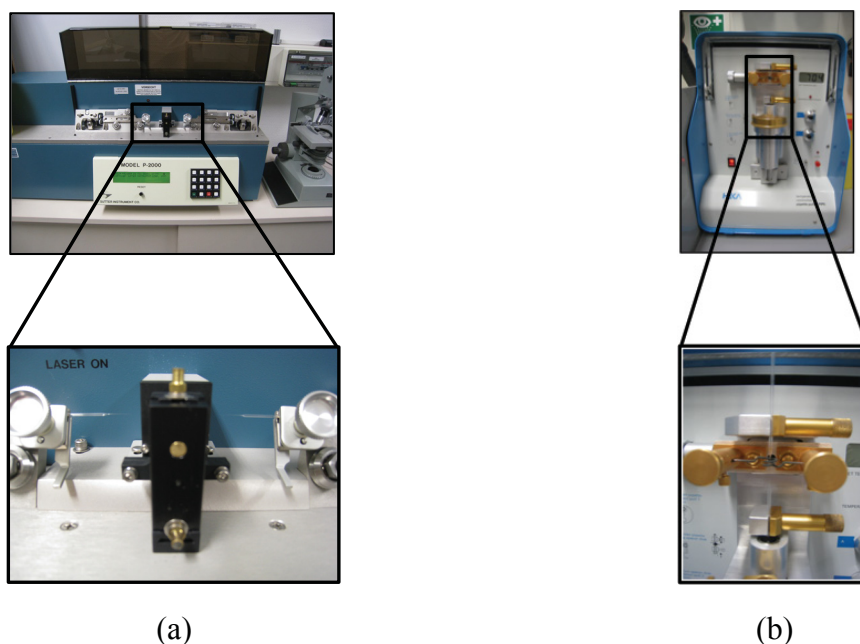
Figure 3.5: (a) A horizontal and (b) a vertical pipette puller (IP).

To fabricate the acquired glass pipettes, horizontal (Sutter Instrument Modell P-2000, quartz tube) and vertical (HEKA P1P5) pipette pullers are used (Figure 3.5, (a) and (b) respectively). The pipette pullers vary in design, but in fact they all work on the same basic principle.

The fabrication process starts with a uniform glass tube which is heated in the middle using a resistive heating element. As the glass is heated, a pulling force is applied along the axis of the tube. As soon as the glass temperature becomes sufficiently high, its viscosity decreases dramatically and the glass tube stretches rapidly. Furthermore, the

tube becomes extremely thin and eventually breaks into two parts [74]. Each half of the tube can be used as an electrode (Figure 3.6).

The desired tip size, taper length and resistance can be reached by adjusting several parameters in the operating program of the puller. Therefore an excellent reproducibility is possible, especially with the horizontal puller.
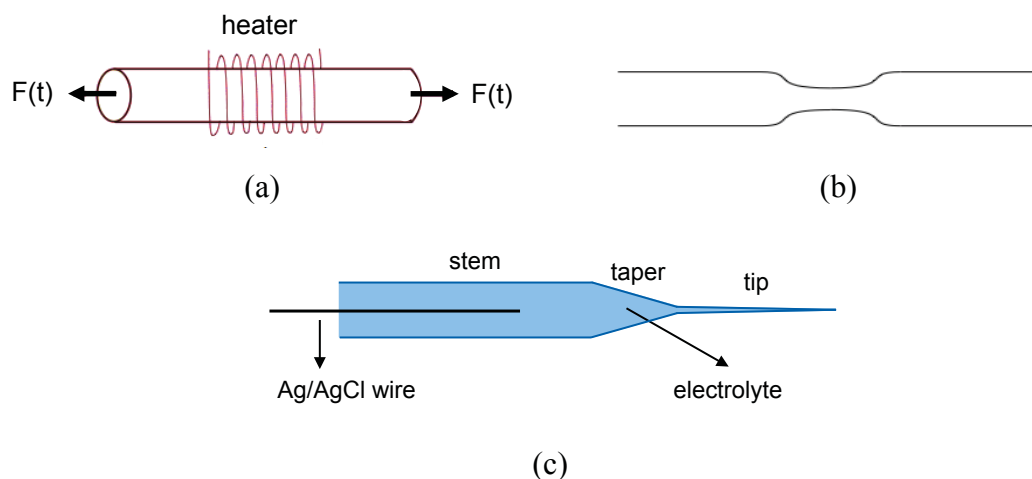
Figure 3.6: The process of glass pipette formation: a) a section of glass capillary; b) a glass capillary narrowed though heating and stretching; c) a final structure of glass microelectrode.

After the fabrication, the borosilicate pipette is slightly bent using gas flame gun and together with the quartz put into the device shown in Figure 3.7. Moreover, under a microscope, with the help of a ruler, the tips of the pipettes are put in the appropriate position to lie in the same plane and the distance between them is 150 μm. Furthermore, the pipettes are fixed to each other (Figure 3.7). For more stability, across the pipettes in the region of the stem (shaft), two or three ca. 3 cm long parts of glass tubes are glued.
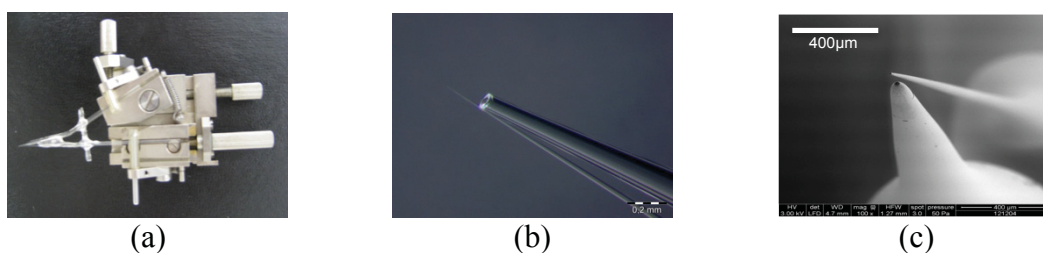
Figure 3.7: The glass microelectrode configuration: (a) the device used for attaching the two pipettes in a certain angle; (b) the difference in positioning of the pipette tips - courtesy of O. Specht (IBMT)); (c) frontal microscope imaging of the pipettes (IBMT).

The last step in making glass electrodes is filling them with salt solution and establishing a connection to the recording circuit. This is made via Ag/AgCl (silver/silver chloride) pellet electrodes which have the role to exchange electrons with Cl^- ions in solution. Through them the current is injected and the voltage is recorded.

In order to provide a return path for the electric current, additionally a bath wire electrode coated with Ag/AgCl (ca. 5 cm long and < 1mm diameter), which is grounded (U = 0 V), is used.

3.3.2.2.1 Geometry of the glass microelectrodes

The drawn glass pipettes are subjected to digital microscope imaging in order to characterize their geometry, the inner and outer diameter starting from the tip till the beginning of the pipette's shoulder millimetre by millimetre. The whole preparation procedure is shown in Figure 3.8. The pipettes are first sawed and then fixed on a sticky patch. Next, the samples are embedded in EpoThin (from Buehler), a mixture of resin and hardener in proportion 2.5:1 (e.g. 25g resin to 10g hardener). Afterwards, the sample should be left to cure for at least 8 hours.

sawing   embedding   grinding and polishing
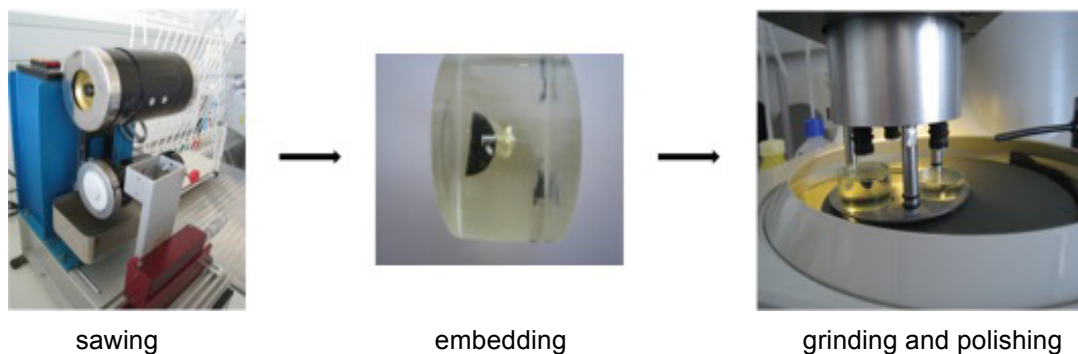
Figure 3.8: Preparation procedure: sawing of the pipette (Well Diamond Wire Saw – Model 3241), embedding of the pipette in Epothin and grinding and polishing of the sample (Struers TegraForce-1 TegraPol-15).

Subsequently, the samples have to be progressively grinded and polished to produce a uniform flat surface. Initially, the samples are wet-treated with 800 grade grit-paper for a minute. Furthermore, the samples are polished with 4000 wet grit-paper (Struers or Buehler) for one more minute.

Figure 3.9: The laser microscope workstation at the IBMT.

Later on, the glass-pipettes sample-diameters and lengths are observed and measured with a digital laser microscope - Olympus LEXT OLS 3000 (see Figure 3.9). Additionally, the two-pipette configuration was subjected to electron microscopy (FEI Quanta^{TM} FEG 250) (see Figure 3.10). The measurements took place at the Institute for Biomedical Technik, University of Rostock.

(a) (b) (c)
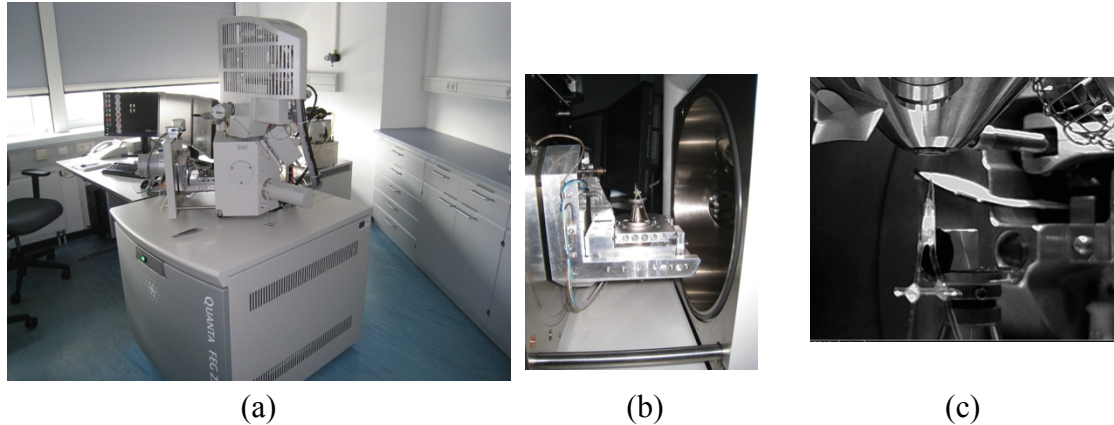
Figure 3.10: (a) The scanning electron microscope workstation at the IBMT; (b) the chamber opening with the pipette sample; (c) camera view inside the vacuum chamber.

Due to incomplete information about the geometry of the pipettes, as a result of damaging of the extremely thin tip of the quartz pipette during transportation and preparation, a second block of microscopy imaging followed. This time the pipettes were separately considered. A polarized light microscope (Zeiss Axio Lab A1) was used for determining the length of both pipettes (several images were made along the length of the samples and subsequently they were properly attached together using GIMP-GNU image manipulation software). A scanning electron microscope (Carl Zeiss SUPRA^{TM} 25 FESEM) was used for characterizing the tiny diameter of the quartz pipette (Figure 3.11). These measurements took place at the Institute of Electronic Appliances and Circuits, University of Rostock.

(a) (b) (c)
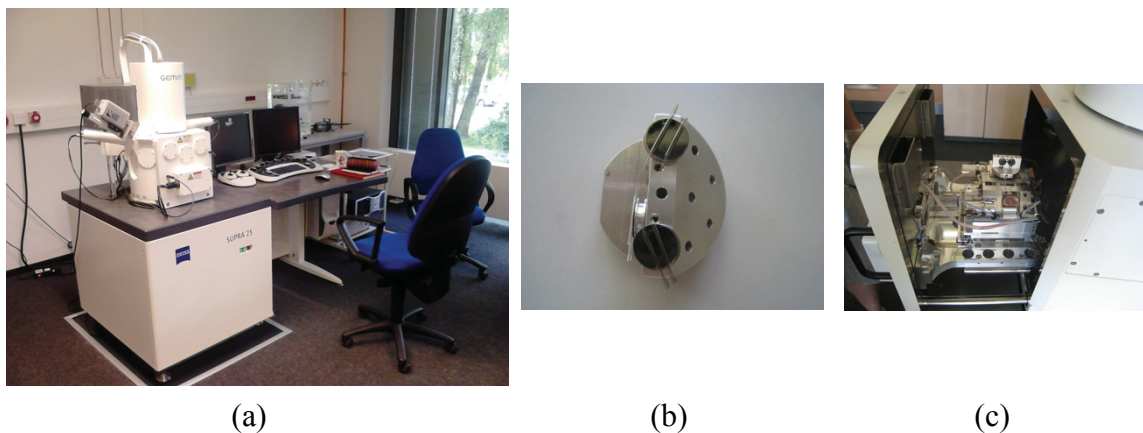
Figure 3.11: (a) The scanning electron microscope workstation at the IEAC; (b) four pipette samples; (c) the specimen chamber with the samples.

3.3.2.3 Solution

For the purpose of this study three different aqueous solutions were made. The first electrolyte represents the artificial perylimph and it is used for filling the chambers. Its concentration of 4 mM KCl (0.298 g/l potassium chloride) and 140 mM NaCl (8.1942 g/l sodium chloride) gives the unique ionic composition of the perylimph. Later for the measurements with biological tissues an ACSF with the following composition was used in both chambers: 124 mM NaCl (7.2466 g/l), 26 mM NaHCO3 (2.1843 g/l), 3 mM KCl (0.2237 g/l), 1.25 mM NaH2PO4 (0.1500 g/l), 2.5 mM CaCl2 (0.3676 g/l), 1.3 mM MgCl2 (0.1238 g/l) and 10 mM Glucose (1.8016 g/l).

The fabricated glass capillaries were filled with an aqueous composition of 3M CH$_3$COOK (0.2942g/ml potassium acetate) mixed with 300 mM KCl which gave final resistance of approximately 70 MΩ when both glass electrodes are fixed to each other. The filling solution is filtered by using a syringe filter. After filling, the glass pipettes are put for some hours in a vertical position to remove possible bubbles.

All electrolytes are prepared with distilled water. The whole preparation procedure took place at the Institute of Physiology, University of Rostock.The conductivity of all used electrolytes is measured at a temperature of 25 °C (Eutech PC 510, IEAC).

3.3.2.4 Tissue sample

Originally, impedance measurements on synthetic membranes should have been conducted. These membranes should have been used for calibration. Unfortunately, the three types of synthetic membranes that were considered (Optitran BA-S83, Cellulosenitrate E and P PVDF) were too stiff so that the tiny tip of the quartz electrode did not go through. It broke while penetrating the membranes.

Furthermore, in the process of the method development an application on biological membranes was considered. The decision and choice of a suitable membrane (tissue) was very challenging because several criteria had to be fulfilled. In the end, the mesentery of a rat was chosen.

The mesentery is a double-layered fan-shaped peritoneal fold with some connective tissue that anchors the intestines to the back of the abdominal wall. It contains a branch of blood vessels, lymph nodes and nerves that supply the intestines and at the same time helps to keep those organs in place allowing a certain mobility of the same [75], [76].

For the purpose of this study mesentery of albino Wistar rats was examined. This breeding line of the species Rattus norvegicus (brown rat) is a standard animal model for scientific research. The tissue was taken from both male and female albino rats aged two to four months.

The rat was dissected and the mesentery was prepared on the day of interest several hours before the measurements took place. From one rat it was possible to get 3-4 intact samples. For this purpose, the lower part of the membrane holder was placed under the mesentery of the rat. The upper part was placed above it and in this way the tissue was fixed in the membrane holder (Figure 3.12, (b)). The upper and lower parts were screwed together with 4 screws. With a scalpel, the tissue was carefully cut off along the side of the membrane holder. The prepared tissue was stored in nutrient solution (ACSF) cooled and buffered (bicarbonate buffer - 95% CO$_2$ and 5% O$_2$) in order to maintain the pH until it was placed in the measuring chamber (Figure 3.12, (c)).

The sample preparation took place at IP.

<div align="center">(a)　　　　　　　　　　(b)　　　　　　　　　　(c)</div>
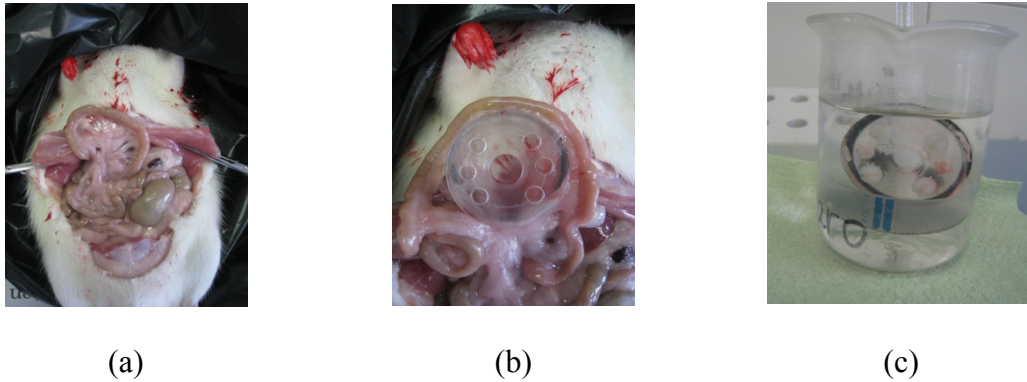
Figure 3.12: (a) Rat dissection; (b) focus on the rat mesentery and the preparation of the sample; (c) the mesentery sample in a nutrient solution.

To determine the tightness and thickness of the tissue, tissue samples were examined under a laser scanning angiography microscope from Heidelberg Engineering. Images of the samples were made in different field depths. The images (see Chapter 5) were taken at the Department of Experimental Ophthalmology, University of Rostock [77].

3.3.3　The experimental setup - modifications

Throughout the experiments many obstacles had to be overcome in order to obtain feasible *in vitro* experimental data. The initial design has undergone several inevitable modifications. Firstly, the amplifier, as well as the pipette holder (a low noise headstage [73] was directly attached to the micromanipulator), had to be changed to extract the influence of possible uncompensated capacitance coming from the electronic devices. Additionally, a different type of amplifier (Lock-In SR830) was included to extrude the influence of undesired frequencies in the measurements. This amplifier was directly connected to the npi SEC-10 LX BF operating in time domain. Moreover, the output data was in frequency domain and thus a simplified and faster data analysis was achieved. More information and details about the operation and control of the devices as well as the signal flow can be found in Chapter 5 and in the bachelor work by Richard Kosub made in the frame of this project [77]**.**
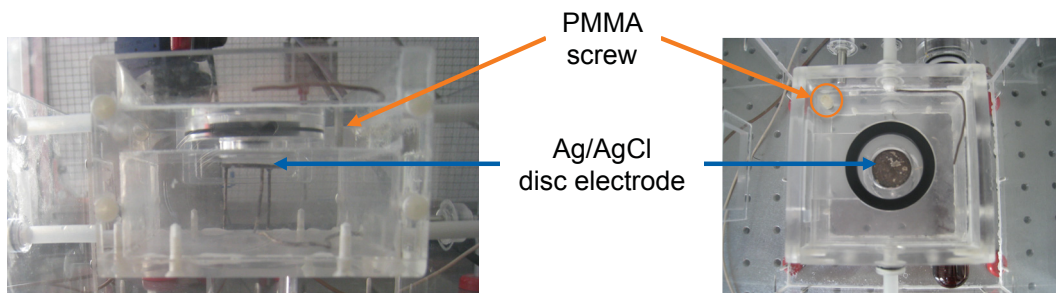
Figure 3.13: Position and form of an additional Ag/AgCl bath electrode; the PMMA screw implemented for pressure equalisation.

Secondly, the *in vitro* system underwent minor alterations and inclusion of a third electrode (Ag/AgCl-disc-electrode with Ø 2cm) was foreseen (Figure 3.14). For supporting the stability and accurately positioning of the electrode directly under the membrane, on one side of the disc electrode three Ag/AgCl wire legs were fixed so that a stable stool structure was formed with a total height of ca. 2.5 cm. This structure was carefully positioned at the bottom of the chamber and one wire leg was earthed.

In the lower chamber after membrane emplacement, a fluid compression appeared. Therefore, a hole was drilled in the plexiglass wall between the lower and upper chambers to equalise the pressure and prevent membrane damage. Afterwards, the hole was closed with a plexiglass screw (see Figure 3.14). Next, to be able to conduct several measurements sequentially, 10 membrane holders with two different diameter openings (0.5 cm and 1cm) were made. In addition, a cylindrical tissue holder was made. As it can be seen from Figure 3.14, (a), the cylindrical tissue holder has the same diameter as the original one and the membrane opening remained unchanged. It consists of three parts (Figure 3.14, (c)) and it was intended to perform impedance measurements on cell cultures growing on a thin film spanned on the end of a glass tube (Figure 3.14, (c) - the glass tube on the left). The glass tube is inserted at the bottom of the tissue holder (on its circumference a sealing ring is mounted which seals the chamber parts and ensures the necessary hold in the chamber). The upper cylindrical part (height ca. 1 cm) is then screwed to the lower part. When using this type of tissue holder, it is not necessary to fill the upper chamber with electrolyte. Through the opening in the cylindrical holder, electrolyte can be filled in and then again the same conditions as in the original model can be achieved, above and under the observed probe is an electrolyte. This new type of tissue holder has not been used for experiments yet, because a suitable biological membrane has been found (see 3.3.2.4).

(a)

(b)

(c)

(d)
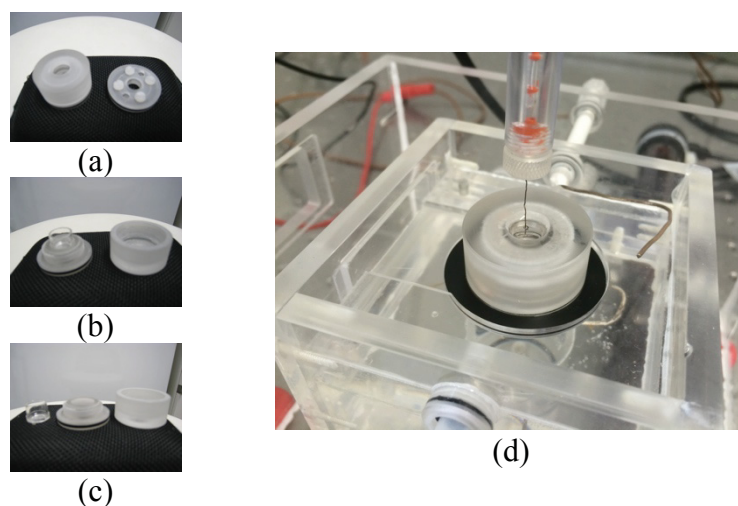
Figure 3.14: (a) The new type of cylindrical tissue holder (left) and the original membrane holder (right). (b) and (c) three different parts of the new type of holder. (d) The cylindrical tissue holder inserted in the *in vitro* chamber.

Furthermore, test experiments with different two-electrode system were conducted - thick borosilicate glass-electrode (the pipette dimensions remain the same as in the

original electrode configuration) was positioned over a membrane against a disc Ag/AgCl bath electrode put directly under the membrane.

Subsequently, a newly designed Ussing-like chamber (Figure 3.15, (a)) with a membrane holder (opening ca. 0.8 mm, thickness ca. 5 mm, Figure 3.15, (c)) and two Ag/AgCl wire electrodes (Figure 3.15, (b), top view) was taken in consideration to support the validity of the impedance measurements carried out with the glass-microelectrode configuration.

(a)   (b)

(c)
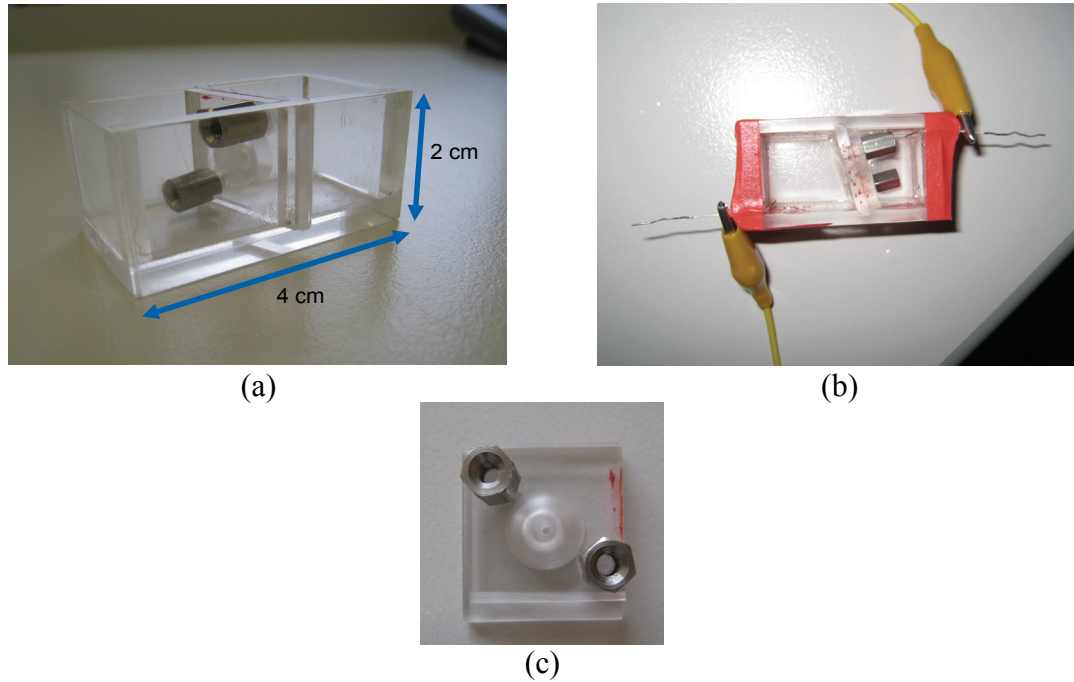
Figure 3.15: The newly designed Ussing-like chamber at the CB in cooperation with the IP.

The idea of such a chamber arose in cooperation with the Institute of Physiology and the Chair of Biophysics at the University of Rostock. The prototype of the chamber is already built and ready to be used, however, due to lack of time only numerical simulations have been carried out. The *in silico* model is described in Chapter 4 and the numerical results are presented in Chapter 5.

4 *In silico* model of the *in vitro* experimental setup

The *in vitro* experimental setup is modelled and simulated in COMSOL Multiphysics® 4.2 (*http://www.comsol.com*). The software package can solve for electromagnetic, thermal, mechanical and many other disciplinary problems and multiphysical problems, as well. For electromagnetic problems, it numerically computes differential equations derived from the Maxwell's equations. Numerically, the package is built upon the Finite Element Method (FEM). Therein, as a problem-specific module the AC/DC module was chosen for 2D axisymmetric and 3D numerical simulations. This module provides several interfaces with different study types that enables an easy definition of the concrete problem and calculation of output parameters in frequency, time or stationary domains. Furthermore, self-written codes in MATLAB® are used for parameter identification and Fourier analysis.

Additionally, several different lumped parameter models of the *in vitro* experimental setup were created, studied and analysed in MATLAB®/Simulink® R2011b/R2013b (*http://www.mathworks.com*) in both time and frequency domain. Therefore, a special suite of MATLAB®/Simulink® Toolboxes™ was implemented. The models mimicry the *in vitro* environment and allow exceptionally good evaluation and comparison of simulated and measured impedance values. The lumped parameter models in MATLAB®/Simulink® were also very useful in the process of calibration, verification and validation of the instruments.

4.1 Short introduction to Maxwell's equations and their numerical solutions

Maxwell's equations are a set of four partial differential equations (Gauss' law for electric fields, Gauss' law for magnetic fields, Faraday's law of magnetic induction and Ampere's law with Maxwell's extension) that capture the electromagnetic fields arising from varying distributions of electric charges and currents, and the change of these fields in time. The Maxwell's equations are the basis of many numerical methods developed for calculating electromagnetic fields.

There are four central physical quantities that are coupled in the Maxwell's equations. These are the *electric field strength* $\mathbf{E}$ [V/m], the *electric displacement field* $\mathbf{D}$ [C/m^2], the *magnetic field* $\mathbf{H}$ [A/m], the *magnetic flux density* $\mathbf{B}$ [T = Vs/m^2] along with the *current density* $\mathbf{J}$ [A/m^2].

The set of Maxwell's equations can be written in integral and differential form, respectively. Both formulations are mathematically equivalent and the relations arise as a consequence of the Gauss divergence theorem and Kelvin-Stokes theorem. The differential form is presented here and used for the numerical modeling and simulation throughout the thesis.

To summarize, the four Maxwell's equations in differential form have the following representation and interpretation:

Gauss' law for electric fields:	$div\ \mathbf{D} = \rho$	(4.1)
Gauss' law for magnetic fields:	$div\ \mathbf{B} = 0$	(4.2)
Faraday's law of magnetic induction:	$curl\ \mathbf{E} = -\partial\mathbf{B}/\partial t$	(4.3)
Ampere's law with Maxwell's extension:	$curl\ \mathbf{H} = \partial\mathbf{D}/\partial t + \mathbf{J}$	(4.4)

The Gauss' law for electric fields (4.1) and Gauss' law for magnetic fields (4.2) define the sources of the electric displacement field and magnetic induction: the flux of **E** through a closed surface is equal to the enclosed charge ρ and the net magnetic flux **B** out of any closed surface is zero (no magnetic charge exists: no "monopoles"). The coupling of the electric and magnetic field is given in Faraday's law (4.3) and Ampere's law (4.4): a time-varying magnetic field generates an electric field whereas a time-varying electric field and/or electric current generate a magnetic field.

The above-described set of four Maxwell's equations has to be extended with three additional equations, the constitutive material equations. In case of a linear and isotropic media, they are given by:

$$\mathbf{D} = \varepsilon_0\varepsilon_r\mathbf{E} = \varepsilon\mathbf{E} \qquad (4.5)$$
$$\mathbf{B} = \mu_0\mu_r\mathbf{H} = \mu\mathbf{H} \qquad (4.6)$$
$$\mathbf{J} = \sigma\mathbf{E} \qquad (4.7)$$

where the material characteristics are defined as $\mu_0 = 4\pi\cdot10^{-7}$ [Vs /Am] - *permeability of free space*, $\varepsilon_0 = \frac{1}{c_0^2\mu_0} \approx 8.854\cdot10^{-12}$ [As/Vm] - *permittivity of free space* whereas, μ_r is the *relative permeability* and ε_r the *relative permittivity*, σ is the *electrical conductivity*. The material properties may depend on space, time and temperature.

In this study, the frequency-domain (time-harmonic) wave equations are needed. When a problem is time-harmonic the electric fields can be written as:

$$\mathbf{E}\ (\boldsymbol{r},t) = \mathbf{E}\ (\boldsymbol{r})\ cos\ (\omega t + \theta) \qquad (4.8)$$

with the angular frequency ω and the phase angle θ.

Commonly, instead of using a cosine function for the time dependence, it is more convenient to use an exponential function $e^{j\omega t}$. The electric field can be expressed as:

$$\mathbf{E}\ (\boldsymbol{r},t) \rightarrow \mathrm{Re}\ (\underline{\mathbf{E}}\ (\boldsymbol{r})e^{-j\omega t}) \qquad (4.9)$$

where $\underline{\mathbf{E}}(\boldsymbol{r}) = |\mathbf{E}|\ (\boldsymbol{r})e^{-j\theta}$ is a phasor containing amplitude and phase information.

The derivative of $e^{j\omega t}$ with respect to time is $j\omega e^{j\omega t}$. Hence, the Maxwell's equations can be easily transformed to the frequency-domain by replacing the time derivative $\partial/\partial t$ with $j\omega$. Then, the time-harmonic equations get the form:

$$div\ \underline{\mathbf{D}} = \rho \qquad (4.10)$$
$$div\ \underline{\mathbf{B}} = 0 \qquad (4.11)$$
$$curl\ \underline{\mathbf{E}} = -j\omega\underline{\mathbf{B}} \qquad (4.12)$$
$$curl\ \underline{\mathbf{H}} = j\omega\underline{\mathbf{D}} + \sigma\underline{\mathbf{E}} + \underline{\mathbf{J}}_{\mathbf{i}} \qquad (4.13)$$

where the current density $\underline{J}$ is composed of a conduction current density $\underline{J}_c$, arising from conductive materials and an impressed current density $\underline{J}_i$, assuming there is no current of free charges.

If the operators $\nabla = grad$ (gradient operator), $\nabla \cdot = div$ (divergence operator) and $\nabla \times = curl$ (curl operator) are introduced, the so-called point-form of the differential Maxwell's equations is obtained:

$$\nabla \cdot \underline{D} = \rho \tag{4.14}$$
$$\nabla \cdot \underline{B} = 0 \tag{4.15}$$
$$\nabla \times \underline{E} = -j\omega\underline{B} \tag{4.16}$$
$$\nabla \times \underline{H} = j\omega\underline{D} + \sigma\underline{E} + \underline{J}_i \tag{4.17}$$

This form is used to facilitate the understanding of the denotations used in the equations applied in COMSOL Multiphysics®.

4.1.1 Time-harmonic electro-quasistatic formulation

For the electrode-electrolyte-membrane studies, the complexity of the problem can be greatly simplified by applying the electro-quasistatic (EQS) approximation for slowly varying electromagnetic fields. Generally, besides electro-quasistatic, the magneto-quasistatic (MQS) approximations can be defined. To decide which approximation is appropriate for a given problem, the relation between charge relaxation time $\tau_e = \varepsilon/\sigma$, current density diffusion time $\tau_m = \mu\sigma d_s^2$, electromagnetic transit time $\tau_{em} = \sqrt{\tau_e\tau_m}$, angular frequency $\omega = 2\pi f$ of the given problem as well as the studied system dimension d_s has to be considered. If the study includes sources that vary sinusoidally with frequency ω, then if $\omega \approx 1/\tau_e$ holds, the EQS approximation is suitable, whereas if $\omega \approx 1/\tau_m$, the MQS approximation has to be used [79].

The EQS approximation is only valid when the studied geometry is considerably smaller than the wavelength. The criterion that has to be fulfilled is $|kd_s| << 1$, where k is the wave number defined as $k = \omega\sqrt{\mu\varepsilon\left(1 - j\frac{\sigma}{\varepsilon\omega}\right)}$ [28], [80]-[82]. If this is the case then the wave propagation phenomena can be neglected. Hence, the inductive phenomena are disregarded, whereas capacitive and resistive phenomena are taken into account. When reducing the model to an EQS problem, the following assumptions are being valid: the magnetic flux is assumed to be negligible ($\partial\underline{B}/\partial t = 0$) and displacement currents are taken into account ($\partial\underline{D}/\partial t \neq 0$). The equations to be solved become:

$$\nabla \cdot \underline{D} = \rho \tag{4.18}$$
$$\nabla \cdot \underline{B} = 0 \tag{4.19}$$
$$\nabla \times \underline{E} = 0 \tag{4.20}$$
$$\nabla \times \underline{H} = j\omega\underline{D} + \sigma\underline{E} + \underline{J}_i \tag{4.21}$$

According to the EQS assumptions, the electric field $\mathbf{E}$ is free of eddy currents (4.20) and can be described as the gradient of a complex scalar potential:

$$\underline{\mathbf{E}} = \textit{-grad } \underline{V} \tag{4.22}$$

Combining equation (4.22) with the electro-quasistatic equation (4.21) and (4.5), after several mathematical manipulations [81], the following reformulated potential equation can be derived:

$$\triangledown \cdot \left[(\sigma + j\omega\varepsilon_0\varepsilon_r)\triangledown\underline{V} \right] = \triangledown \cdot \underline{\mathbf{J}}_{\mathbf{i}} \tag{4.23}$$

This equation provides the voltage field in the frequency domain when current sources that vary sinusoidally with frequency ω are used and it is the governing equation used for the numerical simulations.

For numerical evaluation of the electromagnetic fields, several discretization methods can be implemented among which are the Finite Integration Technique (FIT), Boundary Element Methods (BEM), Finite Difference Method (FD) and the Finite Element Method (FEM). They are applicable for numerical problems in time and frequency domains and based on the discretization of Maxwell's equations. In the Finite Element Method, the unknown solution is approximated by a function in a finite dimensional space [80].

4.2 FEM and its basic principles

This section gives only a succinct overview and introduces some important notations since there exist plenty of textbooks on FEM and the method itself was not the focus of the research reported here.

The Finite Element Method (FEM) is a variational approach to solve Maxwell's equations in their differential form (4.1) - (4.4) on a discretized geometry. In general, there are two different types of problems based on partial differential equations, initial and boundary value problems. After discretization, the final linear system of equations or eigenvalue problems are a discrete analogue to the Maxwell's equations. The time and space discretized fields can be used for efficient numerical simulations of electromagnetic problems in complex geometries.

Generally, the procedure of discretization and solving of a certain problem by the FEM is achieved following several basic steps [80], [83].

To start with, a certain computational domain is defined within which the Maxwell's equations are solved. This domain includes the geometry under study divided into finitely many non-overlapping elements (elements or grid cells) interconnected at nodes and edges. Typically, the FEM discretization employs unstructured grids. The advantage of this is that the elements do not need to be the same size. Common elements for a 2D domain are triangles or rectangles and for a 3D domain tetrahedra and hexahedra. On each single element, a local basis function is defined and a weak formulation of the problem is derived. The basis functions are normally low-order polynomials that are nonzero and expressed as functions of the node positions in case of nodal elements. The same process is applied to all elements and boundary conditions are imposed. The simple equations that model the finite elements are then assembled into a larger system of equations that models the entire problem. Thus, a global system matrix of equations (stiffness matrix) is formed. Eventually, the system of linear

equations is solved using linear algebra techniques. The solution of the system of algebraic equations gives an approximation of the solution to the partial differential equations. The denser the mesh, the closer the approximate solution gets to the actual solution. Another possibility is the use of higher order elements.

For this study, the COMSOL Multiphysics® implementation of the FEM is considered.

4.3 FEM model

The finite element computations of the *in vitro* experimental setup are carried out with the commercial software COMSOL Multiphysics® 4.2. Models of both single glass microelectrode (2D and 3D) and two glass microelectrodes (only 3D) submersed in a physiological electrolyte solution are constructed (Table 1). Next, the whole experimental setup is modelled including the two electrodes, the membrane holder (with and without stretched membrane) and the complex chamber (3D simulations). In addition, two other model modifications of the *in vitro* model were considered (Table 2). Eventually, a model of the newly designed Ussing-like chamber with a membrane holder and two-electrode configuration was completed (Table 3). For this purpose two interfaces in the AC/DC module in COMSOL Multiphysics® are used: Electric Currents (stationary and frequency domain study) and Electrostatics (stationary study).

For these problem types, a linear system of equations results from the FEM application. This linear system is solved using an iterative solver, BiCGStab with a Multigrid preconditioner and a relative tolerance of $1 \cdot 10^{-6}$, in a range of test frequencies varied from 0 to 1 GHz, by applying a current with amplitude I_0.

Computed values of electric potential and impedance in the above given frequency range are of interest.

4.3.1 Model of a glass microelectrode

In order to gain a particular knowledge of the properties of the *in vitro* system, the model has been gradually studied. Initially, a model of one fluid-filled glass microelectrode immersed in a salt solution was designed (Figure 4.1) which contributed for a better understanding of the electrical properties of such microelectrode. Therefore, the glass microelectrode is modelled as an upside-down truncated cone representing the tip of the electrode with a base (tip) radius r_b, an apex radius r_a and height (tip length) h filled with an electrolyte solution ($\varepsilon_r = 109$; $\sigma = 2$ S/m) and immersed into a cylindrical chamber filled with the same aqueous solution. The base of the electrode is placed flush with the upper end of the cylinder. Consequently, appropriate boundary conditions are assigned. The surface of the cylinder is defined as insulating, while on its bottom the ground boundary condition (voltage $U = 0$ V) is applied. The surface of the microelectrode that lies flush with the end of the cylinder is defined as a current source (terminal). For the boundaries on the symmetry axis (green dashed line, Figure 4.1), condition for axial symmetry applies.
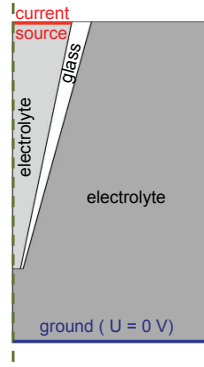
Figure 4.1: A 2D - model of a glass electrode tip immersed in an electrolyte-filled cylindrical chamber.

Two models are considered. In the first one, the glass thickness of the microelectrode is incorporated (dielectric properties of the glass: $\varepsilon_r = 4.2$; $\sigma = 1 \cdot 10^{-12}$ S/m), linearly increasing from the apex to the base of the truncated cone. The second model includes the thickness of the glass as a thin layer approximation, by using special boundary condition (contact impedance), specified with the material conductivity, permittivity and thickness d_l. This boundary condition assumes that all currents flowing through the layer have only a normal component:

$$\mathbf{n} \cdot \mathbf{J_1} = (\sigma + j\omega\varepsilon_0\varepsilon_r)\,\frac{V_1 - V_2}{d_l}$$

(4.24)

$$\mathbf{n} \cdot \mathbf{J_2} = (\sigma + j\omega\varepsilon_0\varepsilon_r)\,\frac{V_2 - V_1}{d_l}$$

where the indicies 1 and 2 refer to the two sides of the boundary.
The advantage of such kind of approximation is the reduction of the number of mesh elements. Hence, a gain in computation time and memory can be achieved.
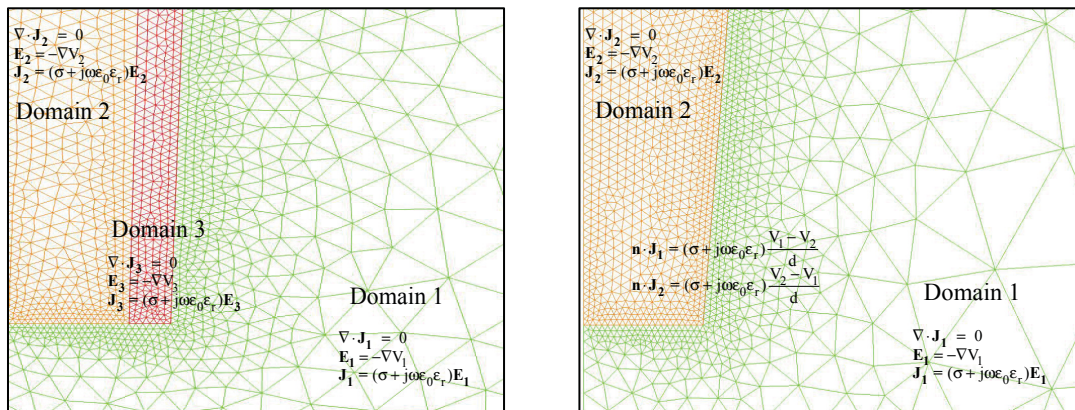
Figure 4.2: Governing equations for the three domains for a 2D-model with incorporated glass thickness (left; 87,263 mesh elements) as well as for the two domains and the boundary condition for the 2D-model with thin layer approximation (right; 6,1971 mesh elements).

To confirm the validity of the single glass microelectrode FEM-models, values for the resistance and capacitance were computed. According to [85] and [87], the whole resistance of the glass-microelectrode is concentrated at the tip region of the electrode, whereas the capacitance, which arises as a consequence of the glass wall behaving as a dielectric surrounded by electrolytes that act as conductors, is distributed along its length. Besides, it has been reported that the capacitance of a microelectrode is in agreement with the one given by the relation for the capacitance of a cylinder under the assumption that the ratio between the outer (r_2) and inner radius (r_1) remains constant over the length [87]. The capacitance per unit length is given by the expression:

$$C' = \frac{C}{l} = \frac{2\pi\varepsilon_0\varepsilon_r}{\ln\frac{r_2}{r_1}} \tag{4.25}$$

Moreover, the resistance of fluid-filled glass microelectrode tip submerged in the same electrolyte solution up to a length l can be quantitatively described as follows [94]:

$$R_{tip} = \frac{\rho}{\pi\cdot\tan^2(\alpha)}\left(\frac{2\cdot\tan(\alpha)}{d_t} - \frac{1}{1 + \frac{d_t}{2\cdot\tan(\alpha)}}\right) \tag{4.26}$$

where the resistivity of the filling fluid is ρ, the tip angle is α and the tip diameter is d_t.

electrode type	tip geometry		filling solution		bathing solution	
	diameter [μm]	conical angle [rad]	material properties		material properties	
			σ [S/m]	ε_r	σ [S/m]	ε_r
low resistance microelectrode	40	0.1	2	109	2	109
	5	0.1	2	109	2	109
	5	0.025	2	109	2	109
	5	0.025	30.3 | 1	80	30.3 10 1 0.3 0.2 0.148 0.11	80
high resistance microelectrode	0.5	0.025	30.3 | 1	80	30.3 10 1 0.3 0.2 0.148 0.11	80
	0.1	0.05				
two-electrode configuration	10	0.0225	2	109	2	109
	1	0.005				
	10	0.0225	34.3	80	2	109
	1	0.005				

Table 1: Types of models of a fluid-filled glass microelectrode, their geometry and the material properties of the filling and bathing solution.

Equation (4.26) is valid only if the properties of the inside and outside solutions of the microelectrode are the same ($\rho_i = \rho_o$).

In fact, due to the simple model geometry of the electrolyte-electrode system, analytical solutions (using equations (4.25) and (4.26)) could be calculated and thus the numerically computed solutions validated. Importantly, a convergence study was performed by decreasing the mesh element size (2D-triangular mesh and 3D-tetrahedral mesh). 2D-simulations showed that even with a relatively course mesh (3278), less than 0.025% relative deviation to the analytical solution of the resistance and 0.068% of the capacitance was reached.

Finally, comparison of the impedance considering the thickness of the glass and incorporating the thin layer approximation was carried out. The maximum relative difference of the absolute value and phase of the impedance was 0.4% and 0.7%, respectively.

4.3.2 Model of the *in vitro* experimental setup

Taking into account the properties of an ideal glass microelectrode-electrolyte interface, a 3D model of the *in vitro* chamber with all its compartments and a two-electrode system has been built. The model contains six different domains that comply with the real geometry (Figure 4.3 and Figure 4.4).
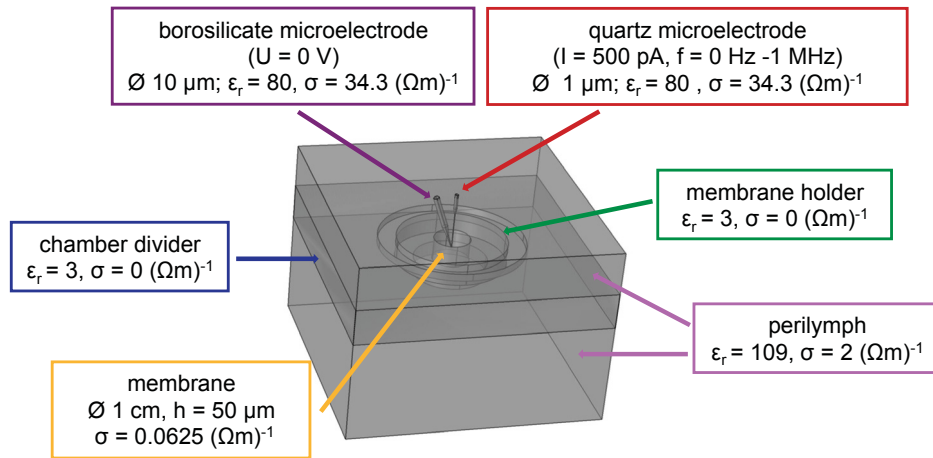
Figure 4.3: A 3D-model of the *in vitro* experimental setup showing the different components as well as their material properties and dimensions.

Originally, a 7 x 5.5 x 7 cm^3 block filled with an aqueous solution representing the perilymph (ε_r = 109; σ = 2 S/m [28]) was built. Next, inside of this box at a 1.2 cm distance down from the top, a chamber divider was placed, defined as a PMMA (plexiglass - ε_r = 3; σ = 0 S/m) block with dimensions 7 x 1 x 7 cm^3. In the middle of the chamber divider, starting from its top, circular stair structures (first step 0.2 cm deep, second step 0,4 cm deep) were formed which ended with an opening (hole Ø 2 cm) on its bottom. Over this, the membrane holder is placed. The membrane holder is modelled as a PMMA cylinder, Ø 3 cm and 0.6 mm high, with a hole in the middle (Ø 1 cm and 0.6 mm high). 2 mm down from the top of the membrane holder, the membrane is

positioned (Ø 1 cm and 50 μm high; ε_r = 80; σ = 0.0625 S/m [95]). The glass pipettes are modelled consisting of three parts - cylindrical part (shaft) and two conical parts representing the taper and the tip, respectively, and filled with an electrolyte (ε_r = 80; σ = 34.329 S/m, analytically calculated value for the pipette electrolyte: $\sigma = \lambda$ (molar conductivity) $\cdot$ c (electrolytic concentration). The thinner glass pipette (tip: Ø 1 μm, $\alpha_1 \approx$ r_{b1}/h_1 = 0.005 rad; taper: Ø 100 μm, α_2 = 0.225 rad; stem: Ø 900 μm, h_3 = 0.3 cm) is positioned in the middle of the membrane holder whereas the thicker shorter pipette (tip: Ø 10 μm, α_3 = 0.025 rad; taper: Ø 200 μm, α_4 = 0.143 rad; stem: Ø 860 μm, $h_5 =$ 0.8 cm) is rotated 20° with respect to the latter. The distance between the tips of the pipettes is approximately 150 μm. The thinner glass pipette is pushed through the membrane and is positioned ca. 50 μm under the membrane. Hence, the thicker glass pipette is positioned ca. 50 μm above the membrane. The bases of the electrodes are placed flush with the upper end of the chamber. Consequently, appropriate boundary conditions are assigned. The surface of the chamber is defined as insulating. The surface of the microelectrode that lies flush with the end of the cylinder is defined as a current source (terminal) whereas on the surface of the thicker electrode ground boundary condition is applied (U = 0 V). Instead of incorporating the glass thickness, the thin-layer approximation is assigned to the pipette walls.
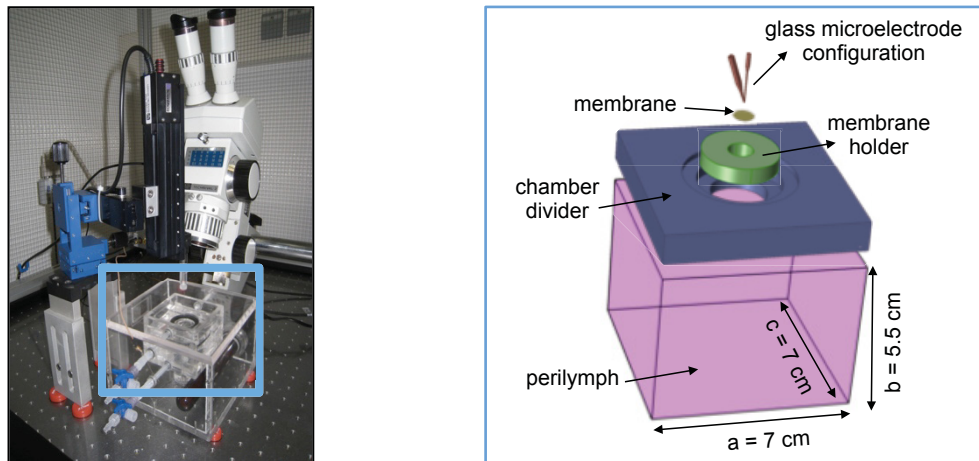
Figure 4.4: Components of the model (left). From top to bottom: the two-electrode system (red), the membrane (orange), the membrane holder (green), the chamber divider (blue), the chamber filled with perilymph (violet).

Since the model geometry is very complex and includes very tiny entities compared to the total volume, the process of mesh generation is rather challenging both for the number of mesh elements and computational memory. Therefore, a meshing sequence was used to keep high mesh resolution in the subdomains that hold very small details and that are important for analysis, while providing a coarser mesh in the other subdomains (Figure 4.5). Additionally, virtual mesh operations were applied to control the mesh between two subdomains.
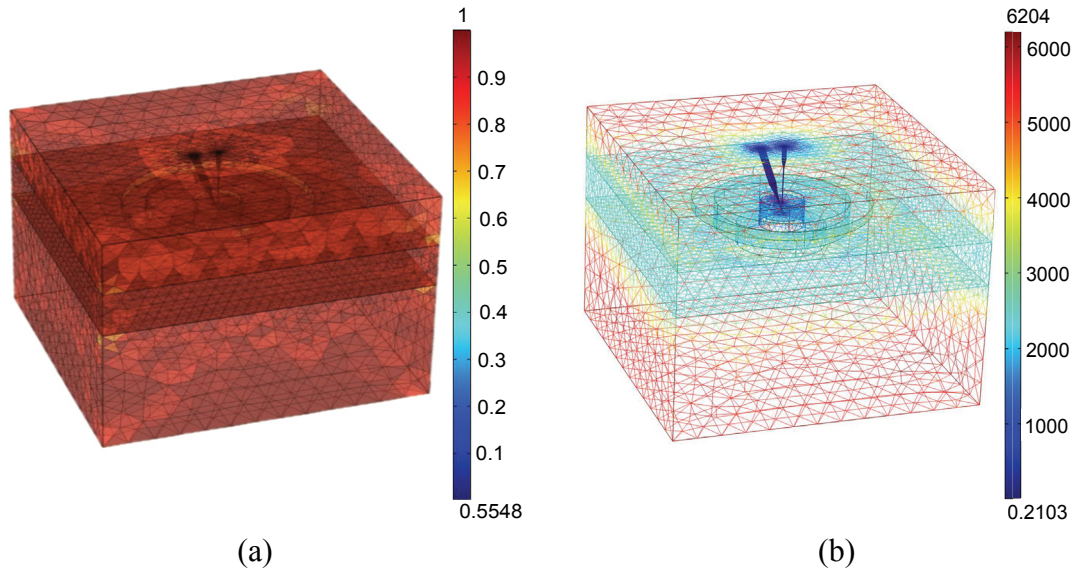
Figure 4.5: Plot of mesh element quality (scalar values between 0 and 1, where a higher number indicates a higher mesh element quality) (a) and mesh element size in μm (b) used for discretization of the model.

Eventually, the whole 3D geometry was discretized with 2,412,365 tetrahedral elements, including 177,616 triangular face elements, as well as 11,000 edge elements and 96 vertex element.

Additionally to the original *in vitro* model, two other model modifications were considered (Figure 4.6). In these models, the applied material properties in the subdomains remain unchanged as well as the dimensions of the glass pipettes and membrane. The difference to the original model is the number of electrodes used. To reduce the number of mesh elements and hence the computing effort, the whole bottom domain of the chamber directly under the disc-Ag/Ag/Cl-electrode (Ø 2 cm) was not included in the model and in the simulation, since no field distribution is expected there.

The modified *in vitro* model (Figure 4.6, (a)) was discretized with 2,365,024 tetrahedral elements, including 175,008 triangular face elements, as well as 10,890 edge elements and 92 vertex elements whereas the model in Figure 4.6, (b) was discretized with 1,229,986 tetrahedral elements, including 119,913 triangular face elements, as well as 3,672 edge elements and 104 vertex elements.

It is important to point out that every even tiny geometry modification in the models leads to a different mesh generation. Thus, the number of discretization elements alters. The models are useful to test and simulate the behaviour of the *in vitro* system by using different electrode configurations.
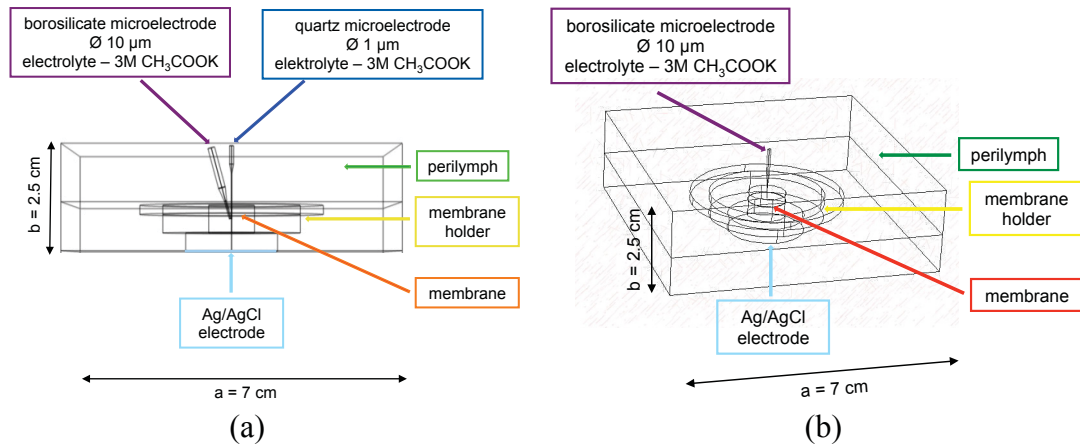
Figure 4.6: Modification of the *in vitro* model: (a) three-electrode configuration, (b) two-electrode configuration.

model	electrode configuration	subdomains	material properties	
			σ [S/m]	ε_r
initial	two-glass	electrode system	34.3	80
		membrane	0.0625	80
modified 1	two-glass + big disc	membrane holder	0	3
		chamber divider	0	3
modified 2	one-glass + big disc	chamber	2	109

Table 2: The subdomains and their material properties of the *in vitro* model and its modifications.

Eventually, simulations of the newly designed Ussing-like chamber (4 x 2 x 2 cm^3) with a membrane holder (opening ca. 0.8 mm, thickness ca. 5 mm) and two-Ag/AgCl-electrodes was completed to support the validity of the simulations carried out with the glass microelectrode configuration. The chamber and the membrane holder are made of plexiglass. The inclination angle of the membrane holder is 19°. The properties of the glass-electrodes and electrolytes remain the same as in the original *in vitro* model (Figure 4.7, (a)). For the second model, the wire-Ag/AgCl-electrodes are modelled as cylinders (Ø 0.1 cm and 2 cm high; $\varepsilon_r = 1$; $\sigma = 61.6 \cdot 10^6$ S/m).

The Ussing-like chamber with two-glass-electrode configuration (Figure 4.7, (a)) was discretized with 1,127,615 tetrahedral elements, including 63,333 triangular face elements, as well as 8,652 edge elements and 68 vertex elements. The model with the two-Ag/AgCl wire-electrodes in Figure 4.7 (b) was discretized with 399,216 tetrahedral elements, including 31,878 triangular face elements, as well as 2,027 edge elements and 52 vertex elements.
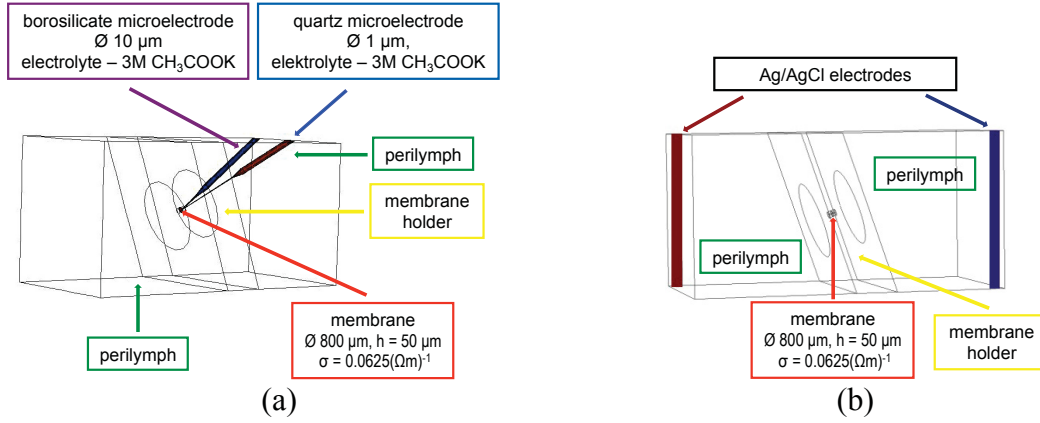
Figure 4.7: Model of the Ussing-like chamber: (a) with two-glass-electrode configuration, (b) with two-Ag/AgCl wire-electrodes.

model	electrode configuration	subdomains		material properties	
				σ [S/m]	ε_r
Ussing-like chamber 1	two-glass	electrode system	glass	34.3	80
			Ag/AgCl	$61.67 \cdot 10^6$	1
		membrane		0.0625	80
Ussing-like chamber 2	two-Ag/AgCl	membrane holder		0	3
		chamber		2	109

Table 3: The subdomains and their material properties of the Ussing-like chamber model

4.4 Lumped parameter model of the *in vitro* experimental setup

In addition to the proposed FEM models to simulate the impedance of the microelectrode–membrane–electrolyte interface, a second type of model of the *in vitro* experimental setup has been created and studied in MATLAB®/Simulink®. The lumped parameter model mimics the *in vitro* environment and allows exceptionally good analysis and comparison of simulated and measured impedance values.

Simulink® is a block diagram environment integrated within MATLAB®, enabling incorporation of MATLAB algorithms into models and exporting simulation results for further analysis.

Simulink provides a graphical user interface, includes custom built-in block libraries and uses solvers for simulating dynamic systems.

The lumped parameter model used to model the electical circuit of interest deploys components (blocks) of the Simscape™ library, for representing electrical components and circuits, called SimPowerSystem™. Initially, all blocks necessary to build the system were collected from the library. Afterwards, the selected blocks were connected according to a pattern needed to complete the circuit system. The parameters of these blocks can be easily changed when necessary and they can also be defined from the MATLAB workspace and used in Simulink. For simulation of any Simulink model built

of SimPowerSystem's blocks, an environment block (powergui) is needed. In this block simulation, configuration options and analysis tools can be specified. Finally, a simulation time was selected, a numerical method (discrete solver with a fixed step size) was chosen and a simulation was run. The fixed step size was chosen to compile with the sampling rate of the signals used in the measurements.

The model includes a source signal (current chirp or rectangular signal), branch of RC elements in parallel and a voltage measurement block that measures voltage between two electrical nodes. Moreover, an impedance measurement block that measures impedance as a function of frequency has been attached between two nodes (Figure 4.8).
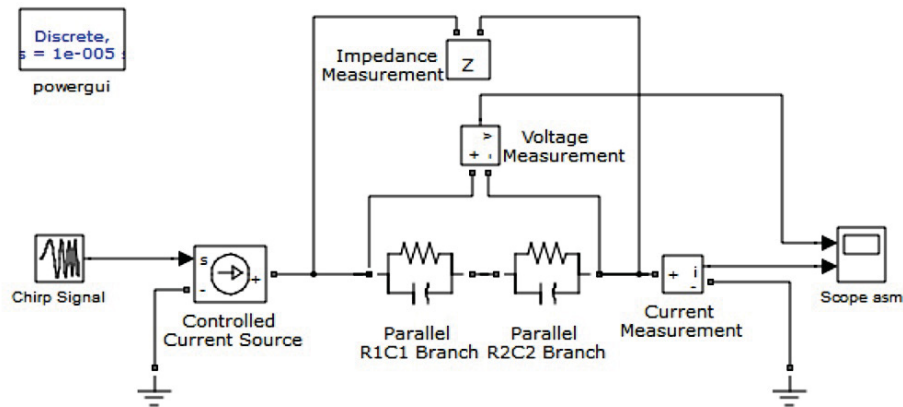
Figure 4.8: A lumped parameter model of the *in vitro* experimental setup in MATLAB®/Simulink®.

The lumped parameter model can be used not only to validate the COMSOL-model but also to analyse the imported measurement data, the injected current and the measured voltage. Ultimately, comparisons between experimental results and their theoretical predictions can be carried out (Figure 4.9).

Furthermore, the lumped parameter model could also be very useful in the process of calibration, verification and validation of the instruments. Therefore, the model was appropriately adapted and built to model the SEC passive cell model (see 3.3.2.1) used to tune and test the measuring instruments. The exact circuit combinations of passive elements (resistors and capacitors) and their parameter values respectively were then included and assigned. In this case, the source signal is imported from the measured data file including the input (current) signal used for the measurements. A comparison of the voltage output - measured and simulated signal can be made. The computed impedance values using the Fourier transformation ($\mathbf{Z}(\omega) = \mathbf{F}\{v(t)\}/\mathbf{F}\{i(t)\}$) of the measured signals in time domain, can then be compared with the simulated impedance values.

Additionally, a special Simulink model was built in such a way that by using the measured input and output in time domain, estimation values of the R and C passive elements can be directly identified. For this, the Control and Estimation Tools Manager was used. The estimated parameters were then compared with the parameters identified upon the impedance values using the MATLAB implementation of the Nelder-Mead

(simplex) method for finding the minimum of a scalar function of several variables in order to verify the self-written code in MATLAB® for parameter identification.
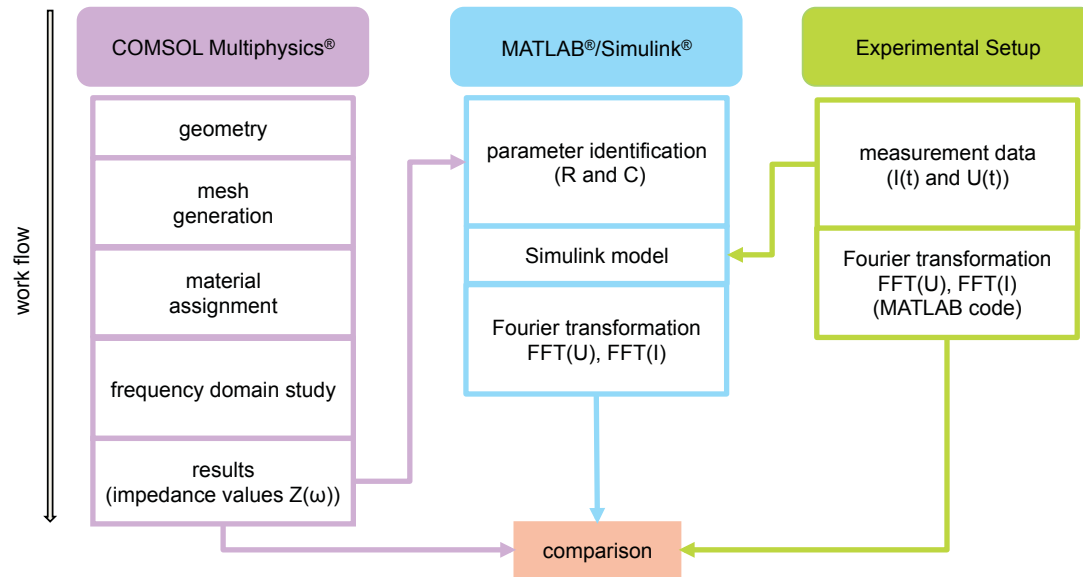
Figure 4.9: A work-flow diagram for measurement, simulation and characterization of the electrode-membrane-electrolyte system.

5 Simulation and measurement results

5.1 Numerically computed results

5.1.1 A single fluid-filled glass microelectrode

Historically, for analysing the electrical properties of a microelectrode tip, a parallel RC equivalent circuit has been considered [85],[92]. It has been assumed that R_e is the resistance concentrated at the tip of the microelectrode, whereas C_e is the capacitance distributed along the microelectrode [86]-[92] (Figure 5.1). Hence, a COMSOL-model of a single fluid-filled glass microelectrode immersed in a aqueous solution (saline cylinder) was designed to provide a better understanding of the electrical properties of such a microelectrode [89].
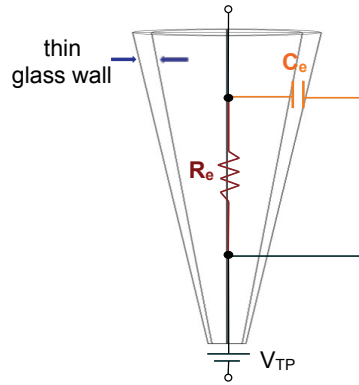
Figure 5.1: Equivalent circuit of a glass microelectrode tip.
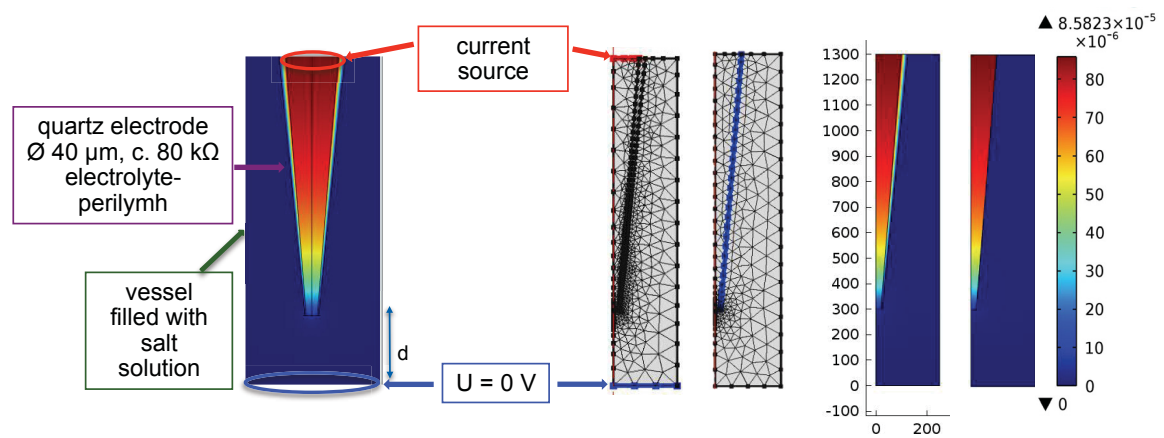
Figure 5.2: Plot of electric potential (V) (left 3D model; right 2D axisymmetric model with thin glass wall and thin contact impedance layer approximation, respectively).

To verify the existence of a parallel RC equivalent network, a test glass electrode (tip data: Ø 40 μm, α = 0.1 rad, thickness of the glass linearly increasing 5-25 μm) filled with electrolyte (ε_r = 109; σ = 2 S/m) and immersed in a cylindrical chamber (Ø 250 μm, height h = 1000 μm) was subjected to a sine wave analysis (I_0 = 1 pA; f = 0 Hz - 1 GHz). Furthermore, Nyquist plots of the impedance were generated and used to verify the presence of an equivalent parallel RC circuit (Figure 5.4). Eventually, the values of the R and C lumped elements were identified (Figure 5.4) using the MATLAB implementation of the Nelder - Mead (simplex) method for finding the minimum of a scalar function of several variables. Additionally, the least square method was used as a quality criterion for the optimisation process. The Nyquist plots of impedance values computed in COMSOL Multiphysics® indicated the existence of two equivalent parallel RC elements in series. Moreover, it was presumed that one parallel RC circuit represents the glass microelectrode tip, while the second one exists between the microelectrode and the bath electrode. The parameter identification has shown that the adopted RC circuit was valid for a broad frequency range. However, in the high frequency range > 10 MHz, further parasitic lumped elements appear which contribute to a slight deviation between the computed and identified values.
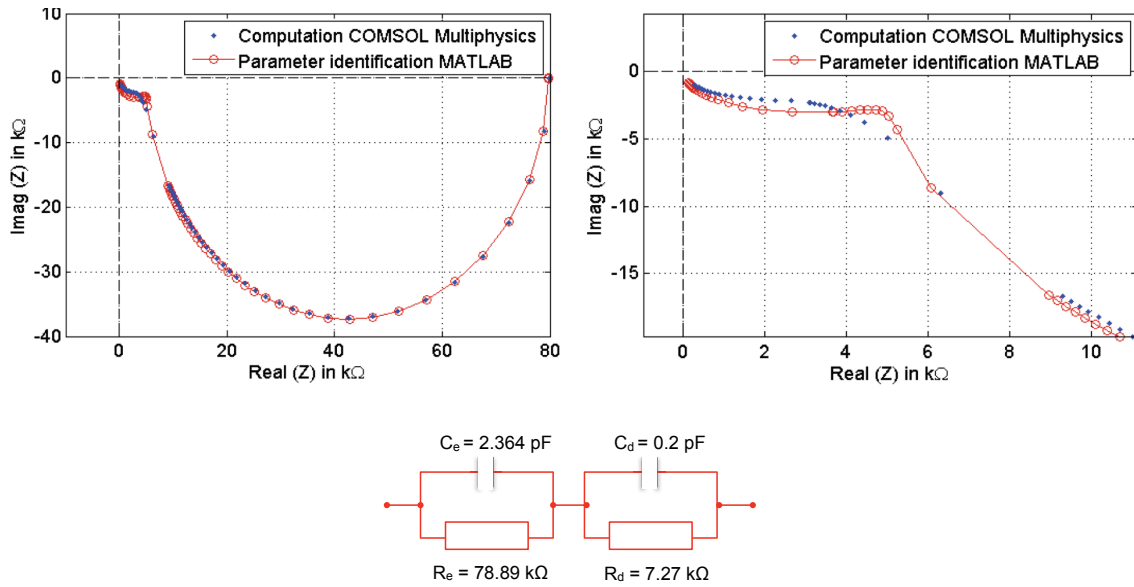
Figure 5.4: Nyquist plot of impedance values (equivalent reactance against equivalent resistance) computed in COMSOL Multiphysics® (up); identified parameter values of two parallel RC circuits in series (down).

In order to investigate the presumption given above, the distance between the electrode tip and the bath electrode (ground) was gradually increased from 0 mm (tip laying directly on the bath electrode) to 3 mm and a frequency study was performed. The electrode remained the same size and was submerged to the same depth inside the cylindrical chamber filled with saline. The height of the cylindrical chamber was increased and hence the distance between the ground and the electrode tip is altered.

Figure 5.3: Equivalent resistance (left) and equivalent reactance (right) as a function of frequency (logarithmic scaling).

Hence, the simulation results were presented in two different forms. Figure 5.3 shows the equivalent resistance and equivalent reactance as a function of frequency.

Clearly, the magnitude of the equivalent resistance decreases with increasing the distance between the electrode tip and the bath electrode and two different relaxation times (time constants $\tau = \varepsilon/\sigma = RC = 1/(2\pi f_c)$) are to be seen. The first time constant is at $f = 800$ kHz whereas the second is at $f = 300$ MHz (Maxwell-Wagner effect). Moreover, a parameter identification was performed and the obtained results are illustrated in Figure 5.4. Evidently, the RC values of the first parallel circuit remain almost the same with increasing the distance between the electrode tip and the bath electrode but there is a substantial difference between the values of the second RC circuit – the values increase with increasing of the distance.
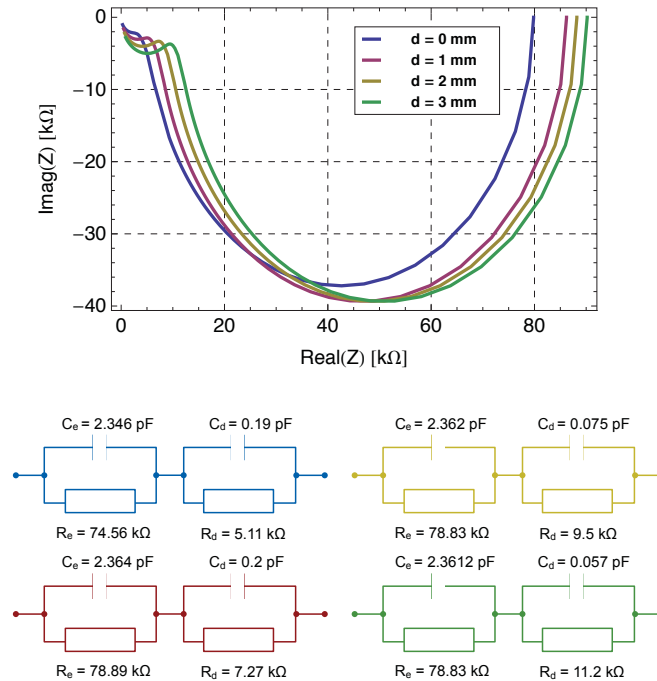
Figure 5.4: Nyquist plot of impedance values computed in COMSOL Multiphysics[®] (up); identified values of two parallel RC elements in series (down).

Moreover, test simulations were made on glass microelectrodes with different geometries, filled and surrounded with different solutions. Additionally, the electrodes were submerged at varying depths of immersion (1-5 mm) in a bulk solution to observe the effect on resistance and capacitance. In the models, the influence of physicochemical phenomena was not investigated - no double layers are included and no diffusion processes are considered.

5.1.1.1 The glass microelectrode capacitance

The capacitance of a glass microelectrode, discussed in details in [85], [87], [90], has been found to depend upon the depth of immersion. In fact, the latter should be carefully taken into account in bioimpedance measurements since the experiments are performed by immersing the electrodes at different depths in bulk solutions and in the biological tissues. Thus, in order to observe the effect on the electrode capacitance that arises due to varying immersion depth, subsequently, a glass microelectrode tip (Ø 5 µm, $\alpha = 0.1$, linearly increasing glass thickness - $r_2/r_1 = 1.33$) was immersed millimetre by millimetre in salt solution. Moreover, in each case, a frequency study was performed to investigate possible changes of the electrode-electrolyte impedance as a function of the immersion depth.
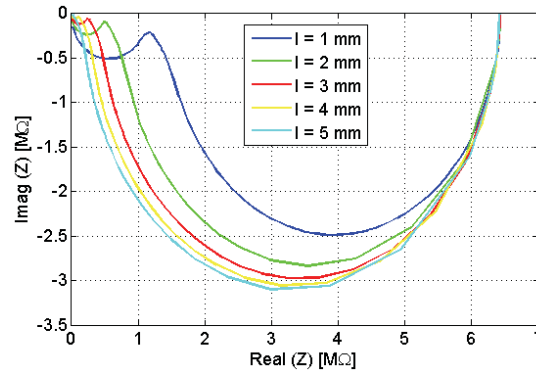
Figure 5.5: Nyquist plot of impedance values for mm immersion of the microelectrode tip in the salt solution, computed in COMSOL Multiphysics®; l is the immersion depth ranging from 1 to 5 mm.
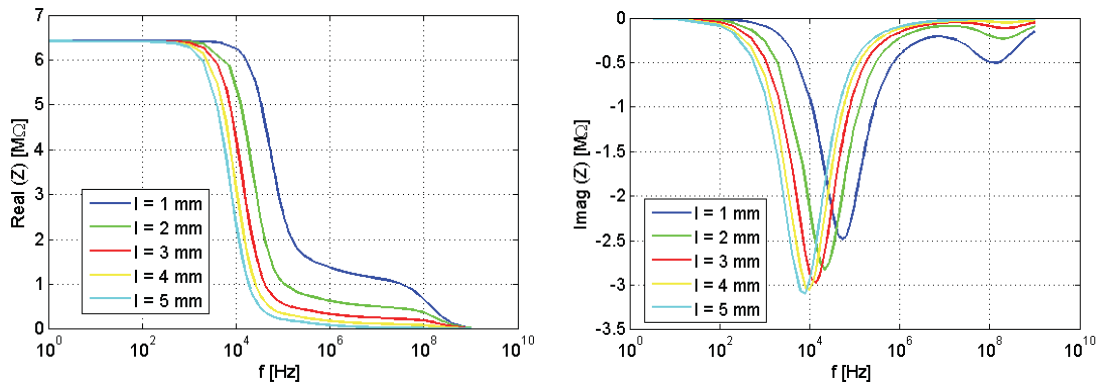
Figure 5.6: Equivalent resistance (left) and equivalent reactance (right) as a function of the frequency (logarithmic scaling); l is the immersion depth ranging from 1 to 5 mm.

It can be seen from Figure 5.5 and Figure 5.6 that with increasing of the immersion depth, the time constant increases as well (f_c decrease).
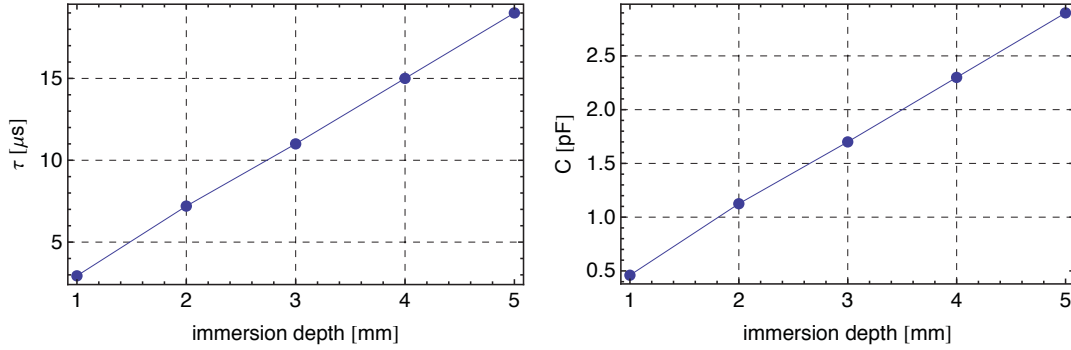
Figure 5.7: Time constant (τ) as a function of immersion depth of the microelectrode tip (left); microelectrode capacitance as a function of the immersion depth of the microelectrode tip (right).

Furthermore, from the obtained simulation data, the capacitance value can be identified. Figure 5.7 shows the capacitance of a microelectrode as a function of the immersion depth. As the electrode is submerged deeper in the solution, a linear relationship between the capacitance and the depth of immersion is found. The changes of the capacitance are approximately 0.6 pF/mm which is compatible with the results (between 0.4 and 1 pF/mm) reported by [87], [92], [93], whereas it is obvious from Figure 5.5 and Figure 5.6 (left) that the resistance doesn't change considerably.

Next, simulations were performed by varying the thickness of the glass. For this purpose, an electrode with tip opening of Ø 5 μm, $\alpha = 0.025$ and three different uniform glass thicknesses was accounted ($d_t = 0.825$ μm, $d_t = 8.25$ μm and $d_t = 4.537$ μm (mean value of 0.825 and 8.25)) and a linearly increasing glass thickness - $r_2/r_1 = 1.33$ (from 0.825 μm at the apex to 8.25 μm at the base). The ratio $r_2/r_1 = 1.33$ is roughly the same as the ratio of the inner and outer radius of the quartz glass capillary (fire polished QF 120-90-10) used for the experiments.
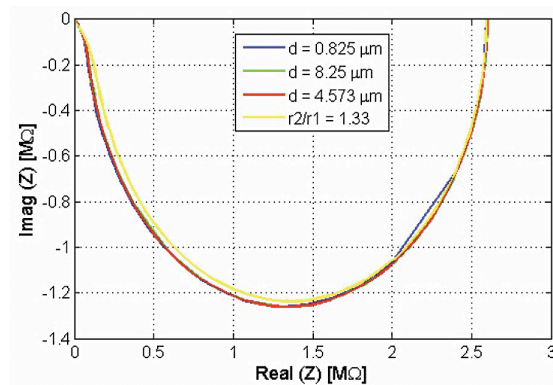
Figure 5.8: Nyquist plot of impedance values for different glass thicknesses computed in COMSOL Multiphysics®; d_t is the uniform glass thickness.
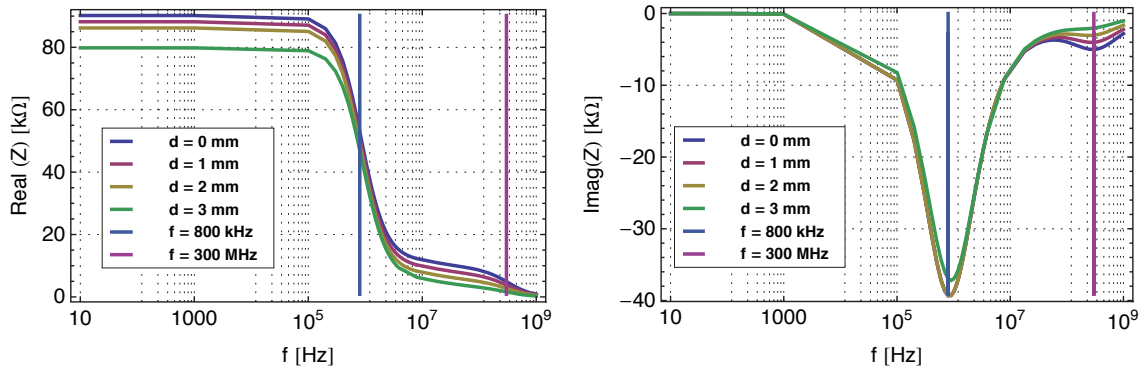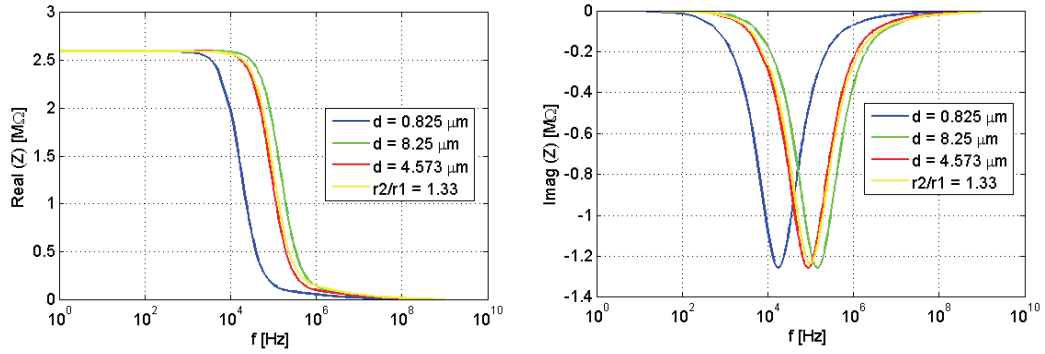
Figure 5.9: Equivalent resistance (left) and equivalent reactance (right) as a function of frequency (logarithmic scaling); d_t is the thickness of the uniform glass layer, r_2/r_1 is the ratio of the linearly increasing glass thickness.

The obtained results are illustrated in Figure 5.8 and Figure 5.9 and they show that with increasing the uniform glass thickness, the impedance values remain approximately the same and the time constant decreases (f_c increases). Thereby, the capacitance decreases with increasing the glass thickness. Interestingly, the impedance value obtained by modeling a uniform glass thickness with $d_t = 4.537$ μm is very close to that when a linearly increasing glass thickness is considered. Therefore, for simplification of the model, in the majority of cases, the thickness of the glass is approximated as a uniform thin layer, by using special boundary condition (contact impedance), specified by the material conductivity, permittivity and thickness d_l (see Section 4.3.1).

5.1.1.2   The glass microelectrode resistance

To date, several theoretical and experimental studies have been performed regarding the glass microelectrode resistance [85], [86], [88]. Therein, it was stated that the resistance of a glass microelectrode is inversely proportional to the diameter of the tip opening and the electrode length does not much affect the resistance. Hence, the resistance is mostly concentrated at its tip. Furthermore it was revealed that the resistance strongly depends on the concentration of the filling solution as well as on the concentration of the surrounding solution in which the electrode is immersed. Another presumption is that the resistance of the microelectrode is approximately a linear function of the resistivity of the surrounding solution [84], [85]. Further study showed, that the total electrode resistance is determined not only by the electrode geometry and the filling and bathing solution (internal resistance), but also by the resistance between the electrode tip and the ground electrode in the surrounding medium (external resistance). Moreover, the external resistance in a glass microelectrode is usually way smaller than the internal resistance [91].

All previously mentioned issues were considered in the *in silico* study of a single fluid-filled glass microelectrode. Resistances of test glass microelectrodes, with different tip openings and lengths, immersed in seven solutions of different resistivities ρ_o (3.3, 10, 100, 300, 500, 700 and 900 Ωcm) were computed. Each microelectrode was filled with $\rho_i = 3.3$ Ωcm. The outcome of the simulations confirms the expected effects described in the literature.

Assuming a glass microelectrode with a perfect insulating wall, the equation used for the approximate calculation of the internal and external electrode resistance derived from a general model of an open tip glass microelectrode with radius r_0 and angle α (in radians) in [86], [88], [91] is:

$$R_i + R_o = \frac{\rho_i}{\pi r_0 \alpha} + \frac{\rho_o}{2\pi r_0} \qquad (5.1)$$

Further, a comparison of the numerically and analytically computed total electrode resistance (internal and external) values was done considering no double layer and no diffusion (Figure 5.10). A pipette with a tip diameter of 0.5 μm, a cone angle $\alpha = 0.0025$ rad filled with 3M KCl electrolyte ($\rho_i = 3.3$ Ωcm) was immersed into a chamber filled with seven different electrolytes with resistivities ranging from 3.3 to 900 Ωcm. The maximal relative difference between the analytical and numerical results was 0.9%.
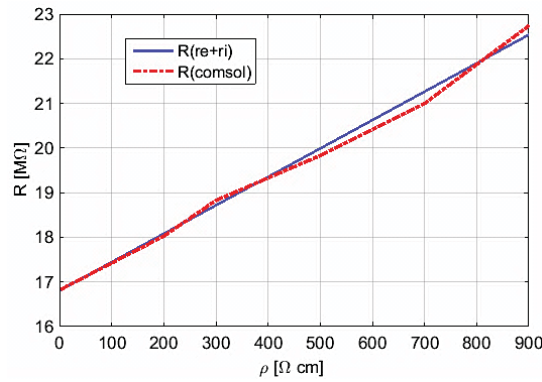
Figure 5.10: Resistance of a microelectrode with tip diameter 0.5 μm, cone angle $\alpha = 0.0025$ rad filled with 3M KCl solution ($\rho_i = 3.3$ Ωcm) as a function of resistivity of test solutions (KCl) ranging from 3.3 to 900 Ωcm. Numerically computed values in COMSOL Multiphysics® (red line) and analytical resistance values (blue line) are shown.

Further, in this study, two other electrode tip geometries were modeled (Ø 0.1 μm, $\alpha = 0.005$ rad and Ø 5 μm, $\alpha = 0.025$ rad) and filled with 3M KCl ($\rho_i = 3.3$ Ωcm) as well as with 0.1 M KCl solution ($\rho_i = 100$ Ωcm) and immersed in seven different solutions starting from 3M KCl ($\rho_i = 3.3$ Ωcm) to 0.01M KCl ($\rho_i = 900$ Ωcm) as proposed in [88].

Interestingly, Figure 5.11 and Figure 5.12 show similar resistance-resistivity dependence although different filling solutions and different tip geometries were considered. It can be also deduced that with increasing resistivity of the filling solution, the resistance increased.

Similarly to [90], Figure 5.13 illustrates the linear relation between the high resistance microelectrode (Ø 0.1 μm) to the low resistance microelectrode (Ø 5 μm) under identical filling solutions.
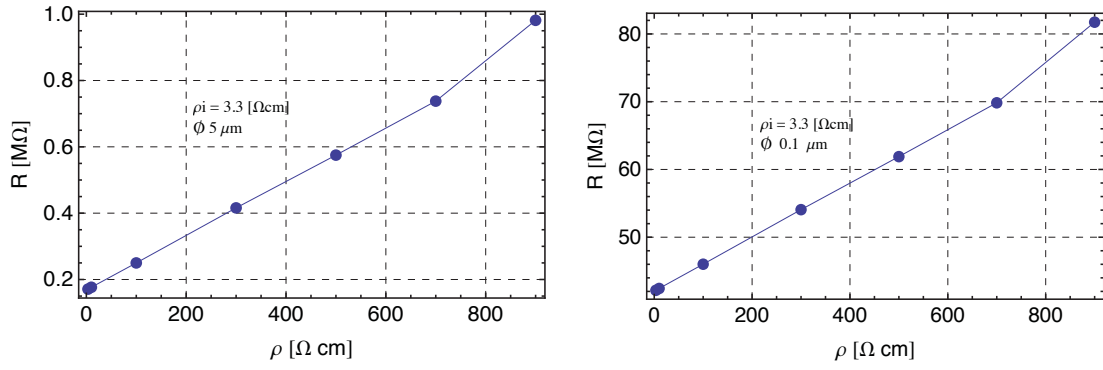
Figure 5.11: Resistance as a function of resistivity of test solutions (KCl) ranging from 3.3 to 900 Ωcm for microelectrodes filled with 3M KCl solution (ρ_i = 3.3 Ωcm); low resistance microelectrode - tip diameter 5 μm (left), high resistance microelectrode - tip diameter 0.1 μm (right).
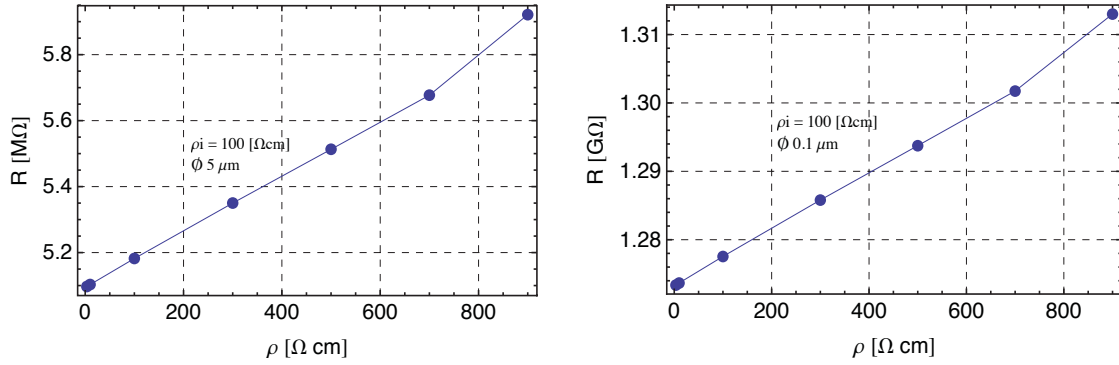
Figure 5.12: Resistance as a function of resistivity of test solutions (KCl) ranging from 3.3 to 900 Ωcm for microelectrodes filled with ρ_i = 100 Ωcm (0.1 M KCl) solution; low resistance microelectrode - tip diameter Ø 5 μm (left), high resistance microelectrode - tip diameter Ø 0.1 μm (right).
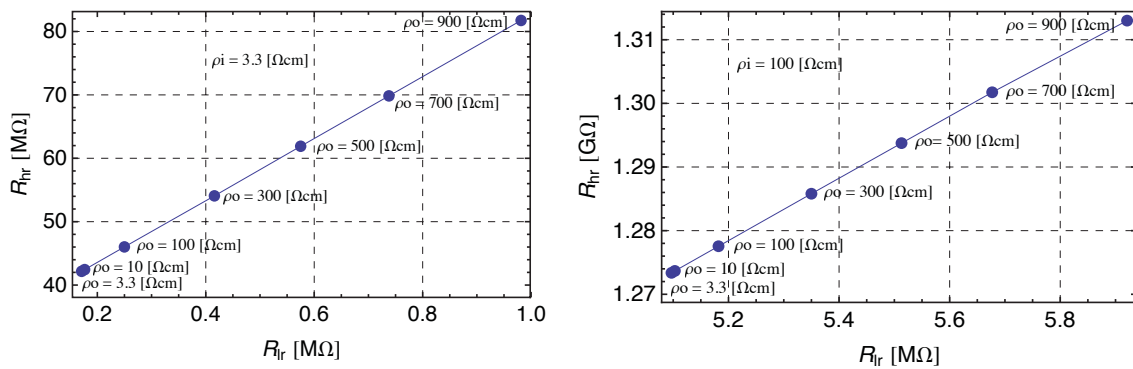
Figure 5.13: Relation between resistance of high resistance microelectrodes and low resistance microelectrodes when filled either with KCl solutions with ρ_i = 3.3 Ωcm (left) or ρ_i = 100 Ωcm (right) and immersed into solutions with resistivity ranging from 3.3 to 900 Ωcm.

Additionally, a frequency domain study was made, where the resistivity of the filling solution was set to $\rho_i = 3.3$ Ωcm whereas the resistivity of the surrounding solution was $\rho_o = 3.3$ Ωcm, $\rho_o = 100$ Ωcm and $\rho_o = 1000$ Ωcm.

By varying the resistivity of the surrounding solution it is obvious that the impedance and the time constant change and decrease with decreasing resistivity of the surrounding solution (Figure 5.14, Figure 5.15).
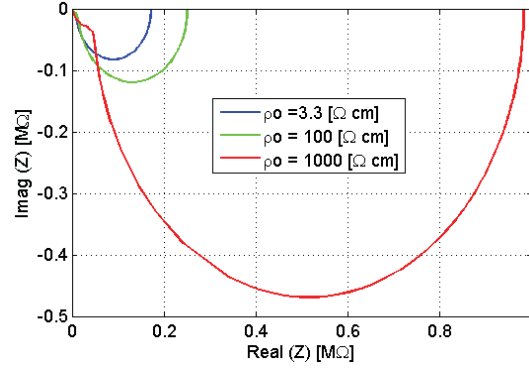
Figure 5.14: Nyquist plot of impedance values computed for resistivity of filling solution $\rho_i = 3.3$ Ωcm and resistivity of surrounding solution $\rho_o = 3.3$ Ωcm, $\rho_o = 100$ Ωcm and $\rho_o = 1000$ Ωcm with tip diameter Ø 5 µm.
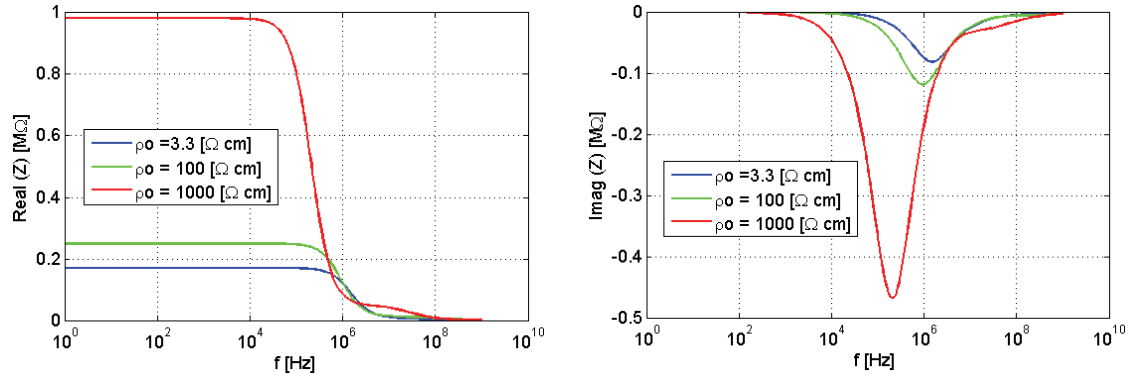
Figure 5.15: Equivalent resistance (left) and equivalent reactance (right) as a function of frequency (logarithmic scaling); the resistivity of filling solution is $\rho_i = 3.3$ Ωcm and the resistivity of surrounding solution is $\rho_o = 3.3$ Ωcm, $\rho_o = 100$ Ωcm and $\rho_o = 1000$ Ωcm with tip diameter Ø 5 µm.

To summarize, the same glass micropipette may have a wide range of resistances as a microelectrode, depending on the filling and immersing solution.

5.1.2 Two-electrode system

A model of a two-electrode system with the same tip geometries as the electrode configuration used for the *in vitro* model simulations (tip data: Ø 1 µm, $\alpha = 0.005$ rad, thickness of the glass linearly increasing - $r_2/r_1 = 1.33$; tip data: Ø 10 µm, $\alpha = 0.0225$

rad, thickness of the glass linearly increasing - $r_2/r_1 = 1.25$) immersed in a salt solution ($\varepsilon_r = 109$; $\sigma = 2$ S/m) was also considered (Figure 5.16). Both pipettes are filled with the same electrolyte as the surrounding one.
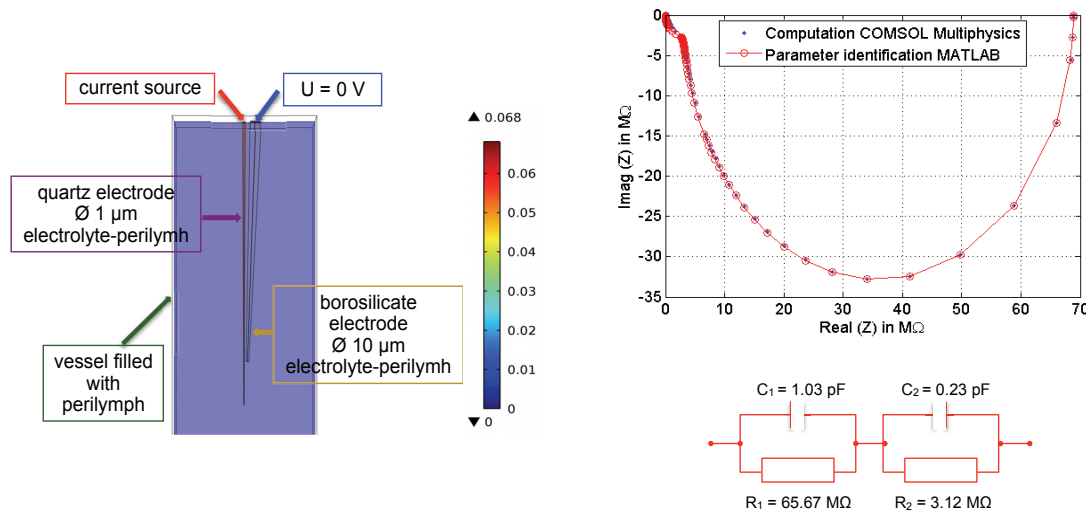
Figure 5.16: Electric potential (left); Nyquist plot of equivalent reactance against equivalent resistance computed in COMSOL Multiphysics® and MATLAB®/Simulink®; identified values of two parallel RC elements in series (right).

After a frequency domain study was performed, the simulation results were identified. Next, the identified values were assigned to the lumped parameter model in MATLAB®/Simulink® and a test analysis was performed. Hence, a chirp signal (see section 5.2 for more information) was generated and injected in the RC circuit. The output of the model simulations comprised the voltage response and additionally computed impedance values. Figure 5.17 shows the impedance as computed values in COMSOL Multiphysics®, the impedance values as computed with the powergui in MATLAB®/Simulink® and the Fourier transform values from the time domain simulations in MATLAB®/Simulink®.
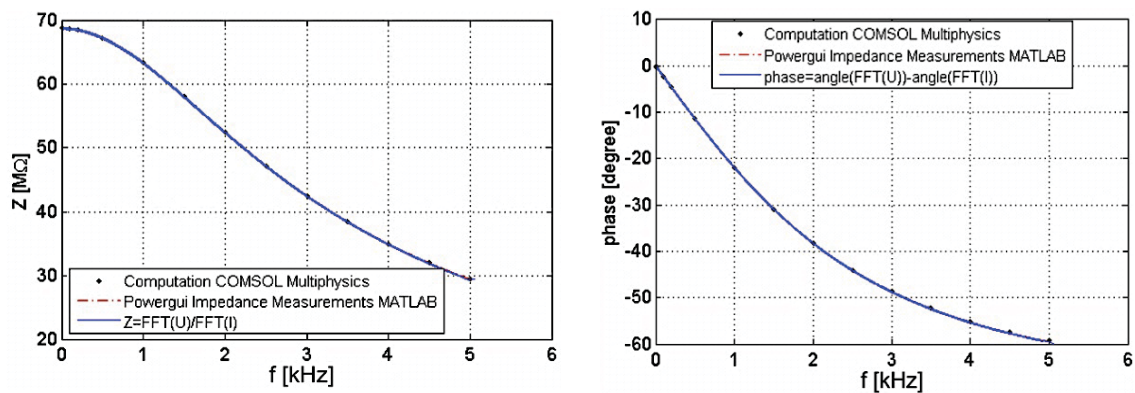
Figure 5.17: Plot of impedance and phase against frequency. Computed values in COMSOL Multiphysics® and MATLAB®/Simulink® are shown.

The comparison of the computed impedance profile over a frequency range f = 10 Hz - 5 kHz yields a maximum relative difference under 0.1%.

Further, the pipettes were filled with a different electrolyte (ε_r = 80; σ = 34,3 S/m) and immersed in the same bath solution (ε_r = 109; σ = 2 S/m). The same analysis was proceeded as before and this test simulation yields the electrical properties of the two-electrode configuration used in the *in silico* study of the experimental setup.
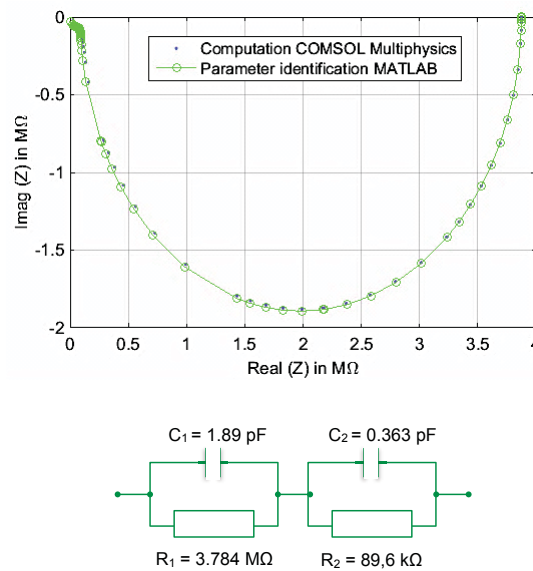
Figure 5.18: Nyquist plot of equivalent reactance against equivalent resistance computed in COMSOL Multiphysics® and MATLAB®/Simulink®; identified values of two parallel RC elements in series (right).

The two test examples show again that the total resistance value of the electrode system strongly depends on the chosen resistivity of the filling electrolyte. Thus, normally, for lowering of the electrode resistance, which is desirable in the experiments, a highly concentrated electrolyte (usually 3M KCl or as in this study 3M CH_3COOK) is used.

5.1.3 *In silico* study of the experimental setup

Eventually, an *in silico* study of the experimental setup including a membrane was carried out. Initially, two glass microelectrodes as described in 4.3.2 were immersed (1.2 cm deep) in a bathing solution (*in vitro* chamber with inserted membrane holder) and subjected to a sine wave analysis (I_0 = 500 pA, f = 0 Hz - 1 MHz). In order to obtain current flow, one electrode is the current carrying (voltage recording) and the other one is the indifferent electrode. The output of the model simulations comprised the voltage response and additionally computed impedance values. Afterwards, the same analysis was made by inserting a membrane in the membrane holder between the tips of the electrodes. It was considered that the current-carrying electrode is centrally inserted through the membrane und positioned ca. 50 μm under the membrane. Hence, the indifferent electrode is positioned ca. 50 μm above the membrane. Next, both simulation data were plotted in a Nyquist diagram (Figure 5.19) and a parameter

identification was made in order to obtain the difference in impedance (resistance and capacitance) values between the two simulation cases.

With membrane insertion between the tips of the glass microelectrodes, the impedance increased and as shown in Figure 5.19, after identifying the RC circuits fitting the computed values, only a small change in the resistance of the system can be seen. The increase of the resistance in the *in vitro* system occurs as a consequence of assigning a purely homogeneous resistant membrane. The impedance due to the membrane sample is the difference between the impedance with and without membrane insertion.
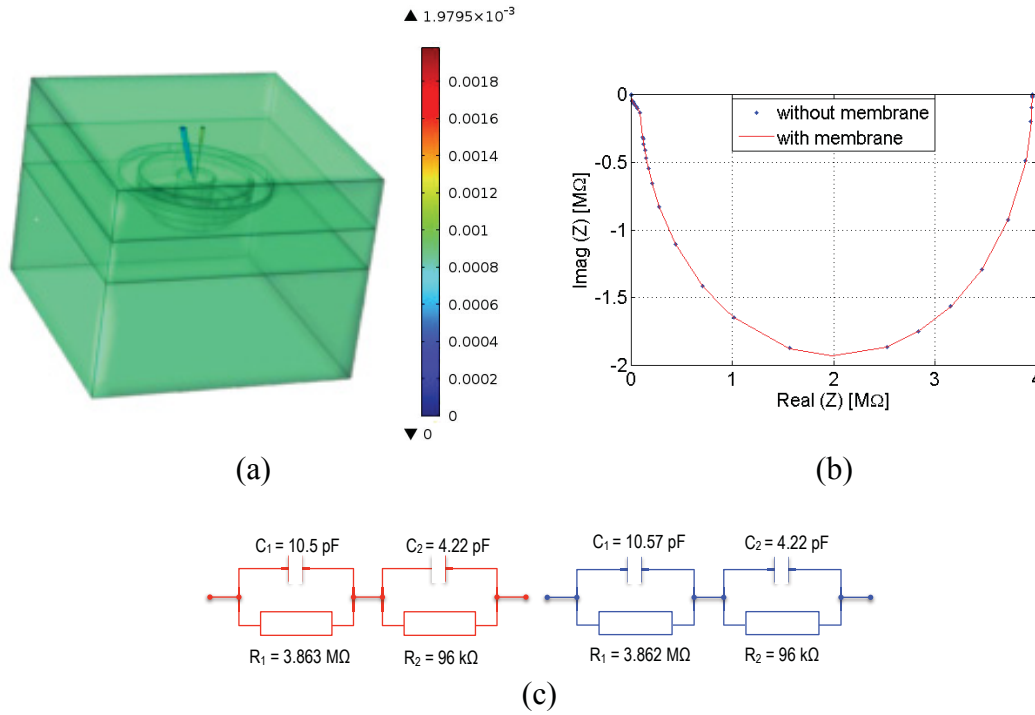
Figure 5.19: Electric potential (a); Nyquist plot of equivalent reactance against equivalent resistance (b); identified values of two parallel RC elements in series for the case without (red colour) and with membrane insertion (blue colour) (c).

5.1.3.1   Modificated *in vitro* models

To further investigate the properties of the *in vitro* system and simulate its behaviour, some alterations were made and different electrode configurations were taken into account (see Figure 4.6). Generally, to better control and distinguish the measured tissue zone during bioimpedance measurements, it is preferable to use a third electrode or even a fourth electrode [30]. Therefore, in the first modified model, a third neutral big disc-Ag/AgCl-electrode was included. The borosilicate electrode was taken as current-passing whereas the quartz electrode was taken as a signal-recording electrode (with no or negligible current flow). In this case the obtained result is a transfer impedance which is defined with excitation and response at different terminals (electrodes). The computed transfer impedance values (Figure 5.20 and Figure 5.21) indicate another equivalent circuit than the one proposed and used for fitting a terminal impedance (the current-carrying electrode is also used for measuring the potential drop). The parameter

identification has shown that an adopted parallel RC circuit in series with additional resistor was valid for a broad frequency range. However, in the high frequency range >100 kHz, further parasitic lumped elements appear which contribute to a deviation between the computed and identified values. Thus, the properties of the proposed three-electrode configuration have to be further investigated. Moreover, to get even more precisely impedance values of the membrane sample, the potential difference between a terminal and a transfer impedance can be considered. Technically, it should be possible to conduct the *in vitro* experiments in such manner to get this potential difference.

Figure 5.20: Nyquist plot of impedance values computed when using the three-electrode configuration.

Figure 5.21: Equivalent resistance (left) and equivalent reactance (right) as a function of frequency (logarithmic scaling) when using the three-electrode configuration.

In the second modified model, a two-electrode configuration with a borosilicate electrode (both current-passing and voltage recording, placed 150 μm above the membrane) against a big indifferent disc-Ag/AgCl-electrode (placed under the membrane) was considered. Once again, numerical simulations without and with membrane between the current-carrying and the indifferent electrode were performed. The output of the model simulations comprised the voltage response and additionally computed impedance values which were then fitted to an appropriate equivalent RC circuit - two parallel RC circuits in series.

To reduce the number of mesh elements and hence the computing effort, the whole bottom domain of the chamber directly under the disc-Ag/AgCl-electrode was not included in the models and in the simulation, since no field distribution is expected there. As presumed, this model modification did not influence the numerical results.

The identified parameter values from the simulation results, taking into account the two additional electrode configurations, are summarized in Table 4. The symbol "x" in the table stands for "no capacitance value" due to the fitting of a resistor in series to a parallel RC circuit for the computed impedance spectrum of modified model 1.

model	electrode configuration	membrane insertion	identified values			
			R_1 [Ω]	C_1 [pF]	R_2 [Ω]	C_2 [pF]
modified 1	two-glass + big disc	no	34.87	x	46.90	$7 \cdot 10^4$
		yes	43.7	x	58.36	$6 \cdot 10^4$
modified 2	one-glass + big disc	no	90210	4.255	431.9	2.2
		yes	90304	4.255	441.8	2.2

Table 4: Identified parameter values obtained from the computed impedance in COMSOL Multiphysics® considering two different electrode configurations.

Since the shape of the stimulated tissue volume strongly depends not only on the active electrode dimensions but also on the relative position of the electrodes to each other, numerical simulations changing the position of the current carrying electrode to the membrane i.e. to the indifferent electrode were done. Therefore, the active electrode tip was positioned 200 μm above the membrane and moved towards the membrane with a 50 μm step until the tip was directly positioned on the membrane surface. Altogether five different impedance values were computed and the identified RC values fitted to a two parallel RC circuits in series are given in Table 5.

model	electrode position [μm]	identified values			
		R_1 [kΩ]	C_1 [pF]	R_2 [kΩ]	C_2 [pF]
modified 2 one-glass + big disc	0	114.36	4.317	0.446	2.245
	50	90.89	4.281	0.441	2.196
	100	90.55	4.271	0.442	2.198
	150	90.30	4.256	0.442	2.201
	200	90.29	4.240	0.442	2.203

Table 5: Identified parameter values obtained from the computed impedance in COMSOL Multiphysics® for different positions of the active electrode in respect with the indifferent electrode.

As it can be seen from the values tabulated in Table 5, the resistance and capacitance values of the first RC circuit gradually decrease with increasing the distance between the electrodes, in the stimulating area 50-200 μm above the membrane. However, when the active electrode starts to closely approach the membrane sample, the impedance values increase rapidly. The values of the second circuit remain almost unchanged.

5.1.3.2 The Ussing-like model

A model of a newly designed Ussing-like chamber was also built and numerical simulations with two different electrode configurations were carried out. The idea behind this model was to test the reliability and the validity of the initial glass-microelectrode configuration by using two-Ag/AgCl-wire electrodes. Hence, numerical simulations without and with membrane between the current-carrying and the indifferent electrode were performed.

First, simulations with the two-glass electrode configuration were made. In Figure 5.19 and in Figure 5.22, as it was to be expected, can be clearly seen that the computed impedance values show the same frequency-depended characteristic. The identified values confirm this also (see Figure 5.19, (c) and Table 6).
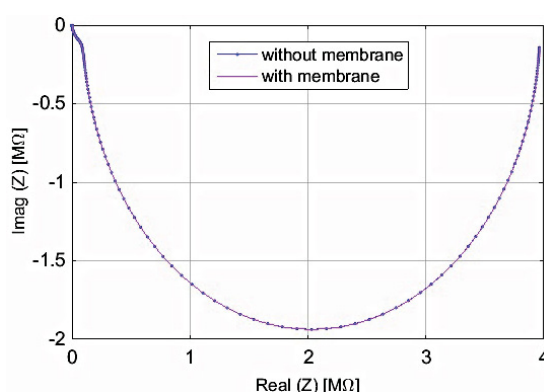
Figure 5.22: Nyquist plot of impedance values computed when using the initial glass-microelectrode configuration.
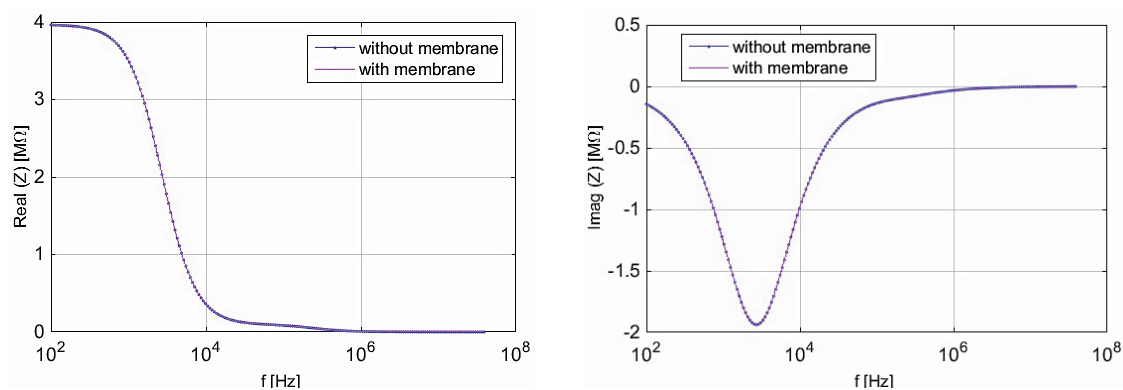
Figure 5.23: Equivalent resistance (left) and equivalent reactance (right) as a function of frequency (logarithmic scaling) when using the initial glass-microelectrode configuration.

In Figure 5.22 and Figure 5.23, no significant difference can be seen between both curves because the impedance of the electrode configuration (MΩ) is several orders of magnitude bigger than the one of the membrane sample (few Ω). Thus, this is the major drawback when measuring with glass electrode configurations. It is very challenging to catch the electrical signals coming only from the measured biological sample when the

properties of the glass electrode are not properly compensated before (see Section 5.2.1).

Furthermore, another low impedance measurement configuration consisting of Ag/AgCl wires was used just to show the difference in the impedance spectrum between the two studies. One undesirable effect appearing during measuring with such electrodes is the polarisation impedance of the electrodes but this will not be treated here. The results are shown in Figure 5.24 and Figure 5.25.
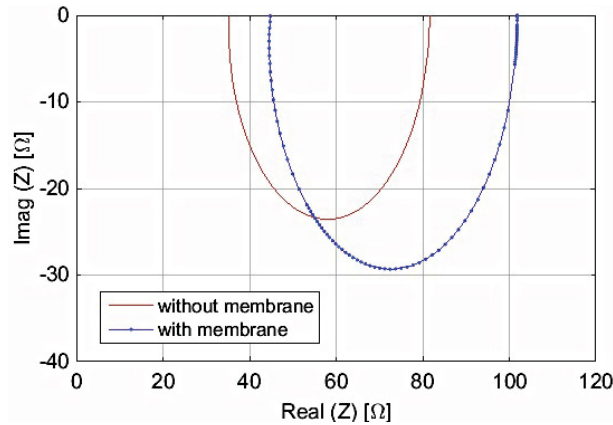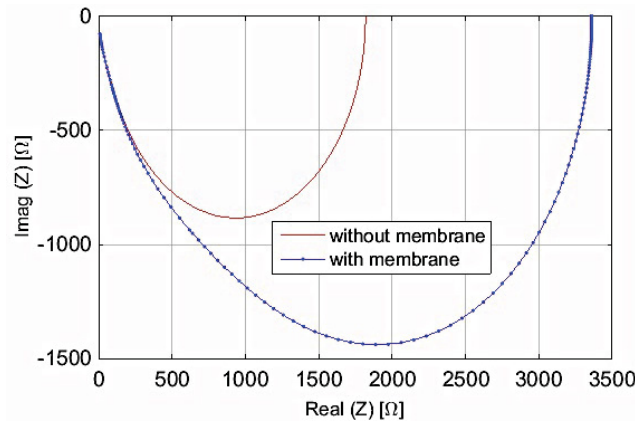

Figure 5.24: Nyquist plot of impedance values computed when using the two-Ag/AgCl-electrode configuration.

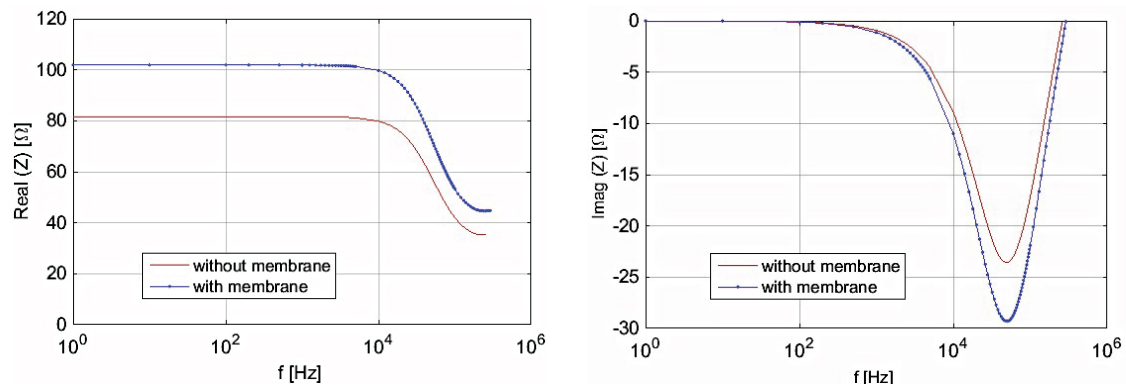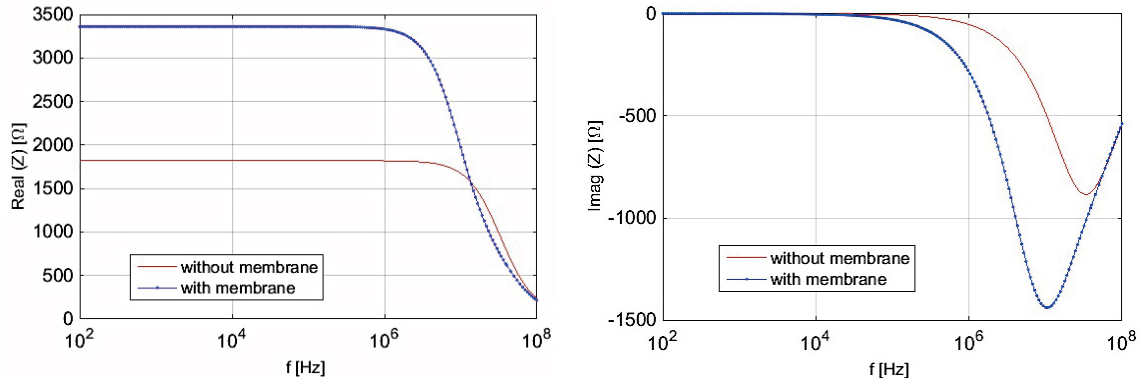Figure 5.25: Equivalent resistance (left) and equivalent reactance (right) as a function of frequency (logarithmic scaling) when using the two-Ag/AgCl-electrode configuration.

The identified RC values fitted to the most appropriate circuits for both electrode configurations are given in Table 6. The symbol "x" in the table stands for "no capacitance value" due to the fitting of only two parallel RC circuits in series for the computed impedance spectrum of the model with the two-glass-electrode configuration. As it can be seen in Table 6, to perfectly fit the impedance spectrum of the computed values obtained from the numerical simulations with membrane sample using the two-Ag/AgCl measuring configuration, a third RC parallel circuit in series had to be added. The second RC parallel circuit remained exactly the same in both cases. The difference of three orders of magnitude is more than obvious when comparing the values computed with the two different electrode configuration.

electrode configuration	membrane insertion	identified values					
		R_1 [kΩ]	C_1 [pF]	R_2 [kΩ]	C_2 [pF]	R_3 [kΩ]	C_3 [pF]
two-glass	no	$3.872 \cdot 10^3$	1.52	$9.47 \cdot 10^3$	6.53	x	x
	yes	$3.873 \cdot 10^3$	1.52	$9.5 \cdot 10^3$	6.53	x	x
two-Ag/AgCl	no	1.755	2.71	0.065	7.47	x	x
	yes	2.593	6.46	0.065	7.47	0.703	4.68

Table 6: Identified parameter values obtained from the computed impedance in COMSOL Multiphysics® considering the Ussing-like model with two different electrode configurations.

The above-presented and summarized results indicate that for conducting feasible experiments, two models could be appropriate and therefore very desirable - the modified *in vitro* model 2 (one big glass electrode against a disc Ag/AgCl electrode) as well as the newly designed Ussing-like model using either the two-glass electrode configuration or the two-Ag/AgCl wire electrode configuration.

5.2 Measured data

5.2.1 General considerations: operation, control and signal flow

The acquisition of accurately measured data depends strongly on the experimental setup and its calibration and thus, test and tuning procedures are necessary for optimal recordings. Therefore, the passive SEC (Single Electrode Clamp amplifier) cell model [72], [73] has been chosen, suitable for use with single electrode amplifiers (in this case the npi SEC-10 LX BF) to check the function of the instruments.
Additionally, a different type of amplifier (Lock-In SR830) was included to extrude the influence of undesired frequencies in the measurements. The latter, operates in frequency domain and hence provides simplified and faster data analysis.

The start was given by investigating the operation mode of the npi SEC-10 LX BF amplifier and adjusting the device parameters. Next, the relevant measurement parameters and configuration were optimized. Therefore, an externally generated current signal was applied and voltage values were recorded, the data was converted, acquired and analysed. Afterwards, the same procedure was performed with the Lock-In SR830 amplifier that was directly connected to the npi SEC-10 LX BF operating in time domain. The lock-in amplifier was computer-controlled via a RS232 data interface using the MATLAB®/Test and Measurement Tool. For the purpose of this study a special MATLAB script was developed, to automatically send the amplitude and the frequency of the excitation signal to the device and to store the measured data (impedance spectrum) sets of X (real part of the impedance) and Y (imaginary part of the impedance) or R_m (magnitude of the impedance) and θ (phase difference).
Finally, comparison and optimisation of the measured and simulated data was performed as presented in the following sections.
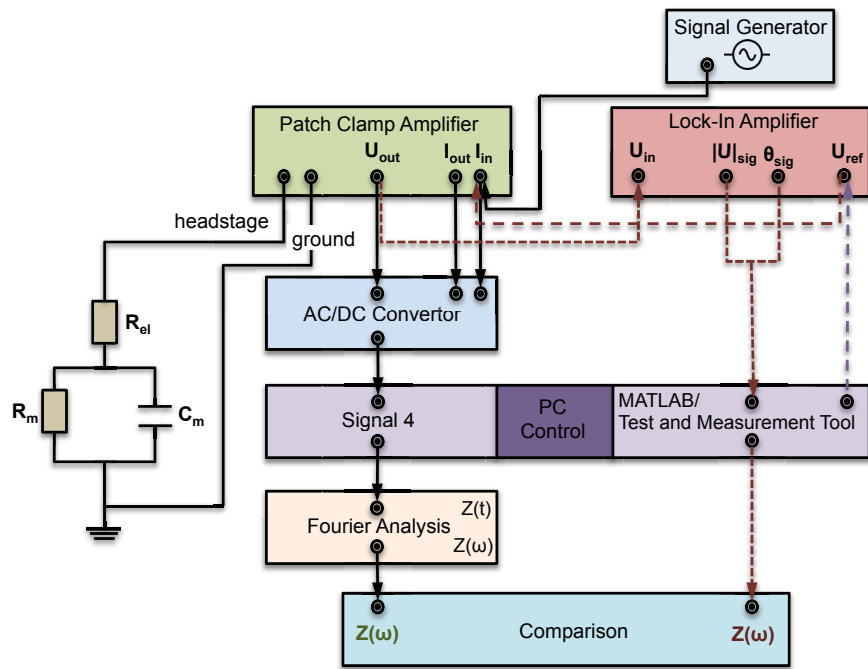
Figure 5.26: A schematic diagram of the experimental setup: analysis flow chart.

5.2.1.1 Test and tuning procedures: verification and validation with the passive cell model (SEC)

Once the above-described steps were accomplished, measurements using a passive SEC (Single Electrode Clamp amplifier) cell model [72], [73] took place, guided by the geometry complexity of the *in vitro* model and the difficulty in distinguishing of glass microelectrode properties. Current injections and voltage recordings were performed with a single-electrode clamp amplifier (npi SEC-10 LX BF) in "the bridge balance" operation mode. Hence, two different series of measurements were conducted - electrode resistance and voltage measurements.

(a)
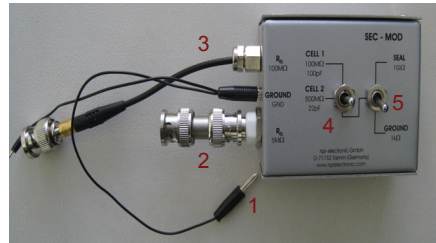
(b)

Figure 5.27: The experimental setup including the SEC (a) and the SEC model itself (b).

The SEC model is indeed a combination of electric circuits with known resistor (R) and capacitor (C) values, which represent the electrical properties of an electrode and a cell. With switch 4 (Figure 5.27, (b)) one can switch between two different cell types with different parameters. The CELL 1 (switch 4, upper position) simulates a medium sized cell with a resistance of 100 MΩ and a capacity of 100 pF whereas the CELL 2 (switch 4, down position) simulates a small sized cell with a resistance of 500 MΩ and a cell membrane capacitance of 22 pF. Furthermore, switch 5 (Figure 5.27, (b)) allows simulation of a bulk resistance 1 kΩ (down position) or a seal formation 1 GΩ (upper position). It is also possible to switch between a 100 MΩ (sharp) and a 5 MΩ (patch) electrode by using connection 2 or 3 connected to the headstage of the npi amplifier.
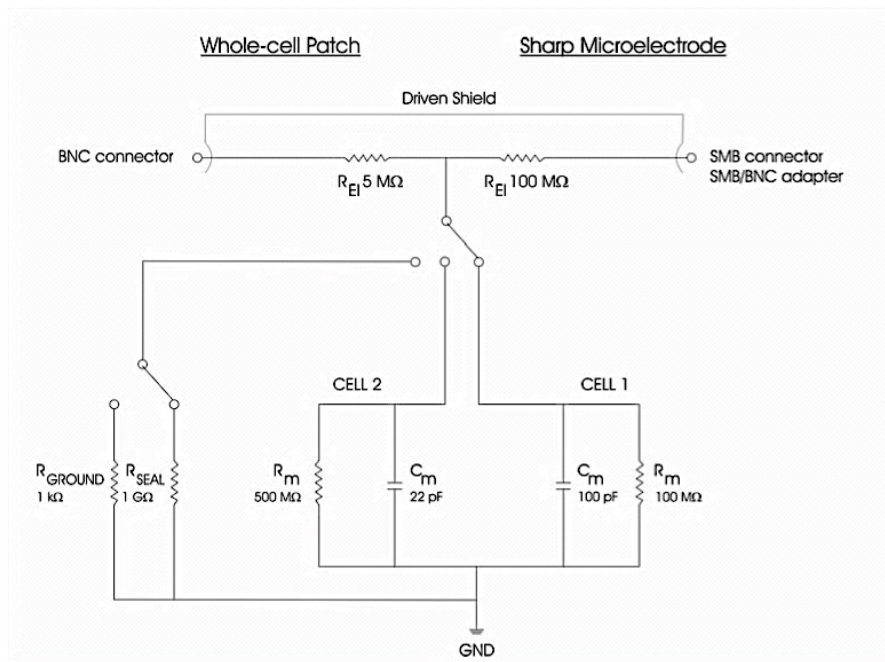
Figure 5.28: A schematic diagram of the passive cell model - SEC [72].

Thus, various different electric circuit possibilities exist (Figure 5.28) and for this study, RC parallel circuit combinations also in series with the two types of electrodes were considered and used for the measurements. Altogether, the voltage response of eight different RC circuits was measured and simulated in time and frequency domain. In order to determine the accuracy of the measurements (deviations between a sequence of same measurements), for each of the eight cases, series of ten to thirty measurements were conducted and the computed mean value was taken into account for the further analysis. Simulations were performed, using the resistance and capacitance given from the manufacturer of the SEC model cell and a comparison between the identified and the ideal R and C values was made.

Firstly, the SEC model was connected to the headstage (connection 2 or 3, Figure 5.27 (b)) and before starting with signal recording, the resistance of the electrode was measured (usual procedure when measuring with glass microelectrodes). This is done by applying a current square pulse ($I_0 = 1$ nA, $T = 2$s, sample rate at 20 kHz). Generally, since the resistance of the electrode is unknown, it can be determined by adjusting a

knob on the amplifier until the steady state pulse response is eliminated (the voltage drop across the electrode is zero). Next, a straight voltage trace with artefacts caused by the potential drop across the electrode was to be seen (Figure 5.29). After the bridge circuit is balanced, the electrode resistance can be read out [71], [97], [98]. The artefacts at the onset and finish of the step result from the capacitance transients that can be also compensated. Finally, a zero voltage trace without artefacts should be achieved. As a result, the electrode resistance and all the capacitive influences are fully compensated. The compensation of the electrode resistance is only done when the electrode properties should not be taken into account and affect the measurements done on a cell or tissue. As mentioned above, in the measurements with the SEC model, the electrode resistance is in some cases compensated, in others not.

(a)   (b)
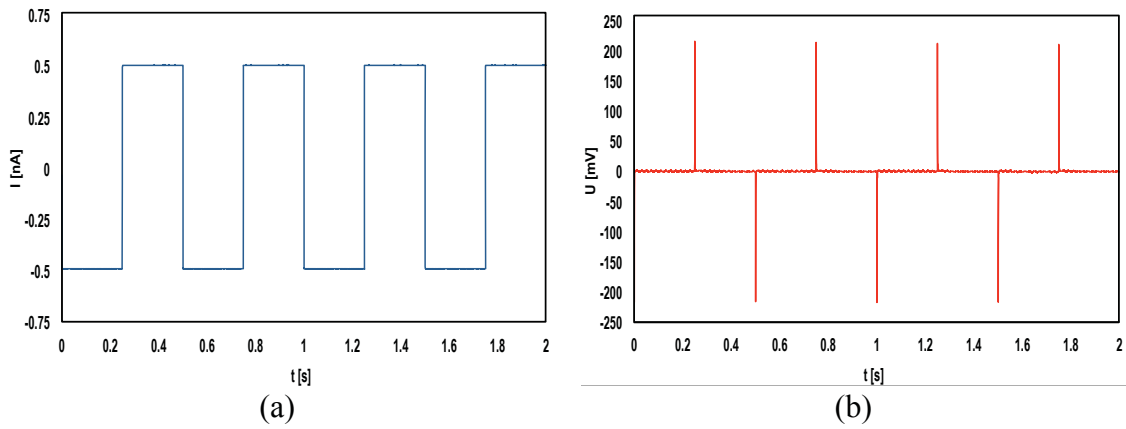
Figure 5.29: Adjustment of the bridge balance: current command signal (a), potential output after compensation of the capacitance (b).

Furthermore, for the study, a swept-sine-wave (chirp or ZAP-impedance amplitude profile [99]-[103]) current signal with constant amplitude I_0 and linearly increasing frequency was applied and a voltage signal was measured (Figure 5.31). The input current impulse with linearly modulated frequency can be expressed in the form:

$$I(t) = I_0 \sin(f_{start}t) + (f_{end} - f_{start})\frac{t^2}{2T}$$

(5.1)

where f_{start} and f_{end} are the initial and final instant frequencies of the sweep, respectively, and T is the duration of the chirp pulse. A wave form of a chirp signal is presented in Figure 5.30.

The advantage of this multi-frequency-one-time measurement technology over the common sine wave excitation (single frequency at a time) is the enormously reduced measurement time, shortening of the stored data sequence as well as fast grasping of the transient physiological changes in living tissues [104]. The amplitude of the response of such signal is attenuated and phase-shifted to the excitation at every time instance, depending on the instant frequency of the chirp.
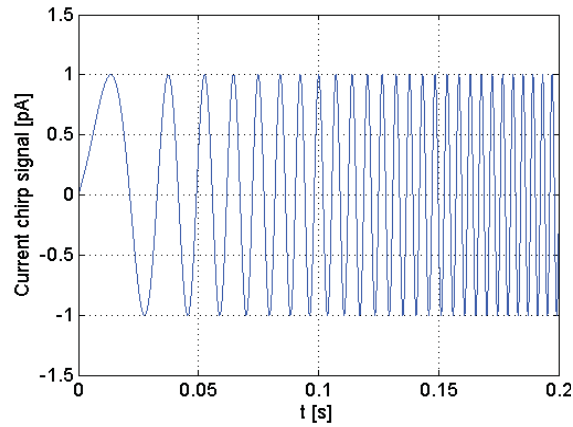
Figure 5.30: An example of a test chirp signal generated in MATLAB®/Simulink®.

In the particular experiments, the input current stimuli (constant amplitude peak-to-peak value: $I_{pp} = 0.5$ nA, $f_{start} = 0.5$ Hz; $f_{end} = 0.5$ kHz, $T = 2$s) and the recorded voltage were digitized at a sampling rate of 100 kHz and transformed into the frequency domain using the fast Fourier transform (FFT). Figure 5.32 shows the FFT magnitude of the current signal ($\mathbf{F}\{i(t)\}$) and the recorded voltage ($\mathbf{F}\{u(t)\}$) corresponding to the measured signals in time domain, illustrated in Figure 5.31. In this case the CELL 1 (parallel RC circuit, $R_1 = 100$ MΩ and $C_1 = 100$ pF) was considered and it was measured with the npi-amplifier (time domain). The sharp electrode (connection 3) in series to this circuit was measured before and compensated ($R_e = 101$ MΩ).
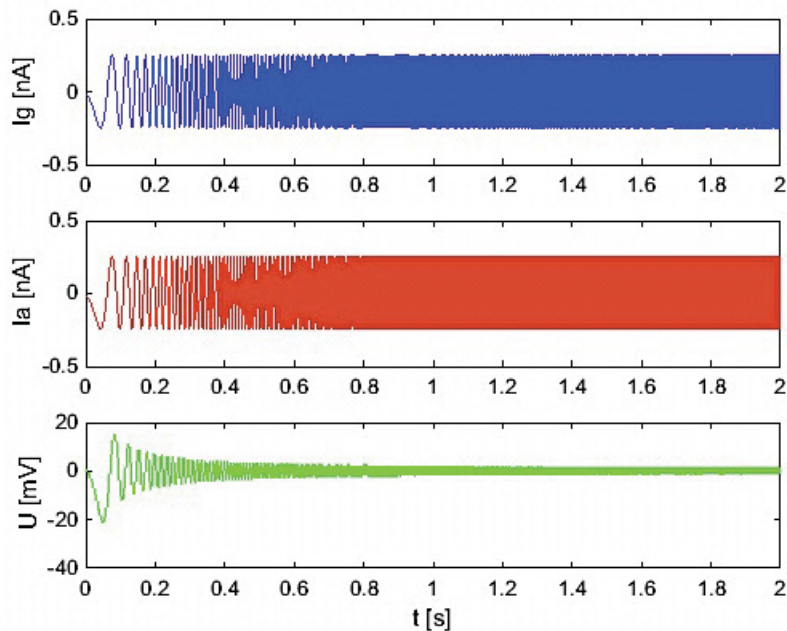
Figure 5.31: Measured data in time domain for CELL 1 ($R_1 = 100$ MΩ and $C_1 = 100$ pF) from the SEC model: current stimulus (blue), current output (red), registered voltage (green).
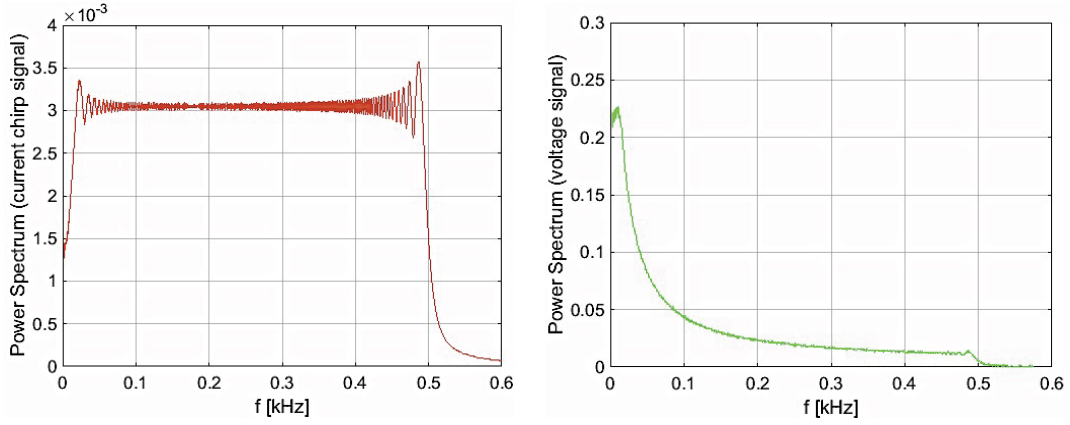
Figure 5.32: Power spectrum (FFT) of the injected current chirp (left) and the measured voltage response (right) (CELL 1).

Afterwards, the impedance values for the frequency range from 0.5 Hz to 0.5 kHz were computed. The complex impedance value at a given frequency was determined as:

$$\mathbf{Z}(\omega) = \frac{\mathbf{F}\{\text{voltage response}\}}{\mathbf{F}\{\text{current input}\}} = Z_{real} + jZ_{imag} = |Z|e^{-j\theta} \qquad (5.2)$$

where Z_{real} and Z_{imag} are the real and imaginary component of the impedance; $|Z|$ is the absolute value of the impedance and θ the phase shift between the voltage and current signal.

For analysis purposes and rough estimation of the system parameters, the impedance values were displayed in three different figures. The plots of the absolute value of the impedance ($|\mathbf{Z}|$) and the phase shift θ against frequency are shown in Figure 5.33 whereas in Figure 5.34, Im($\mathbf{Z}$) and Re($\mathbf{Z}$) are plotted against frequency. Figure 5.35 shows the equivalent resistance (Z_{real}) against the equivalent reactance (Z_{imag}).
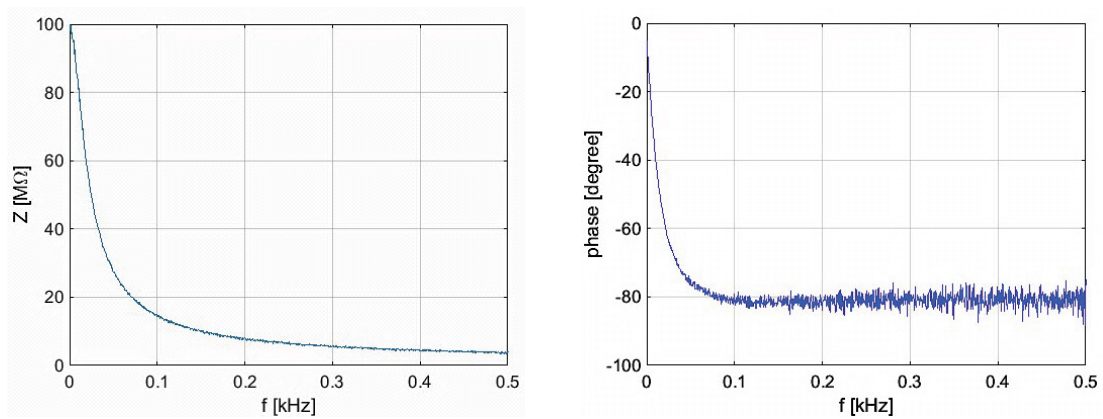
Figure 5.33: Absolute value of the impedance as a function of frequency (left); phase shift between current input and voltage response as a function of frequency (right) (CELL 1).

Figure 5.34: Equivalent resistance (left) and equivalent reactance against frequency (right) (CELL 1).

As expected, the presented results show the behaviour of a resistor in parallel with a capacitor that was also confirmed with the system identification and parameter estimation.
The absolute value of the complex impedance at a frequency near zero is around 100 MΩ, which is the resistance value of the CELL 1, gradually decaying until the cutoff frequency, the point where the signal is attenuated to half of its power. The cutoff frequency ($f_c = 1/2\pi\tau$) determined by its time constant ($\tau = RC$) is equal to 15.3 Hz which is similar to the analytically computed value of 15.9 Hz. The absolute value of the impedance approaches zero as the frequency increases. The phase difference between the voltage and current source in the measured frequency range attenuates slowly to approximately 84º. The phase angle of a parallel RC circuit is always somewhere between 0º (purely resistive circuit) and 90º (purely capacitive circuit). In Figure 5.34 and in Figure 5.35, can be seen that lower frequency signals are passed through the resistor, whereas higher frequency signals are attenuated and the reactance drops.
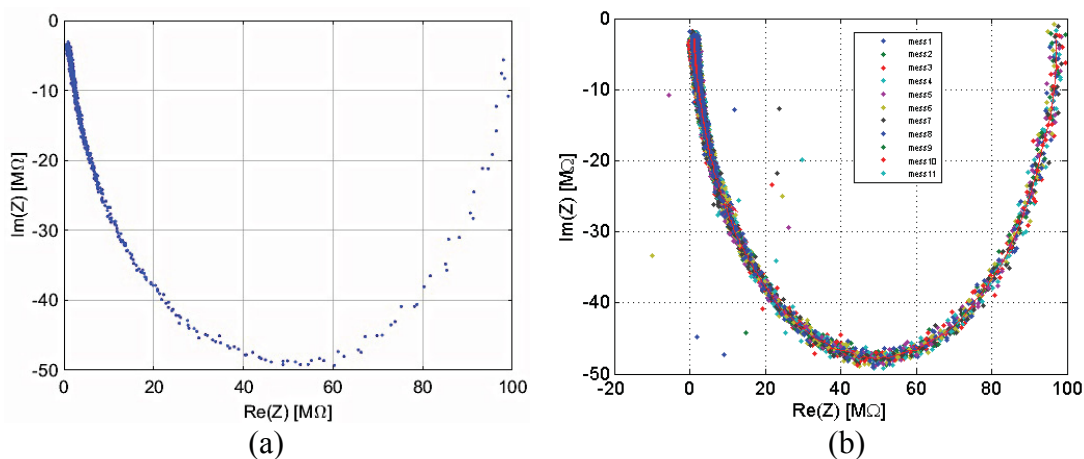
Figure 5.35: Plot of the equivalent resistance against equivalent reactance (CELL 1): one measurement (a) and a series of measurements (b).
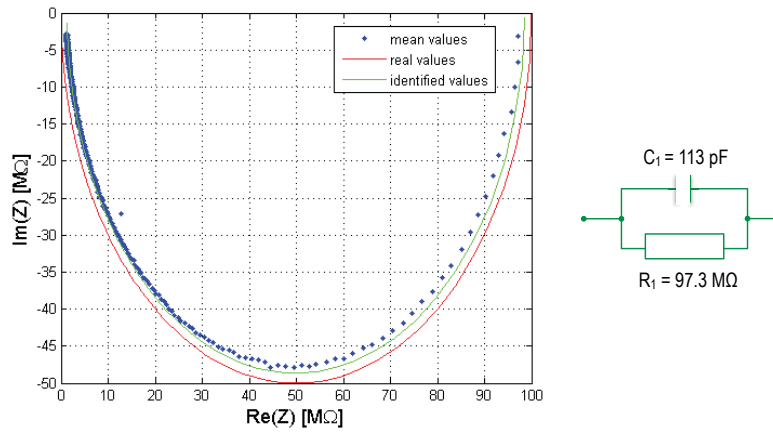
Figure 5.36: Plot of the equivalent resistance against equivalent reactance: computed values with the lumped-parameter model in MATLAB®/Simulink® using the RC circuit of CELL 1 (ideal case, red); the mean value of the series of measurements (blue), identified values (green).

A case with the sharp electrode (R_e = 100 MΩ) in series with the CELL 1, was also accounted for the measurements. In Figure 5.37 and Figure 5.38, the results of a series of measurements are shown.

When comparing the results in the impedance plane in Figure 5.35 and Figure 5.38 it can be seen that the semi-circular arc of the electrical circuit of resistor in parallel with capacitor in Figure 5.35 is only shifted on the x-axis in Figure 5.38 for the value of the electrode resistance, so that the resulting resistance R at $\omega \to 0$ is equal to $R = R_e + R_1 =$ 200 MΩ and at $\omega \to 500$ Hz is equal to $R_e = 100$ MΩ. The cutoff frequency is at 23 Hz.
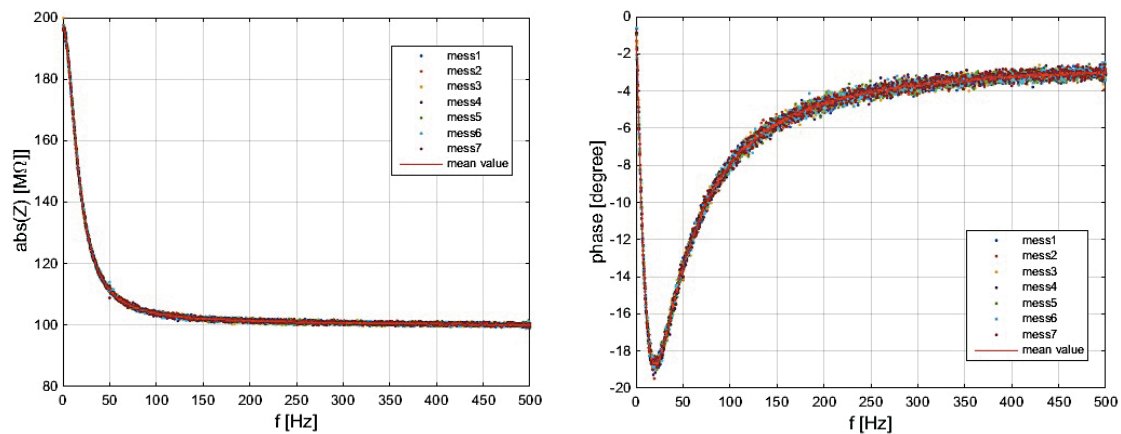
Figure 5.37: Plot of impedance data of series of measurements: absolute value of the impedance as a function of frequency (left); phase shift between current input and voltage response as a function of frequency (right) (sharp electrode R_e in series with CELL 1).
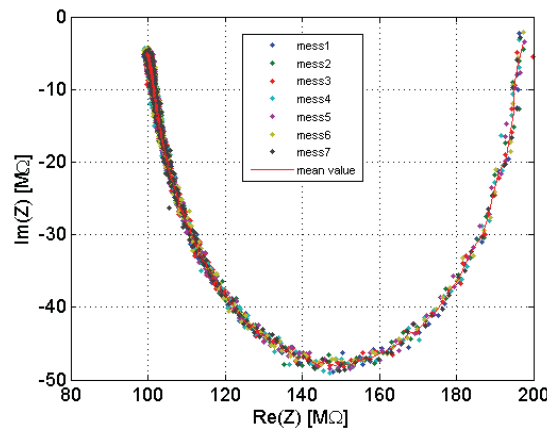
Figure 5.38: Plot of the equivalent resistance against equivalent reactance: series of measurements (different colours) and their mean value (red) (sharp electrode R_e in series with CELL 1).

For all eight cases also measurements were made with the lock-in amplifier. The input excitation signal had an amplitude of $I_0 = 0.2$ nA and frequencies in the range between 5 Hz and 10 kHz. The used lock-in amplifier model was not able to generate sweep signals. Therefore, altogether, 100 frequencies (measurement points) were used linearly allocated in the used frequency range. The time between two single measurements (two different frequencies) was 3s. Afterwards, a comparison with the time domain measurements was made. The data analyses process remained the same.

In Figure 5.39 and Figure 5.40 the impedance data obtained from the npi-amplifier (FFT of the mean values of series of measurements), the lock-in amplifier and the computed values with the lumped-parameter model in MATLAB®/Simulink® consisting of a sharp electrode $R_e = 100$ MΩ in series with RC circuit of CELL 1 is shown.
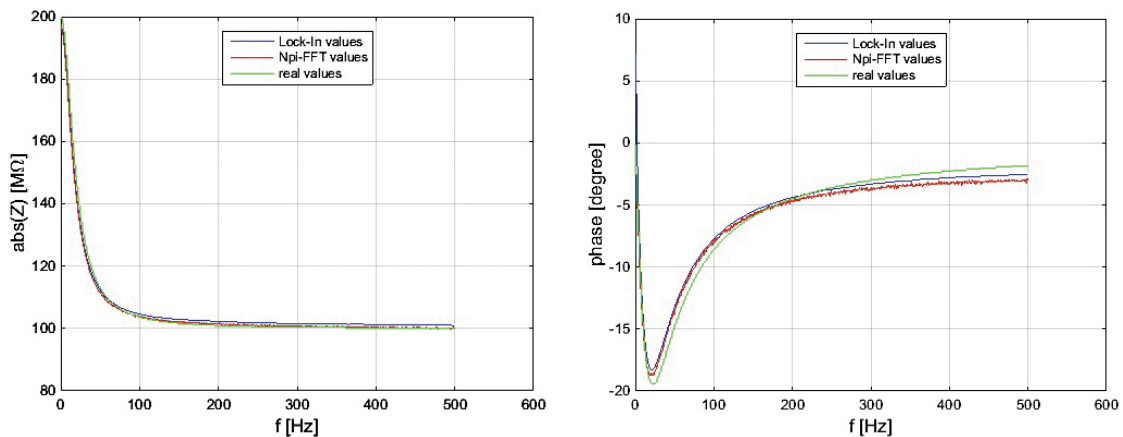
Figure 5.39: Plot of impedance data obtained from the npi-amplifier (FFT values, red), the lock-in amplifier (blue) and computed values in MATLAB®/Simulink® (green): absolute value of the impedance as a function of frequency (left); phase shift between current input and voltage response as a function of frequency (right) (sharp electrode R_e in series with CELL 1).
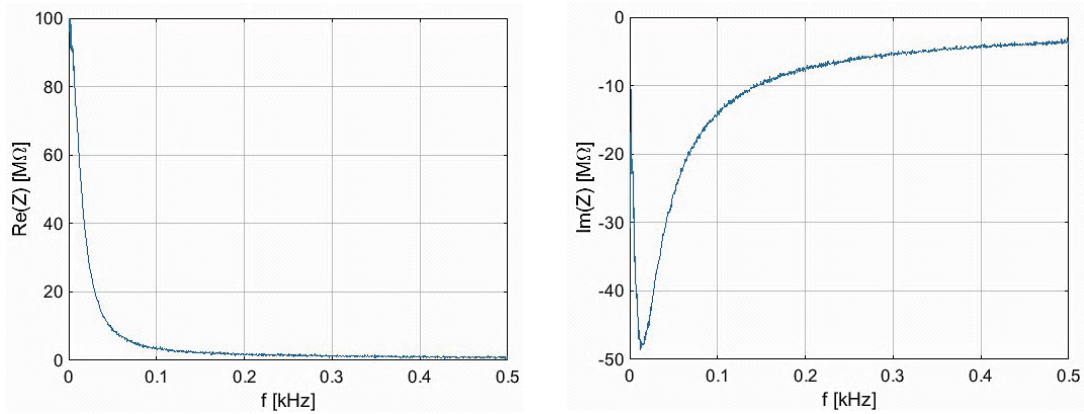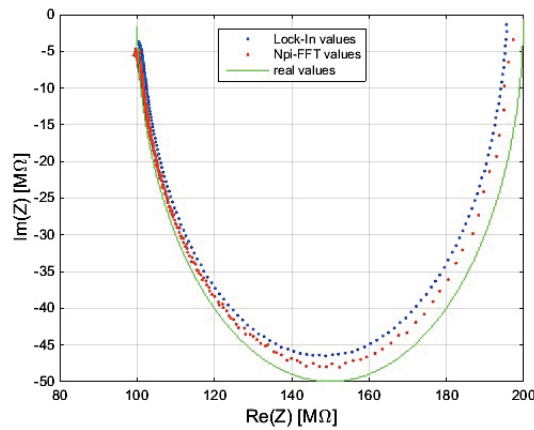
Figure 5.40: Plot of the equivalent resistance against equivalent reactance: data obtained from the npi-amplifier (FFT values, red), the lock-in amplifier (blue) and the computed values in MATLAB$^®$/Simulink$^®$ (green) (sharp electrode R_e in series with CELL 1).

The identified R and C values of all the measurements conducted on the SEC model with the npi- and lock-in amplifier are given in Table 7.

	model	**identified values**					
		npi-amplifier			lock-in amplifier		
		R_e [MΩ]	R [MΩ]	C [pF]	R_e [MΩ]	R [MΩ]	C [pF]
CELL 1	C₁ / R₁	<u>101</u>	97.3	113	<u>101</u>	93.82	106
		<u>5</u>	95.39	112	<u>5</u>	97.163	108
	Rₑ C₁ / R₁	100.5	98.11	108.7	99.368	91.77	106
		6.34	97.23	120	4.98	96.98	108
CELL 2	C₂ / R₂	<u>101</u>	477.8	35.86	<u>101</u>	437	35.6
		<u>5.1</u>	460	36	<u>5</u>	451.5	35.1
	Rₑ C₂ / R₂	103.68	456	36.3	101.22	437	35.67
		8.34	456	36.4	5.08	445	35.4

Table 7: Fitting parameter results for the SEC model obtained from the npi- and lock-in amplifier.

The underlined resistance values in the table indicate the cases in which the electrodes were compensated before the measurements started. These are the values read out from the npi-amplifier after the bridge balance. The identified values are grouped into two groups for each CELL. The first group contains R and C values of a parallel circuit (the

electrode resistance is compensated) whereas the second group, R_e, R and C values of a circuit of resistance in series with parallel RC circuit.

As it can be seen in Table 7, both models in both cases were fitted well with a certain deviation in the values in comparison with the resistance and capacitance given from the manufacturer of the SEC model cell. In all cases it is obvious that, though careful stray capacitance compensation, still up to 20 pF are not fully compensated. The capacitance and resistance compensation was especially challenging when considering the 5 MΩ electrode due to the noisy signal response to the input square pulse. When comparing the resistance values (identified and given for the npi-amplifier) for each of the CELLs, it can be observed that the agreement between identified and given values is reasonable with a maximum relative error of 5% for R_1 and 8% for R_2. For the lock-in amplifier, the maximal discrepancy was estimated to be 7% for R_1 and 12.6% for R_2.

To summarize, an important fact is that with both amplifiers, similar results were obtained.

5.2.2 The glass micropipettes - geometry characterization

The quantification of the exact dimensions of the glass microelectrodes is crucial for both precise modeling of the experimental setup and for optimization and analysis of the measurements. The drawn glass pipettes were examined under digital microscope imaging in order to characterize their geometry, the inner and outer diameters, millimetre by millimetre starting from the tip until the beginning of the pipette's shoulder (Figure 5.41).
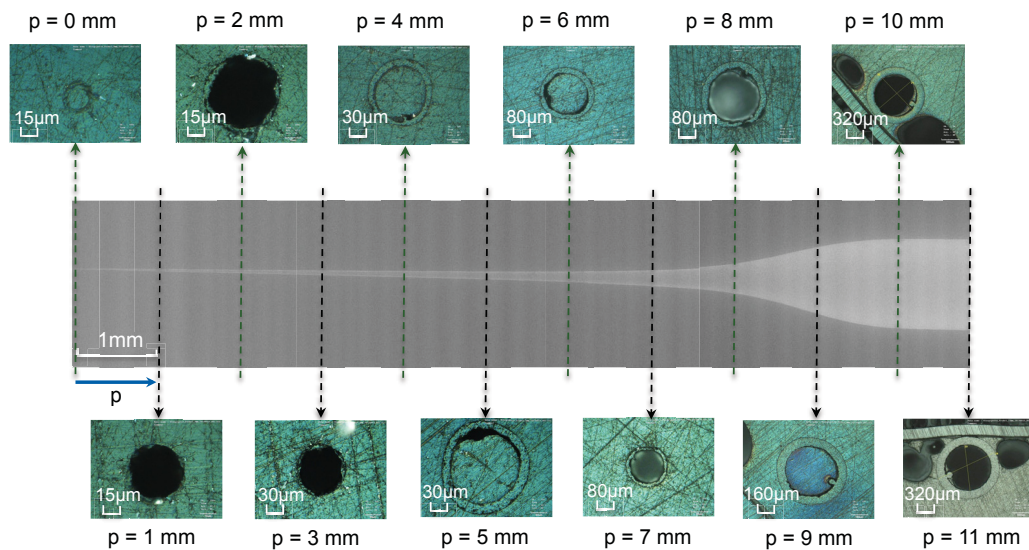
Figure 5.41: Glass pipette geometry measurement: LEXT images of embedded quartz glass pipette made at a millimetre distance starting from the tip opening of the micropipette up to 11 mm distance from it.

The whole preparation procedure is explained in section 3.3.2.2.1. Several tenths of pipettes were pulled and investigated but by only few, the geometry characterization was successfully fulfilled. Hence, in the first block of geometry characterization, the

focus was set on four single quartz micropipettes, as well as five two-pipette configurations (a borosilicate pipette fixed to a quartz pipette). They were visually investigated with digital microscope imaging (Figure 5.41) and scanning electron microscopy (Figure 5.43).
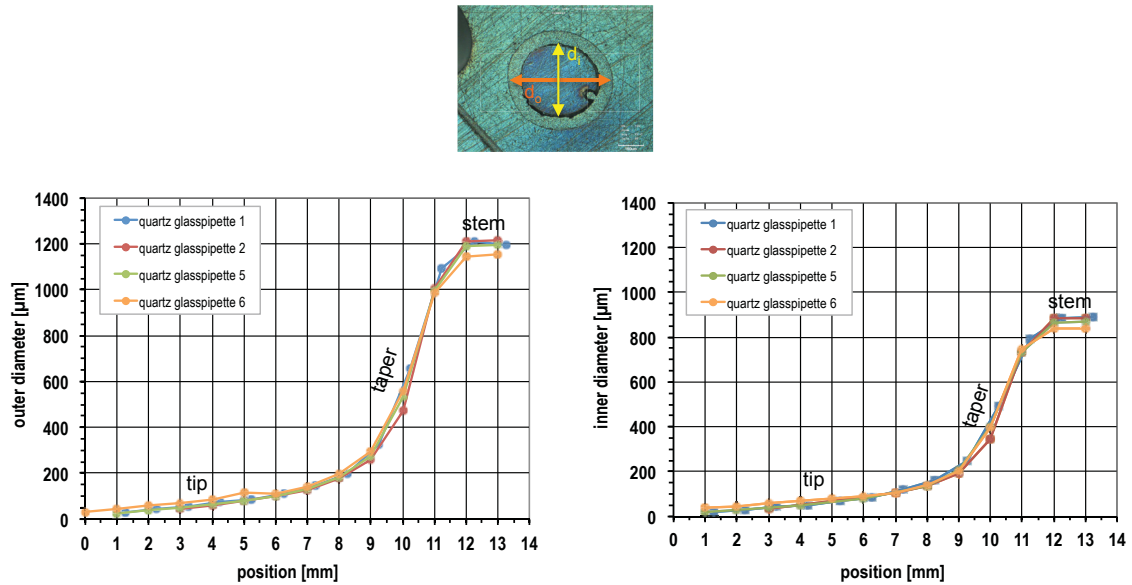
Figure 5.42: The outer and inner diameter of the quartz glass micropipettes as a function of a measurement position.

Figure 5.42 reveals the values of the outer and inner diameter of four quartz pipettes and as it can be seen in the tip-taper area the diameters are nearly linearly increasing by millimetre length. The relative change of the outer to inner diameter deviates in the range between 1.3 and 1.4. The ratio of the outside to the inside diameter of a quartz glass tube has a constant value of 1.33.

(a)   (b)   (c)
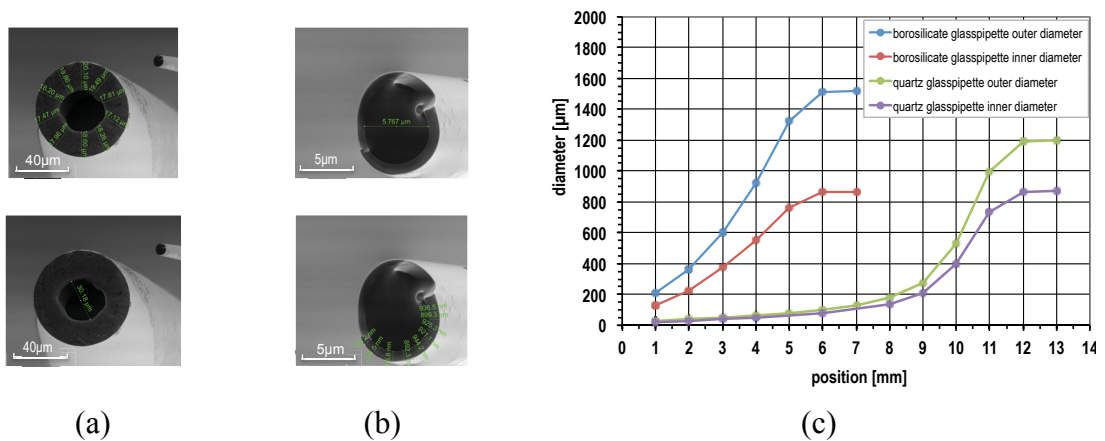
Figure 5.43: SEM images of the borosilicate and quartz glass configuration (a) and (b); outer and inner diameter of the borosilicate and the quarz glass micropipettes as a function of the measurement position (c).

Next, the geometry of a two-pipette configuration (borosilicate and quartz pipette) was characterized using SEM. Figure 5.43 shows the difference in glass thickness, inner and outer diameters and length of the tip, of the borosilicate and quartz micropipette.

Furthermore, in the second block of microscope imaging, seven borosilicate and seven quartz glass micropipettes were successfully investigated. This time, after the pulling process, each half of the glass tube was considered and investigated to see if there are some significant changes in the geometry. Firstly, the length of both pipette types was optically observed and measured using light microscopy. For the borosilicate pipettes, three to four images were made along the length of the samples, whereas for the quartz pipettes seven to eight. Each of these images were then carefully attached together and put in a sequence using GIMP- GNU image manipulation software. Images of a quartz and borosilicate pipette together with the average lengths of the tip, taper and stem of the quartz and borosilicate pipettes are shown in Figure 5.44. The average length of the observed quartz pipette is 12645 μm whereas of the borosilicate pipette is 7236 μm.

9735 μm   1830 μm   1080 μm

(a)

(b)

4784 μm   1688 μm

764 μm
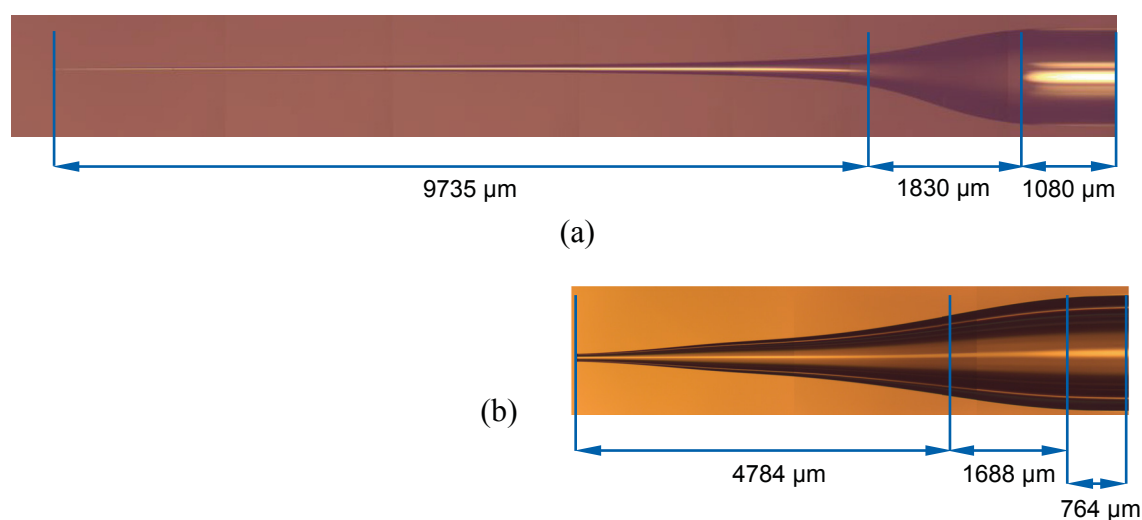
Figure 5.44: Light microscope images and glass pipette length geometry data: (a) quartz pipette; (b) borosilicate pipette.
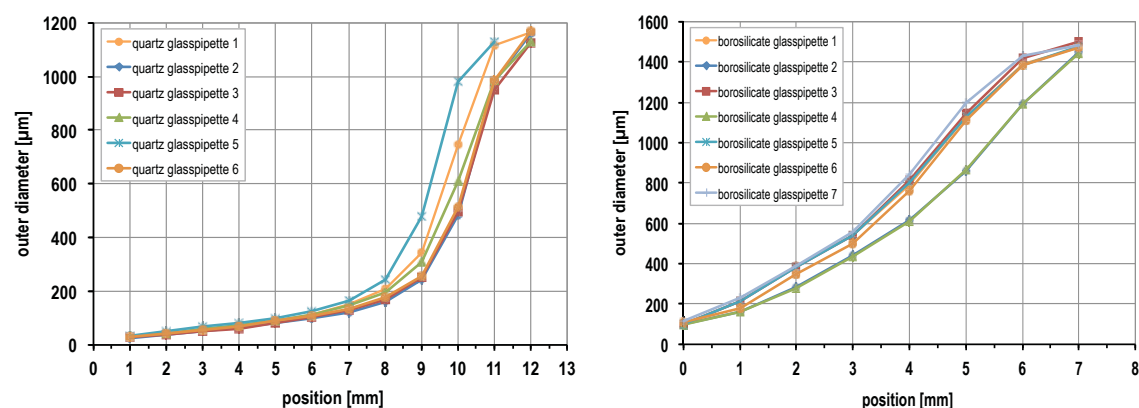
Figure 5.45: The outer diameter of the quartz and borosilicate glass micropipettes as a function of the measurement position.

From the results shown in Figure 5.45 it is evident that the measured outer diameters of the quartz glass from both block measurements are approximately the same. Thus, a very good reproducibility of the pipettes is possible. The small deviation in the curves appears because each of the two pulled halves from one glass tube was considered. Other than the quartz glass measurements, the measurements of the borosilicate pipette show a difference of about 100 μm per millimetre length in the tip region. It seems as if in the first block of measurements, one millimetre of the tip was broken.

Moreover, a scanning electron microscope was used for characterizing the tiny diameter of the quartz pipette. SEM images were also made of the borosilicate pipettes. The images showed that the outer diameter of the quartz pipette tip deviates between 70 and 104 nm. The outer diameter of the borosilicate pipette tip is between 80 and 100 μm and the inner between 45 and 60 μm, respectively. Unlikely, the observed estimates of the diameter of the borosilicate pipette are several times bigger than the expected (proposed) one of ca. 10 μm. Hence, the setting parameters of the pipette puller have to be carefully checked once more.

(a)   (b)
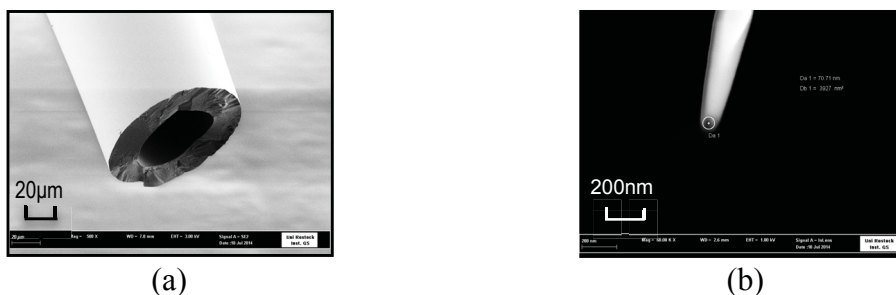
Figure 5.46: SEM images of a borosilicate (a) and quartz pipette (b).

When filled with an aqueous composition of 3M CH_3COOK (0.2942g/ml potassium acetate) mixed with 300 mM KCl, the glass electrodes fixed to each other had a final resistance of approximately 70-90 MΩ. These values agree in the order of magnitude with those calculated from the dimensions of the quartz electrodes.

The geometry characterization is very delicate and tedious due to the fragile and tiny pipette probes. Therefore, to get accurate data, no contamination, careful transportation and skillful handling of the pipettes is of great importance.

5.2.3 Electrolytes – electrical conductivity measurement

The determination of the properties of electrolytes with respect to the dependence of their electric conductivity on concentration demands very accurate experimental data. There are several factors that may influence the accuracy of these measurements: temperature and humidity, purity and accuracy of the concentration of the solutions during preparation, storage, and measurement.
Electrolytes are aqueous solutions containing ions. The ions in the diluted solutions are responsible for carrying the electric current. The electrolytes can be either strong or weak. Strong electrolytes (for example KCl or CH_3COOK) are completely dissolved

(ionised) in solution. Thus, the concentration of ions (number of charge carriers) in the solution is proportional to the concentration of the added electrolyte. Weak electrolytes are aqueous solutions that are not fully ionised in solution. They can conduct electricity, but normally not as well as a strong electrolyte due to the fewer ions that carry the charge from one electrode to the other.

Theoretically, the conductivity should increase in direct proportion to concentration ($\sigma \sim c$). However, the experiments show that for certain chemicals at high levels (high concentrations), the conductivity is not directly proportional to the concentration, but increases mostly linearly with respect to the square root of the concentration [105]. For more details, in [106] tables and graphs of conductance values for the majority of commonly used electrolytes, are encountered and presented.

Before running a series of conductivity measurements of the solutions of interest, measurements were carried out with 0.1 M KCl, 0.3 M KCl and 3 M KCl solutions for calibration (accurately known electrolytic conductivity values exist in the literature).

The reference measurement temperature is 25 °C and the results are expressed in S/m.

The measured values are given in Table 8.

electrolyte	composition	σ [S/m]
perilymph	4mM KCl + 140mM NaCl	1.6
ACSF	124mM NaCl + 26mM NaHCO$_3$ + 3mM KCl + 1,25mM NaH$_2$PO$_4$ + 2,5mM CaCl$_2$ + 1,3mM MgCl$_2$ +10mM Glucose	1.519
pipette electrolyte	3M CH$_3$COOK + 300mM KCl	15.8

Table 8: Measured conductivity values of the electrolytes.

Unfortunately, the measured values of perilymph and the pipette electrolyte, do not match their analytically calculated conductivity values. Therefore, to achieve accurate numerical simulations, the values of the conductivity in the models should be adapted.

5.2.4 Microscopic membrane characterization

To determine the tightness and thickness of the tissue, tissue samples were examined under a laser-scanning microscope. Images of the samples were made in different field depths (Figure 5.47).

| (a) | (b) |
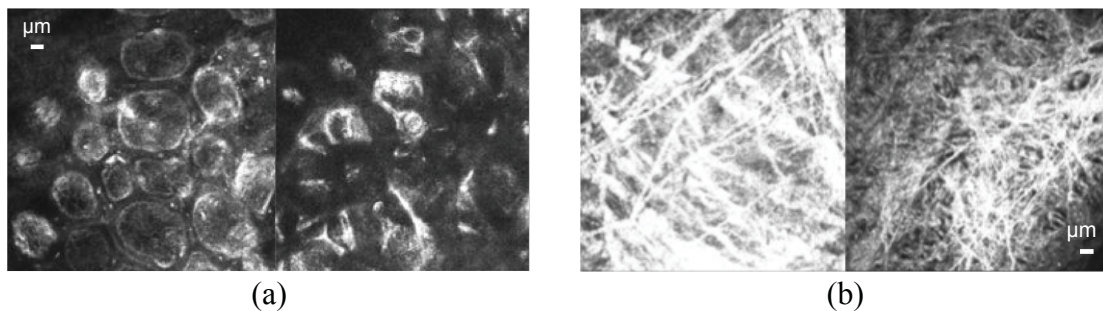
Figure 5.47: Images of the double-layered mesentery (a) and a collagen layer (b) [77].

All observed tissue samples were as fresh as possible, mostly within four to five hours of animal death. Changes in the tissue morphology were observed during the microscopic examinations. During the examination, the tissue was not surrounded by a nutrient solution (ACSF) and began to die. The images are made in a period of ten to twelve minutes. After fifteen minutes, the tissue cells were still visible but they started to dry out and eventually were decomposed.

As already presumed, the mesentery of the rat is composed of two cell layers just as the Reissner's membrane in the cochlea. Additionally, it could be observed that a layer of irregularly arranged fibres also exists which most likely are collagen fibres.

6 Conclusion and outlook

The first steps in the process of establishing a novel *in vitro* system have been successfully made. The numerical models have provided unbounded possibilities for studying various *in silico* scenarios to evaluate and optimize the measurement configuration parameters. A systematic elaboration of the measurements has been carried out and test experiments have been conducted. Moreover, various methods and techniques of data collection and analysis and parameter identification were adopted and used. The most suitable and problem-oriented approaches were also presented and explained.

In the frame of this study, significant obstacles had to be overcome in order to obtain feasible *in vitro* experimental data. Therefore, the particular measurement system was subjected to a variety of modifications and tests. Firstly, the amplifier as well as the pipette holder were modified to exclude the influence of possible uncompensated capacitance coming from the electronic devices. Additionally, a different type of amplifier (Lock-In SR830) was included to extrude the influence of undesired frequencies in the measurements. Next, the *in vitro* system underwent minor alterations and inclusion of a third electrode (Ag/AgCl disc electrode) was foreseen. Subsequently, a newly designed Ussing-like chamber and two Ag/AgCl wire electrodes were taken in consideration to support the validity of the impedance measurements carried out with the glass-microelectrode configuration.

In order to gain a particular knowledge of the properties of the *in vitro* system, the model has been gradually studied. Initially, a model of one fluid-filled glass microelectrode filled and immersed into salt solutions with different resistivities was designed which provided a better understanding of the electrical properties of such microelectrode. Several different numerical studies were conducted concerning the resistance and capacitance of the microelectrode and the computed impedance values were fitted to an electric RC circuit. The models confirmed that the resistance of a glass microelectrode was inversely proportional to the diameter of the tip opening and that the same glass micropipette may have a wide range of resistances as a microelectrode, depending on the filling and immersing solution. Moreover, as the electrode was submerged deeper into the solution, a linear relationship between the capacitance and the depth of immersion was found. The changes of the capacitance were approximately 0.6 pF/mm compatible with the results (between 0.4 and 1 pF/mm) reported by [87], [92], [93].

Next, a numerical model of the *in vitro* model and the two-electrode configuration was built. In addition, two other model modifications were included that contributed for optimising the design of the particular *in vitro* model. Furthermore, simulations on the newly designed Ussing-like chamber with a membrane holder and using two different electrode configurations (two-Ag/AgCl or two-glass electrodes) were made. This model provided very useful information about the electrode-electrolyte-membrane interface.

The acquisition of accurately measured data depends strongly on the experimental setup and the calibration of the same. Thus, test and tuning procedures were necessary for optimal recordings. Measurements using the passive cell model (SEC) were conducted with the npi- and lock-in amplifier. Next, parameter fitting to two suggested RC circuit models was made. The results showed a good agreement of both measurements.

The numerical and experimental data gained in this study was fitted to one or several equivalent parameter circuits connected in series. The values of the model parameters were estimated by implementing the Nelder - Mead (simplex) method for finding the minimum of a scalar function of several variables. Moreover, a numerical procedure has been developed to automatically convert time domain data into frequency domain.

Along the choice of methodology and calibration of electronic devices, the properties of the glass micropipettes, the exact electrolyte composition as well as the preparation conditions of the biological tissues are one of the crucial factors that can affect the measurement results. Therefore, the geometry of the pipettes (quartz and borosilicate) was successfully evaluated (LEXT and SEM images). The length of the taper, shoulder and stem for every pipette was characterized. Importantly, the opening tip diameter of the quartz pipettes was measured ranging between 70 and 104 μm, whereas for the borosilicate pipette the tip diameter was between 45 and 60 μm. Moreover, the measurements showed that the glass thickness of the pipette increases linearly along the taper. Next, the conductivity of the pipette electrolyte (1.6 S/m), the perilymph (1.519 S/m) and the ACSF (15.8 S/m) was measured. Additionally, the membrane was subjected under image microscopy and as presumed the mesentery of the rat was composed of two cell layers just as the Reissner's membrane in the cochlea. This indicates that the membrane is around 50 μm thick.
To achieve even more accurate numerical simulations, the measured values of the pipette geometry, electrolyte conductivity and membrane thickness should be adapted in the numerical models.

The above-described considerations contributed to the further development, optimization and radical improvement of the *in vitro* experimental setup. Further *in silico* studies and *in vitro* measurements could contribute to conducting feasible *in vivo* measurements. This is far beyond the scope of this study and would require new experimental tests and extensive numerical simulations and analysis. Yet, the necessary basic methods and techniques are now at hand and ready to use as a result of the extensive study described here.

Appendix A

One of the objectives as stated in the introduction was to characterize cochlear membrane properties. In order to achieve this goal, initial impedance measurements on a biological tissue (mesentery) were conducted. These measurements were presented and analysed in [77]. Moreover, the experiment data was fitted to a simple equivalent circuit.

In this section two additional numerical fitting methods are briefly introduced and the procedure of fitting to another equivalent electric circuits is shown. Yet, it should be kept in mind that these measurement were made with a two-Ag/AgCl-electrodes instead of with the primarily suggested two-glass-configuration.

A.1 *In vitro* measurements on a biological tissue: equivalent circuit model and parameter identification

The results analysed and presented here are taken as raw data from a bachelor thesis made in the frame of this project [77]. A very important fact that has to be mentioned is that for these initial experiments, a measurement configuration of two-Ag/AgCl-electrodes instead of the two-glass-microelectrodes, as primary proposed, is used. For this purpose, in the original *in vitro* plexiglass chamber, one wire Ag/AgCl electrode is placed directly over the stretched mesentery whereas the second one, the big disc Ag/AgCl electrode is under the membrane. A schematic diagram of the *in vitro* experimental set up used for the measurements is showed in Figure A.1.
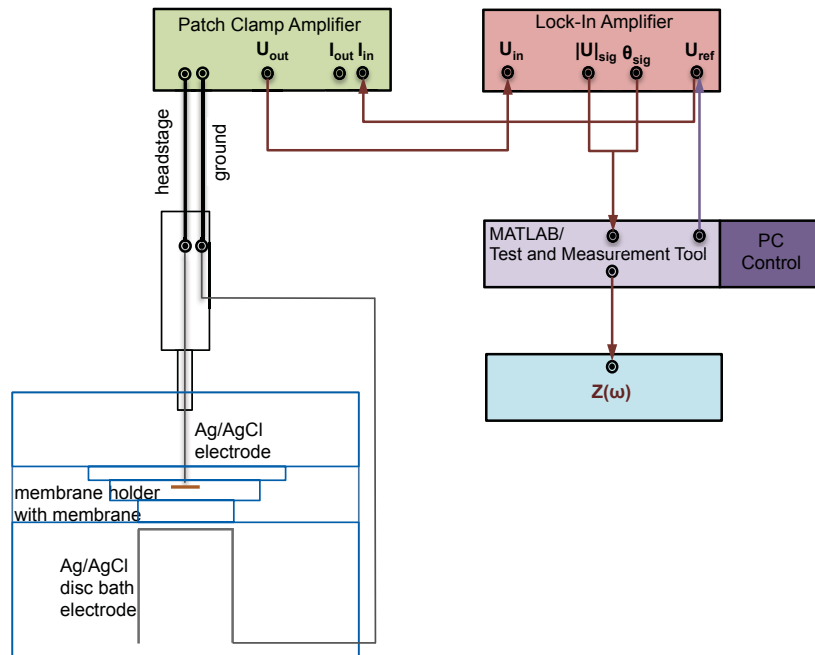
Figure A.1: A schematic diagram of the *in vitro* experimental setup: analysis flow chart.

All included and used electronic devices and software tools in the set up were presented, tested, validated and verified in this doctoral thesis. The measurements were made in frequency domain.

A series of measurements with two different membrane holders (diameter openings 0.5 cm and 1cm) were done. Spectra were recorded at linearly increasing frequencies ranging between 5 Hz and 9 kHz. All measurements were done with an excitation current signal with constant amplitude of 5 nA, at a temperature of 20 °C.

In [77], the measured impedance data is fitted to a simplified transepithelial electrical equivalent circuit as proposed in [107], [108], [109] modeling the apical and basolateral cell membranes as an equivalent resistance (R_{intra}) and a capacitance (C) in parallel. These are connected to a parallel resistance of the paracellular pathway (R_{para}) and in series with the resistance of the measuring electrodes and bathing solution (R_{EL}).
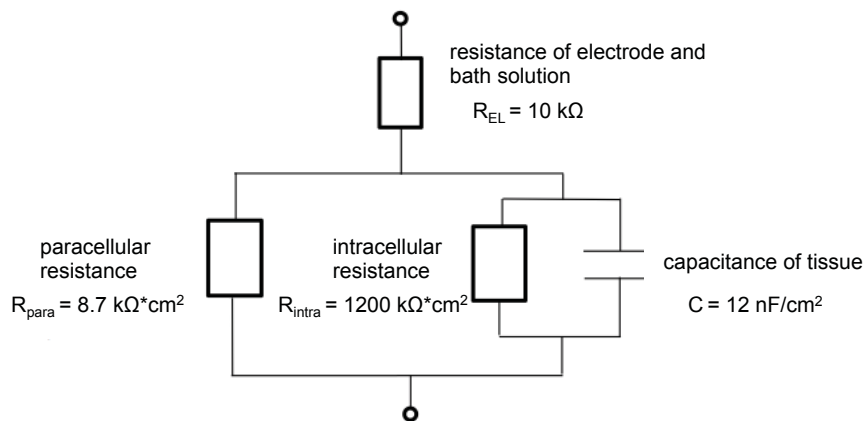
Figure A.2: An equivalent circuit with identified parameters of mesentery and the measuring electrode [77].
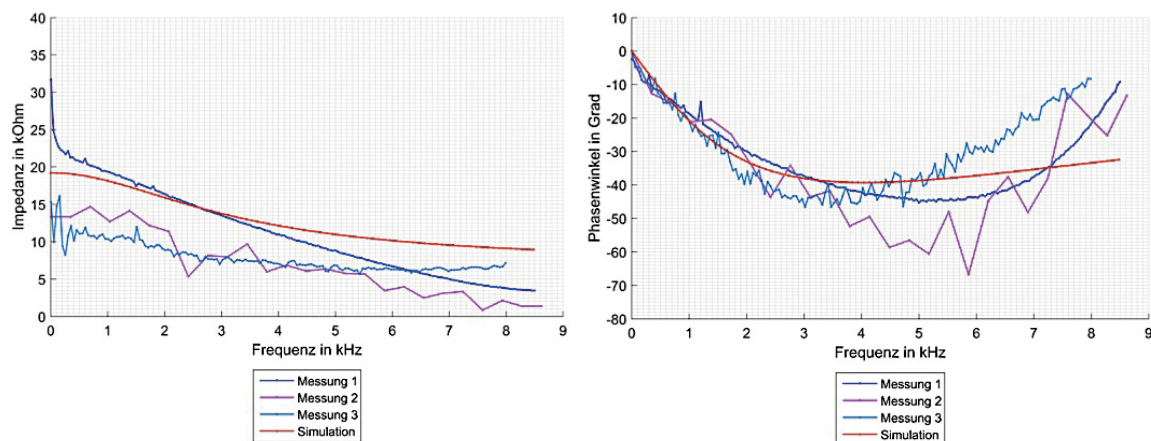
Figure A.3: Plot of measured (shades of blue and magenta colour) and simulated impedance data (red colour) (membrane holder opening with a diameter of 1 cm is used): absolute value of the impedance as a function of frequency (left); phase shift between current input and voltage response as a function of frequency (right) [77].

The equivalent circuit in Figure A.2 is used for modeling the mesentery and the electrode-electrolyte system. As shown in Figure A.3, the chosen electrical model can not exactly fit the experimental data and a certain deviation can be seen. Thus, the electrical behaviour of the mesentery cannot be mimicked in a satisfactory way.

Therefore, an analysis of the measured spectra with a vector-fitting technique [112], [113] can be employed. This numerical method is used for approximation of measured or computed data in frequency domain, solving a linear least square problem and using poles and residues [110]. It is an open-source toolbox implemented in MATLAB$^{\circledR}$ /Simulink$^{\circledR}$ [111]. The impedance response $\mathbf{Z}(s)$ is fitted to an equivalent state-space model (A.1) or alternatively to a pole-residue model (A.2) where s is a complex variable defined as $s = \sigma + j\omega$. The bold entities denote matrices and vectors.

$$\mathbf{Z}(s) = \mathbf{C}(s\mathbf{I} - \mathbf{A})^{-1}\mathbf{B} + \mathbf{D} + s\mathbf{E} \tag{A.1}$$

$$\mathbf{Z}(s) = \sum_{m=1}^{N} \frac{\mathbf{R}_m}{s - a_m} + \mathbf{D} + s\mathbf{E} \tag{A.2}$$

The variables a_m and R_m are the poles and the residues of the system, respectively which are either real quantities or come in complex conjugate pairs, while $\mathbf{D}$ and $\mathbf{E}$ are real and optional. N is the order of approximation. The relation between both models is defined as follows [114] :

$$\mathbf{C}_m = \mathbf{R}_m \qquad\qquad \mathbf{A}_m = (a_m)^{-1}\mathbf{I} \qquad\qquad \mathbf{B}_m = \mathbf{I}$$

$\mathbf{A}$ is a diagonal matrix holding the initial poles, $\mathbf{B}$ is a column vector of ones, and $\mathbf{C}$ is a row vector holding the residues.

This technique can be applied to models of any order and number of ports. Thus, it is also suitable when using different electrode configurations (two-, three- and four-electrode systems).

Figure A.5 shows that the impedance spectra can be better estimated when using a more complex equivalent circuit (Figure A.4). The resulting fitting seems to be quite good and a very good curve agreement has been obtained. The analysis using the above-mentioned method, indicates an equivalent circuit that can be mathematically represented by a five-poles transfer function (five time constants are identified). Such an equivalent circuit is composed of a series of five RC elements in parallel. A possible design for this equivalent electric circuit is shown in Figure A.4.
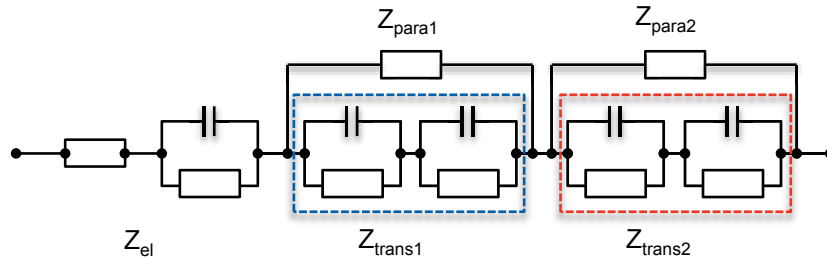
Figure A.4: A proposed equivalent circuit of a mesentery and respectively the measuring electrode.

In this electric model, the transcellular impedance (sum of the apical and basolateral cell membrane impedance) of both cell layers (Z_{trans1} and Z_{trans2}) is represented by two parallel RC elements in series. Parallel to the resistances and capacities of the cell membranes, the paracellular resistance of the tissue (Z_{para1} and Z_{para2}) is connected. The impedance of the electrode-electrolyte system (Z_{el}) is also considered. Moreover, from the obtained poles, the RC values could be calculated using the relation $RC = 1/|a_m|$.
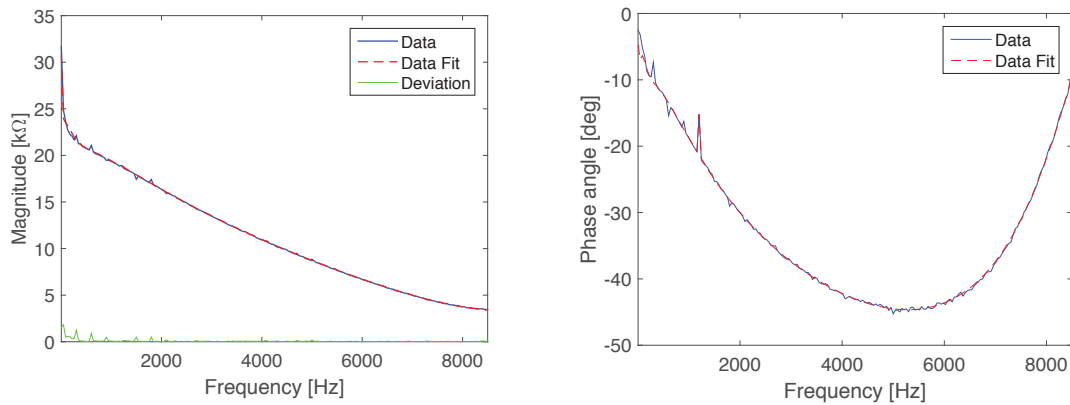
Figure A.5: Plot of measured and fitted impedance data (membrane holder opening with 1cm diameter is used): magnitude of a transfer function as a function of frequency (left); phase of a transfer function as a function of frequency (right).

In a case, as above-presented, a presence of multiple time constants (relaxation processes) is apparent. The single-time relaxations overlap and appear as one dispersion. Hence, another complex model can be considered. When an appearance of spectrum of relaxation processes is identified, then a good agreement with biological systems has been often obtained by incorporation of non-ideal elements that are frequency-dependent. Therefore, instead of using a number of RC circuits in series, it is more commonly to use the Cole impedance model ([38], [39]) by introducing a "Constant Phase Element" (CPE) (section 2.4.2.1).

The Cole-Cole model presented in Figure 2.17 was fitted to the measured data. The impedance of this circuit is given by equation (2.3). The equation contains four parameters that have to be identified: α, R_∞, R_0 and τ, where R_0 is the resistance at very low frequencies, R_∞ is the high frequency resistance and τ is the time constant of the system. The electrical parameters were estimated by implementing the Nelder - Mead (simplex) method for finding the minimum of a scalar function of several variables (the same method was implemented in this doctoral thesis).

The measured and identified values of an equivalent circuit of the entire measurement system including the electrodes, electrolyte and biological sample are shown in Figure A.6. As it can be seen, the form of the identified curve fits the measured curve very good, but unfortunately the obtained frequencies do not match. To better show this effect, the data of four frequencies is chosen and additionally plotted using filled-in circles. This implies that the chosen model is not sufficient to identify the entire measurement system all at once.
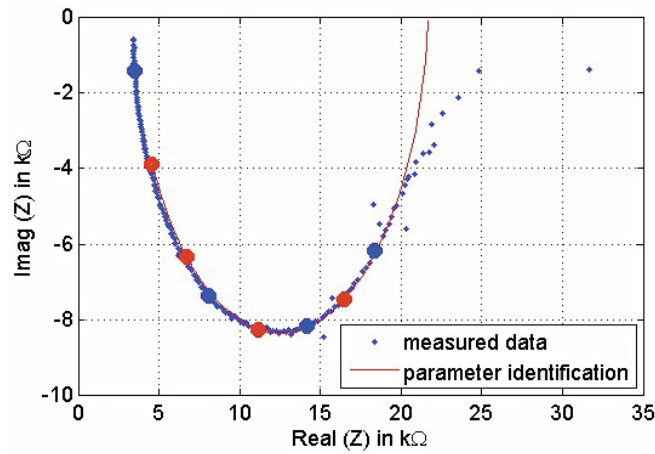
Figure A.6: Plot of the equivalent resistance against equivalent reactance: data obtained from the measurements (blue) and from the identification in MATLAB®/Simulink® (red). The filled-in circles present measured and identified values at the following frequencies: 2, 4, 6 and 8 kHz.

Overall, the presented models (designs) of the above-proposed equivalent circuits serve as an outlook for further analysis of the measured data. For better approximation of the electrical properties of the biosample and its distinguishing from the electrode-electrolyte system properties (polarization impedance), it is highly advisable to do two measurements (just as proposed in the simulations, section 5.1.3): one only with the measuring electrode configuration immersed into the bathing solution whereas in the second measurement the biosample should be additionally included. The difference between the two measurements should yield the approximate impedance spectra of only the biological sample under study.

References

[1]   Loizou, P. (1998). Introduction to cochlear implants. *Tutorial article on cochlear implants in IEEE Signal Processing Magazine* , 101-130.

[2]   Pau, H. W., Just, T., Dommerich, S., Lehnhardt, E., & Behrend, D. (2005). Konzept eines „endostealen" Cochlear Implant-Elektrodenträgers für Patienten mit Restgehör und Machbarkeitsstudie aus anatomischer Sicht. *Laryngo-Rhino-Otol*. Vol. 84, 402-407.

[3]   Lehnhardt, E., Hessel, H., Gibson, P., Parker, J. & von Wallenberg, E. (2006). Cochlea Endosteal Electrode Carrier Member. *Patent Application Publication*.

[4]   Rubinstein, J. (1987). Quasi-static analytical models for electrical stimulation of the auditory nervous system. *PhD. dissertation*. University of Washington.

[5]   Suesserman, M. F., & Spelman, F. A. (1993). Lumped-Parameter Model for In Vivo Cochlear Simulation. *IEEE Transactions on Biomedical Engineering*. Vol. 40. No. 3.

[6]   Tognola, G., Pesaroti, A., Norgia, M., Parazzini, M., Di Renzo, L., Ravazzani, P., et al. (2007). Numerical Modeling and Experimental Measurements of the Electric potential Generated by the Cochlear Implants in Physiological Tissues. *IEEE Transactions on Instrumentation and Measurement*, Vol. 56, No. 1, 187-193.

[7]   Briaire, J., & Frijns, J. (2000). Field patterns in a 3D tapered spiral model of the electrically stimulated cochlea. *Hearing Research,* Vol. 148 , 18-30.

[8]   Gruenbaum, A. (2014). Entwicklung eines detaillierten Modells der humanen Cochlea für numerische Studien von implantierten Elektroden. *Dissertation, Universität Rostock*.

[9]   Sriperumbudur, K., Pau, H. W., & van Rienen, U. (2015). Electrical Stimulation of Spiral Ganglion Cells in the Human Cochlea: A 3D Model. *International Conference on the Computation of Electromagnetic Fields (COMPUMAG 2015)*, Montreal, CA, paper number: PC1-11.

[10]   Foley, H. J., & Matlin, M. W.. Sensation & perception, The Auditory System. URL *http://www.skidmore.edu/~hfoley/Perc9.htm*. Last checked on 9 May 2017.

[11]   URL   *http://jacusers.johnabbott.qc.ca/~paul.anderson/806LAB   ANSWERS/ EYELAB/17-26ab_1.JPG* . Last checked on 9 May 2017.

[12]   Lang, F., & Lang, P. (2007). *Basiswissen Physiologie, 2 Auflage*. Springer Medizin Verlag.

[13]   *https://previews.123rf.com/images/alila/alila1203/alila120300014/12772769-Anatomie-der-Cochlea-des-menschlichen-Ohres-Lizenzfreie-Bilder.jpg*.   Last checked on 9 May 2017.

[14]   Purves, D., Augustine, G., Fitzpatrick, D., Hall, W., LaMantia, A.-S., McNamara, J., et al. (2004). Chapter 12 : The Auditory System. In *Neuroscience:Third edition*. Sinauer Associates, Inc.

[15]   Cochlear fluids composition. URL *http://oto2.wustl.edu/cochlea/intro3.htm*. Last checked on 30 Nov. 2013.

[16]   Clopton, B., & Spelman, F. (2006). Chapter 5: Auditory System. In B. Palsson, J. Hubbel, R. Plonsey, & J. Bronzino, *Tissue Engineering*. Taylor & Francis e-Library.

[17]   URL *http://www.lfu.bayern.de/laerm/so_hoeren_wir/index.htm*. Last checked on 8 May 2017.

[18]   Braun, K. A. M. (2014). Dreidimensionale Rekonstruktion humaner Cochleae mit implantierten Cochlea Implantat-Elektroden. *Dissertation*, Universität München.

[19]   Spelman, F. A (2006). Cochlear Electrode Arrays: Past, Present and Future. *Audiology & Neurotology*, Vol. 11, 77-85.

[20]   Rask-Andersen H., Liu, W., Erixon, E., Kinnefors, A., Pfaller, K., Schrott-Fischer, A., & Glueckert, R. (2012). Human Cochlea: Anatomical Characteristics and Their Relevance for Cochlear Implantation. *The Anatomical Record,* Vol. 295, 1791-1811.

[21]   The structure and function of the inner ear - LabSpace-The open university. URL *http://labspace.open.ac.uk/mod/resource/view.php?id=415641*. Last checked on 8 May 2017.

[22]   Advanced Bionics: The cochlear implant technology innovation. URL *http://www.advancedbionics.com.* Last checked on 8 May 2017.

[23]   URL *https://commons.wikimedia.org/wiki/File:Cochlear_Implant.png*. Last checked on 17 May 2017.

[24]   Briare, J. J. (2008). Cohlear Implants – From Model to Patients. *Dissertation,* University of Leiden.

[25]   Gstoettner, W. K., Adunka, O., Franz, P., Hamzavi, J., Plenk JR., H., Susani, M., Baumgartner, W., & Kiefer, J. (2001). Perimodiolar Electrodes in Cochlear Implant Surgery. *Acta Otolaryngologica,* Vol. 121, 216-219.

[26]   AOS_brochure: New Clinical Evidence Confirms the importance of Perimodiolar Electrodes. URL *http://www.cochlear.com*. Last checked on 19 May 2017.

[27]   Pau, H. W., Just, T., Dommerich, S., & Behrend, D. (2007). Temporal bone investigations on landmarks for conventional and endosteal insertion of cochlear electrodes. *Acta Otolaryngologica,* Vol. 127, 920-926.

[28]   van Rienen, U., Pau, H. W., Sun, C., Veerathu, S., Schulze, S., & Schreiber, U. (2006). Electro-quasistatic Field Simulation of an Endosteal Cochlea Implant. *European Conference on Computational Fluid Dynamics*.

[29] Grimnes, S., & Martinsen, Ø.G. (2006). Bioimpedance. In *Wiley Encyclopedia of Biomedical Engineering.*

[30] Grimnes, S., & Martinsen, Ø.G. (2008). *Bioimpedance and bioelectricity basics: Second edition.* Elsevier Ltd.

[31] Min, M., Pliquette, U., Nacke, T., Barthel, A., Annus, P., & Land, R. (2008). Broadband excitation for short-time impedance spectroscopy. *Physiological Measurements*, Vol. 29, 185-192.

[32] Paavle, T., Min, M., & Parve, T. (2008). Using of Chirp Excitation for Bioimpedance Estimation: Theoretical Aspects and Modelling. *International Biennial Baltic Conference (BEC2008)*, Tallinn, Estonia.

[33] Yang, Y., Kang, M., Lu, Y., Wang, J., Yue, J., & Gao, Z. (2011). Design of a wideband excitation source for fast bioimpedance spectroscopy. *Measurement Science and Technology*, Vol. 22.

[34] Martinsen, Ø.G., Grimnes, S., & Schwan H.P. (2002). Interface phenomena and dielectric properties of biological tissue. Encyclopedia of Surface and Colloid Science, Marcel Dekker Inc., 2643-2652.

[35] Barsoukov, E., & Macdonald, J. (2005). *Impedance Spectroscopy: Theory, Experiment and Aplications Second Edition*. John Wiley & Sons Inc.

[36] Macdonald, J. R. (1992). Impedance spectroscopy. *Annals of Biomedical Engineering*, Vol. 20, 289-305.

[37] Miklavcic, D., Pavselj, N., & Hart, F. X. (2006). Electrical properties of tissues. In *Wiley Encyclopedia of Biomedical Engineering*. John Wiley & Sons Inc.

[38] Cole, K. S. & Cole, R. H. (1941). Dispersion and absorption in dielectrics I. Alternating current characteristics. *J. Chem. Phys.*, Vol. 9, 341-351.

[39] Grimnes, S., & Martinsen, Ø.G. (2005). Cole Electrical Impedance Model-A Critique and a Alternative. *IEEE Transactions on Biomedical Engineering*, Vol. 52, No. 1, 132-135.

[40] Kuang, W., & Nelson, S. O. (1998). Low-frequency dielectric properties of biological tissues: A review with some new insights. *Transactions of the ASAE*, Vol. 41, No. 1, 173-184.

[41] Davarcioglu, B. (2011). The dielectric properties of human body tissues at electromagnetic wave frequencies. *International Journal of Science and Advanced Technology*, Vol. 1, No. 5, 12-18.

[42] Coster, H. G. L., Chilcott, T. C., & Coster, A. C. F. (1996). Review: Impedance spectroscopy of interfaces, membranes and ultrastructures. *Bioelectrochemistry and Bioenergetics,* Elsevier Science S. A, 79-98.

[43] Filho, P. B. (2002). Tissue characterisation using an impedance spectroscopy probe. *Doctor thesis*, Department of Medical Physics and Clinical Engineering, University of Sheffield.

[44] Rigaud, B., Hamzaoui, L., Frikha, M. R., Chauveau, N., Granié, M., Scotto Di Rinaldi, J.-P., & Morucci, J.-P. (1994). Tissue characterization by impedance: a multifrequency approach. *Physiol. Meas.*, Vol. 5, 13-20.

[45] Rigaud, B., Hamzaoui, L., Frikha, M. R., Chauveau, N. & Morucci, J.-P. (1995). *In vitro* tissue characterization and modelling using electrical impedance measurements in the 100Hz-10MHz frequency range. *Physiol. Meas.*, Vol. 16, 15-28.

[46] Gabriel, C., Gabriel, S. & Corthout, E. (1996). The dielectric properties of biological tissues: I. Literature survey. *Phys. Med. Biol.* Vol. 41, 2231-2249.

[47] Gabriel, S., Lau, R. W. & Gabriel, C. (1996). The dielectric properties of biological tissues: II. Measurements in the frequency range 10 Hz to 20 GHz. *Phys. Med. Biol.*, Vol. 41, 2251-2269.

[48] Gabriel, S., Lau, R. W. & Gabriel, C. (1996). The dielectric properties of biological tissues: III. Parametric models for the dielectric spectrum of tissues. *Phys. Med. Biol.*, Vol. 41, 2271-2293.

[49] Dean, D. A., Ramanathan, T., Machado, D. & Sundararajan, R. (2008). Electrical impedance spectroscopy study of biological tissues. *J. Electrostat.*, Vol. 66, 165-177.

[50] Gabriel, C., Peyman, A. & Grant, E. H. (2009). Electrical conductivity of tissue at frequencies below 1 MHz. *Phys. Med. Biol.,* Vol. 54, 4863-4878.

[51] Neuman, M. R. (2000). Chapter 48: Biopotential electrodes. The Biomedical Engineering Handbook: Second Edition by CRC Press LLC.

[52] Albulbul, A. (2016). Evaluating major electrode types for idle biological signal measurements for modern medical technology. *Bioengineering* 3,20 doi:10.3390/bioengineering3030020.

[53] von Békésy, G. (1952). DC resting potentials inside the cochlear partition. *Journal of the Acoustical Society of America*, Vol. 24, 72-76.

[54] Spelman, F. A., Clopton, B. M., Pfingst, B. E. (1982). Tissue impedance and current flow in the implanted ear. Implications for the cochlear prosthesis. *Ann. Otol. Rhinol. Laryngol* , Vol. 98, 3-8.

[55] Kumar, G., Chokschi, M., & Richter, C.-P. (2010). Electrical impedance measurements of cochlear structures using the four-electrode reflection-coefficient technique. *Hearing Research,* Vol. 259, 86-94.

[56] Gisselsson, L. (1960). Die elektrischen Potentiale des Innenohres. *European Archives of Oto-Rhino-Laryngology*, Vol. 177, 45–56.

[57] Geisler, C. D., Mountain, D. C., Hubbard, A. E., Adrian, H. O., Ravindran, A. (1977) Alternating electrical-resistance changes in guinea-pig cochlea caused by acoustic stimuli. *Journal of the Acoustical Society of America*, Vol. 61, 1557-1566.

[58] Asakuma, S., Snow Jr., J. B., & Murakami, Y. (1978). Electrical Resistance of the Cochlear Partition. *Hearing Research* , 25-30.

[59] Chou, J. T. Y., & Hellenbrecht, D. (1979). Further studies of the membrane potential of the stria cells of the guinea pig in vitro. *Acta Oto-Laryngologica*, Vol. 88, 187–197.

[60] Suesserman, M. F., & Spelman, F. A. (October 1993). Quantitative In Vivo Measurements of Inner Ear Tissue Resistivities: I. In vitro Characterization. *IEEE Transactions on Biomedical Engineering*, Vol. 40, No. 10, 1032-1047.

[61] von Békésy, G. (1960). Experiments in hearing. New York: McGraw-Hill.

[62] Ulfendahl, M., & Flock, A. (1998). In vitro studies of cochlear excitation. *Current Opinion in Neurobiology*, Vol. 8, 475-479.

[63] Johnstone, B., Johnstone, J., & Pugsley, I. (1966). Membrane resistance in endolymphatic walls of the first turn of the guinea-pig cochlea. *Journal of the Acoustical Society of America*, Vol. 40, 1398-1404.

[64] Honrubia, V., Strelioff, D., & Sitko, S. (1976). Electroanatomy of the cochlea: Its role in cochlear potential measurements. *Electrocochleography*, 23-40.

[65] Strelioff, D. (1973). A computer simulation of the generation and distribution of cochlear potentials. *Journal of the Acoustical Society of America*, Vol. 54, 620-629.

[66] Spelman, F. A, Pfingst B. E, Miller, J. M, Hassul, M, Powers, W. E, Clopton, B. M (1980). biophysical measurements in the implanted cochlea. *Otolaryngol Head Neck Surg,* Vol. 88, 183-187.

[67] Ulfendahl, M., Flock, Å., & Khanna, S. M. (1989). A temporal bone preparation for the study of cochlear micromechanics at the cellular level. *Hearing research*, Vol. 40, 55–64.

[68] Gummer, A., Hemmert , W., Morioka, I., Reis, P., Reuter, G., & Zenner, H. (1996). Cellular motility measured in the guinea pig cochlea. *Biophysics of Hair Cell Sensory Systems*, Vol. 93, 229-239.

[69] Lemmer, C. (2010). Aufbau eines Messplatzes zur Ermittlung der elektrischen Impedanz an biologischen Gewebsstrukturen. *Bachelorarbeit*. University of Rostock.

[70] Hamilton, KL (2011). Ussing's "little chamber": 60 years+ old and counting. *Front. Physio*. 2:6. doi: 10.3389/ fphys.2011.00006.

[71] npi electronic GmbH: Operating instructions and system description of the SEC-10LX single electrode systems. (*http://www.npielectronic.com*).

[72] npi electronic GmbH: Operating instructions and system description for the passive cell model for single electrode switched amplifiers. (*http://www.npielectronic.com*).

[73] npi electronic GmbH: Operating instructions and system description of the SEC-03M single electrode clamp amplifier module for epms systems. (*http://www.npielectronic.com*).

[74] Huang, H., Wylie, J. J., Miura, R. M., & Howell, P. D. On the Formation of glass microelectrodes.

96

[75] *https://radiologykey.com/imaging-of-the-peritoneum-mesentery-and-omentum/.* Last checked on 25 Oktober 2017.

[76] *http://www.dummies.com/education/science/anatomy/what-is-the-peritoneum/.* Last checked on 25 Oktober 2017.

[77] Kosub, R. (2016). Elektrische Charakterisierung von biologischen Membranen zur Modellbildung der menschlichen Cochlea. *Bachelorarbeit.* University of Rostock.

[78] Stanford Research Systems: Modell SR830 DSP Lock-In Amplifier (1993).

[79] Haus, H. A., & Melcher, J. R. (1989). Electromagnetic Fields and Energy. Prentice-Hall. Inc. (*http://web.mit.edu/6.013 book/www/*).

[80] van Rienen, U. (2001). Numerical methods in computational electrodynamics - linear systems in practical applications. *Springer, Lecture Notes in Computational Science and Engineering,* Vol.12.

[81] van Rienen, U., Flehr, J., Schreiber, U., & Motrescu, V. (2003): Chapter: Modeling and Simulation of Electro-Quasistatic Fields. In Simulation and Optimization of Integrated Circuits: International Series of Numerical Mathematics, Birkhäuser Verlag, Basel/Switzerland, Vol. 146, 17-31.

[82] van Rienen, U., Flehr, J., Schreiber, U., Schulze, S., Gimsa, U., Baumann, W., Weiss, D.G, Gimsa, J., Benecke, R., & Pau, H.-W. (2005) Electro-Quasistatic Simulations in Bio-Systems Engineering and Medical Engineering, *Advances in Radio Science* Vol. 3, 39-49.

[83] Bondeson, A., Rylander, T., & Ingeström, P. (2005). Computational electromagnetics. *Springer.*

[84] Lanthier, R., & Schanne, O. (1966). Change of microelectrode resistance in solutions of different resistivities. Naturwissensh. Affen., Vol. 53, 430-431.

[85] Schanne, O., Lavallée, M., Laprade, R., & Gagné, S. (June 1968). Electrical Properies of Glass Microelectrodes. *Proceedings of the IEEE ,* Vol. 56, No. 6.

[86] Plamondon, R., & Gagné, S. (1980). On the influence of Diffusion, Double Layer, and Glass Conduction on the Electrical Resistance of Open Tip Glass Microelectrodes. *IEEE Transactions on biomedical engineering.* Vol. 27, No. 5.

[87] Cornwall, M., & Thomas, M. (1981). Glass microelectrode tip capacitance:its measurements and a method for its reduction. *Journal of Neuroscience Methods ,* 225-232.

[88] Gagne, S., & Plamondon, R. (1987). Open Tip Glass Microelectrode Conduction Through the Wall. *IEEE Transactions on biomedical engineering.* Vol. 34, No. 1.

[89] Holst, M., Pau, H.-W., & van Rienen, U. (2013). Modelling and simulation of an in-vitro experimental set-up to determine membrane electric properties. *Biomedical Engineering / Biomedizinische Technik*, Vol. 58, 747-748, DOI 10.1515/bmt-2013-4359.

[90] Fromm, M., & Schultz, S. (1981). Some properties of KCl-filled microelectrodes: Correlation of potassium "leakage" with tip resistance. *J. Membrane Biol.*, Vol. 62, 239-244.

[91] Amatniek, E. (1958). Measurement of bioelectric potentials with microelectrodes and neutralized input capacity amplifiers. *IRE Transactions on medical electronics*, 3-14.

[92] Rustgi, A. (1994). Modelling of the glass microelectrode tip. *IEE Pro.-Sci. Meas. Technol.*, Vol. 141, No. 5, 391-394.

[93] Nastuk, W. L., & Hodgkin, A. L. (1950). The electrical activity of single muscle fibers. *J. Cell. Comp. Physiol.*, Vol. 35, 39-73.

[94] Bretschneider, F., & Weille, J. (2006). *Introduction to electrophysiological methods and instrumentation.* Academic Press.

[95] Frijns, J. H. M., de Snoo, S. L. & Schoonhoven, R. (1995). Potential distributions and neural excitation pattervs in a rotationally symmetric model of the electrically stimulated cochlea. *Hearing Research,* Vol. 87, 170-186.

[96] Herrmann, A., Köhling, R., & Warkentin, M. (2010). Impedanzmessungen an cochleären Strukturen zur Entwicklung einer endostealen Elektrode. *Projektförderung.*

[97] Brette, R. & Destexhe, A. (2012). Chapter 3 : Intracellular recording. In *Handbook of Neural Activity Measurement.* Cambridge University Press.

[98] MDS Analytical Technologies (2008). The Axon Guide: A Guide to Electrophysiology and Biophysics Laboratory Techniques: *Third edition.*

[99] Puil, E., Gimbarzevsky, B. & Miura, R.M. (1986). Quantification of membrane properties of trigeminal root ganglion neurons in guinea-pig. *Journal of Neurophysiology*, Vol. 55, 995-1016.

[100] Gutfreund, Y., Yarom, Y., & Segev, I. (1995). Subtreshold oscillations and resonant frequency in guinea-pig cortical neurons: physiology and modelling. *Journal of Physiology* , Vol. 483.3, 621-640.

[101] Pike, F., Goddard, R., Suckling, J., Ganter, P., Kasthuri, N., & Paulsen, O. (2000). Distonct frequency preferences of different types of rat hippocampal neurones in response to oscillatory input currents. *Journal of Physiology* , Vol. 529.1, 205-213.

[102] Hutcheon, B. & Yarom, Y. (2000). Resonance, oscillation and the intrinsic frequency preferences of neurons. *Trends in Neurosciences*, Vol. 23, No. 5, 216–222.

[103] Hu, H., Vervaeke, K., & Storm, J. F. (2002). Two forms of electrical resonance at theta frequencies, generated by M-current, h-current and persistent Na+ current in rat hippocampal pyramidal cells. *Journal of Physiology,* Vol. 545.3, 783-805

[104] Yang, Y., Kang, M., Lu, Y., Wang, J., Yue, J., & Gao, Z. (2011). Design of a wideband excitation source for fast bioimpedance spectroscopy. *Meas.Sci.Technol.,* Vol. 22.

[105] *https://sciencing.com/conductivity-vs-concentration-6603418.html.* Last chacked on 6 March 2018.

[106] Rosemount (2010). Conductance data for commonly used chemicals. (*http://instrumentationandcontrol.net/instrumentation-technician-rosemount-2010-conductance-data-commonly-used-chemicals/*).

[107] Gitter, A. H. (2001). Elektrodynamische Modellierung epithelialer Gewebe (Skripte).(*https://klinphys.charite.de/bioinfo/4_k-schluesstech-guenzel/skripte_epithelmodell.pdf*). Last checked on 14 May 2018.

[108] Awayda, M. S., Van Driessche, W., & Helman, S. I. (1999). Frequency-Dependent Capacitance of the Apical Membrane of Frog Skin: Dielectric Relaxation Processes. *Biophysical Journal*, Vol. 76, 219-232.

[109] Kreindler, J. L., Jackson, A. D., Kemp, P. A., Bridges, R. J., & Danahay, H. (2005). Inhibition of chloride secretion in human bronchial epithelial cells by cigarette smoke extract. *Am J Physiol Lung Cell Mol Physiol*, Vol. 288, 894-902.

[110] URL *https://www.sintef.no/en/software/vector-fitting/.* Last checked on 1 June 2018.

[111] URL *https://www.sintef.no/projectweb/vectfit/.* Last checked on 1 June 2018.

[112] Gustavsen, B., & Semlyen, A. (1999). Rational approximation of frequency domain responses by vector fitting. *IEEE Trans. Power Del.*, Vol. 14, No. 3, 1052-1061.

[113] Gustavsen, B. (2006). Improving the pole relocating properties of vector fitting. *IEEE Trans. Power Del.*, Vol. 21, No. 3, 1587-1592.

[114] Gustavsen, B., & De Silva, H. M. Jeewantha (2013). Inclusion of rational models in an electromagnetic transients program: Y-Parameters, Z-Parameters, S-Parameters, Transfer Functions. *IEEE Trans. Power Del.*, Vol. 28, No. 2, 1164-1174.